Modelling radiation fields of ion beams in tissue-like materials

Dissertation
for attaining the PhD degree
of Natural Sciences

submitted to the Faculty of Physics
of the Johann Wolfgang Goethe University
in Frankfurt am Main

by
Lucas Norberto Burigo
from Criciuma, Brazil

Frankfurt 2014
(D 30)

accepted by the Faculty of Physics of the
Johann Wolfgang Goethe University as a dissertation.

Dean:	Prof. Dr. Joachim Stroth
Expert assessor:	Prof. Dr. Marcus Bleicher
	Prof. Dr. Igor Mishustin

Date of the disputation: 16 July 2014

To my family

Acknowledgements

I would like to express my sincere gratitude to my collaborators Dr. habil. Igor Pshenichnov, Prof. Dr. Igor Mishustin and Prof. Dr. Marcus Bleicher for their direct contribution to the development of my Ph.D. studies and my scientific career. They were always available and ready to help me whenever I needed. I would also like to acknowledge the careful review of this dissertation by Igor Pshenichnov. I am also grateful to Igor Mishustin for the invitation to carry out my Ph.D. studies at FIAS.

I am also grateful to Beilstein-Institut, HIC for FAIR, and HGS-HIRe for their generous financial support, to members of the HGS-HIRe management board, in particular, Dr. Gerhard Burau, Dr. Sascha Vogel and Johanna Dilley, to the secretaries at FIAS, Walburga Bergmann and Eike Schädel, and to IT services members at CSC and FIAS, in particular Alexander Achenbach and Michael Lehmann, who assisted in many bureaucratic and technical issues.

The time I've spent in Frankfurt have been marvellous, especially thanks to my wife, Bruna, and my daughter, Elisa. Their love, unconditional support and understanding were of utmost importance. I cannot imagine how I could have succeeded without them.

I also want thank my parents, Valquiria and Norberto, my sister, Michele, my grandparents, Gracina and Olírio (*in memoriam*), Cecília (*in memoriam*) and Waldemar (*in memoriam*), Nair (*in memoriam*) and Virgínio (*in memoriam*), and my parents-in-law, Isabel and Renato, who directly contributed to my personal development and achievements.

Many thanks to colleagues I met at FIAS and HGS-HIRe events, Alessandro Brillante, Antonia Frassino, Daniel Yueker, Maximilian Attems, Rodrigo Negreiros, Vladimir Lavrik and Yuri Malyshkin, for making the working hours even more pleasant. In particular, I thank Daniel also for helping me translate the abstract into German.

Last but not least, I would like to thank my friends in Brazil, Diogo, Elízio, Felipe and Pablo, who were constantly writing me and waiting patiently for my answers, and the new friends I met in Frankfurt, Beti and Wilton, for their support and motivation at difficult times.

Preface

This dissertation is submitted to the Faculty of Physics of the Johann Wolfgang Goethe University for attaining the PhD degree of Natural Sciences. The research described herein was conducted under the supervision of Prof. Dr. Igor Mishustin and Prof. Dr. Marcus Bleicher at the Frankfurt Institute for Advanced Studies, between May 2011 and April 2014.

The results of this work have been presented in the following publications:

- Burigo L, Pshenichnov I, Mishustin I, Bleicher M. 'Microdosimetry of radiation field from a therapeutic ^{12}C beam in water: A study with Geant4 toolkit.' *Nucl. Instrum. Meth. B* (2013) **310**: 37–53. doi:10.1016/j.nimb.2013.05.021.

- Burigo L, Pshenichnov I, Mishustin I, Bleicher M. 'Microdosimetry spectra and RBE of ^{1}H, ^{4}He, ^{7}Li and ^{12}C nuclei in water studied with Geant4.' *Nucl. Instrum. Meth. B* (2014) **320**: 89–99. doi:10.1016/j.nimb.2013.10.018.

- Burigo L, Pshenichnov I, Mishustin I, Bleicher M. 'Comparative study of RBE and cell survival fractions for ^{1}H, ^{4}He, ^{12}C and ^{16}O beams using Geant4 and Microdosimetric Kinetic model.' (2014). arXiv:1403.7929 [physics.med-ph].

- Burigo L, Pshenichnov I, Mishustin I, Bleicher M. 'Monte Carlo simulations of Microdosimetry for Space Research at FAIR.' *J. Phys. Conf. Ser.* (2013) **426**(1): 012006. doi:10.1088/1742-6596/426/1/012006.

- Burigo LN, Pshenichnov IA, Mishustin IN, Bleicher M. 'Radiation quality of cosmic ray nuclei studied with Geant4-based simulations.' *J. Phys. Conf. Ser.* (2014) **503**(1): 012021. doi:10.1088/1742-6596/503/1/012021.

- Bleicher M, Burigo L, Durante M, Herrlitz M, Krämer M, *et al.* 'Nanolesions induced by heavy ions in human tissues: Experimental and theoretical studies.' *Beilstein J. Nanotechnol.* (2012) **3**: 556–563. doi:10.3762/bjnano.3.64.

Lucas Norberto Burigo

April 2014

Abstract

Fast nuclei are ionizing radiation which can cause deleterious effects to irradiated cells. The modelling of the interactions of such ions with matter and the related effects are very important to physics, radiobiology, medicine and space science and technology. A powerful method to study the interactions of ionizing radiation with biological systems was developed in the field of microdosimetry. Microdosimetry spectra characterize the energy deposition to objects of cellular size, *i.e.*, a few micrometers.

In the present thesis the interaction of ions with tissue-like media was investigated using the Monte Carlo model for Heavy-Ion Therapy (MCHIT) developed at the Frankfurt Institute for Advanced Studies. MCHIT is a GEANT4-based application intended to benchmark the physical models of GEANT4 and investigate the physical properties of therapeutic ion beams. We have implemented new features in MCHIT in order to calculate microdosimetric quantities characterizing the radiation fields of accelerated nucleons and nuclei. The results of our Monte Carlo simulations were compared with recent experimental microdosimetry data.

In addition to microdosimetry calculations with MCHIT, we also investigated the biological properties of ion beams, *e.g.* their relative biological effectiveness (RBE), by means of the modified Microdosimetric-Kinetic model (MKM). The MKM uses microdosimetry spectra in describing cell response to radiation.

MCHIT+MKM allowed us to study the physical and biological properties of ion beams. The main results of the thesis are as follows:

- MCHIT is able to describe the spatial distribution of the physical dose in tissue-like media and microdosimetry spectra for ions with energies relevant to space research and ion-beam cancer therapy.
- MCHIT+MKM predicts a reduction of the biological effectiveness of ions propagating in extended medium due to nuclear fragmentation reactions.
- We predicted favourable biological dose-depth profiles for monoenergetic helium and lithium beams similar to the one for carbon beam. Well-adjusted biological dose distributions for ^{1}H, ^{4}He, ^{12}C and ^{16}O with a very flat spread-out Bragg peak (SOBP) plateau were calculated with MCHIT+MKM.
- MCHIT+MKM predicts less damage to healthy tissues in the entrance channel for SOBP ^{4}He and ^{12}C beams compared to ^{1}H and ^{16}O ones. No definitive advantages for oxygen ions with respect to carbon were found.

Zusammenfassung

Hochenergetische Ionen findet man in kosmischer Strahlung. Außerdem werden schnelle Kerne durch Teilchenbeschleuniger bereitgestellt, die heutzutage nicht nur in Kern- und Teilchenphysiklaboren gegenwärtig sind, sondern auch in Krankenhäusern. Die Wechselwirkung solcher Ionen mit Materie und die damit verwandten Effekte sind sehr wichtig für Physik, Radiobiologie, Medizin, sowie Raumfahrtwissenschaft und -technik.

Wenn schnelle Ionen ein Medium durchdringen, schlagen sie Elektronen aus Atomen und Molekülen, wobei sie freie Radikale produzieren vergleichbar mit jeder anderen Art ionisierender Strahlung. Als Folge können Ionen schädliche Wirkungen an bestrahlten Zellen durch die Beschädigung ihrer Makromoleküle und Zellstruktur verursachen. Mehrere wichtige Effekte werden beobachtet, einschließlich Mutation und Zelltod. Die enorme Komplexität der Zellansprechbarkeit auf die Strahlung, erlaubt keine vollständige und fehlerfreie Beschreibung der biologischen Effekte, nachdem die Zellen der Strahlung ausgesetzt wurden. Das Untersuchen physikalischer, chemischer und biologischer Reaktionen initiiert durch das Passieren schneller Ionen durch ein Medium hilft die Auswirkungen solcher ionizierender Strahlung zu verstehen.

Verschiedene Strategien werden angewendet, um die Auswirkungen der Strahlungsfelder von Ionenstrahlen zu untersuchen. Während frühe Studien mit Teilchen ausgeführt wurden, die durch radioaktive Kerne emittiert wurden, beobachtete man in den letzten Jahrzehnten die zunehmende Rolle der Teilchenbeschleuniger in radiobiologischen Experimenten und der Patientenbehandlung. Untersuchungen der Bestrahlung von Zellen und präklinische Verfahren mit Ionenstrahlen, sowie der Fortschritt in der Beschleunigertechnik, führten zur Entwicklung der modernen Radiotherapie, heute bekannt als Ionenstrahl-Krebstherapie. Sie wendet Protonenstrahlen oder Kohlenstoffionen an, um Patienten mit lokalisierten Tumoren zu behandeln, die nicht operativ entfernt werden können. Es gibt mehrere theoretische Modelle, die in der Lage sind die Zellansprechbarkeit auf Strahlung zu beschreiben. In diesen Modellen hängt die relative biologische Effektivität (RBE) beschleunigter Kerne von der Ionenmasse, der Ladung, der kinetischen Energie und dem Zelltyp ab.

Eine wirkungsvolle Methode um die Wechselwirkung ionisierender Strahlung mit biologischen Systemen zu charakterisieren ist die Mikrodosimetrie. Die Mikrodosimetrietechnik wird benutzt um die Fluktuationen der Energiefreisetzung und damit verbundener Größen in Einzelereignissen zu messen, wenn ionisierende Teilchen ein mikroskopisches Objekt durchkreuzen. Die Energie, die Objekten von einigen Mikrometern Größe, welches die typische Dimension des Kerns von Säugetierzellen ist, übermittelt wird, ist die entscheidende in der Mikrodosimetrie gemessene Größe. Das

geschied durch Benutzung eines speziellen Detektors, genannt gewebe-äquivalenter proportionaler Zähler (TEPC) befüllt mit einem verdünnten Gas um ein gewebeartiges Volumen in der Dimension von Mikrometern zu emulieren und die stochastischen Energiefreisetzungsereignisse zu quantifizieren. Die Ansprechfunktion eines TEPC definiert die Variation der Dosis, welche durch Strahlung an einen Zellkern oder andere Sub-Zellkernstrukturen abgegeben wird. Aus diesem Grund ist das mikrodosimetrische Spektrum eine relevante Informationsquelle um radiobiologische Effekte zu modellieren. Mikrodosimetrische Messungen in bodenbasierten Anlagen und in Raumflügen wurden angewendet um galaktische kosmische Strahlung zu untersuchen. Messungen für therapeutische Ionenstrahlung zur Anwendung in der Strahlentherapie wurden auch durchgeführt. Im Besonderen, erlauben TEPC-Detektoren kleiner Größe eingetaucht in realistische Phantome eine räumliche Charakterisierung des Strahlungsfeldes innerhalb eines Patienten.

Theoretische Studien physikalischer Prozesse induziert durch ionisierende Strahlung in gewebeartigen Medien haben zum gegenwärtigen Wissen über Zellansprechbarkeit beigetragen. Theoretische Modellierung und experimentelle Messungen sind komplementäre Ansätze um Strahlungseffekte auf mikroskopischer Skala zu verstehen. Ein rechnerisches Modell, welches in der Lage ist die Ausbreitung energetischer Kerne in erweiterten Medien zu simulieren, dient als ein Werkzeug um diese Effekte zu untersuchen. Berechnungen räumlicher Verteilungen der Energiefreisetzung auf makroskopischer und mikroskopischer Skala durch analytische und Monte-Carlo-Methoden spielen eine wichtige Rolle in solchen Studien. Im Besonderen können Muster der Energiefreisetzung um den Ionenstrahl herum und die Ansprechbarkeitsfunktion eines TEPC durch die Monte-Carlo-Methode simuliert werden.

In der vorliegenden Arbeit wurde die Wechselwirkung von Ionen mit gewebeartigen Medien unter Benutzung des Monte-Carlo-Modells für Schwerionentherapie (MCHIT) untersucht. Entwickelt wurde MCHIT am Frankfurt Institute for Advanced Studies (FIAS). MCHIT ist eine Geant4-basierte Anwendung mit der Absicht die physikalischen Modelle von Geant4 zu benchmarken und die physikalischen Eigenschaften therapeutischer Ionenstrahlung zu untersuchen. Es wurde zuvor demonstriert, dass MCHIT das Tiefendosisprofil für leichte Kerne reproduzieren kann, sowie die Erzeugung sekundärer Neutronen und geladener Fragmente in Kernkollisionen zwischen dem Primärion und Kernen des Mediums beschreiben kann. Zudem wurden auch die Verteilungen positronen-emittierender Kerne, relevant für das PET-Monitoring in der Ionenstrahl-Krebstherapie, erfolgreich berechnet. Wir haben gezeigt, dass das MCHIT-Modell in der Lage ist die räumliche Verteilung der Gesamtdosis in gewebeartigen Medien zu beschreiben, welche um viele Größenordnungen mit der radialen Entfernung von der Strahlachse variiert.

Wir haben neue Funktionalitäten in das MCHIT implementiert um das Benchmarking des Geant4-Modells zu erweitern und die Auflösung der Energiefreisetzung von der Millimeter- auf Mikrometerskala zu erhöhen.Das ist ein notwendiger Schritt zu einem umfassenderen Verständnis der Wechselwirkungen des Ionenstrahles mit gewebeartigen Medien und zur Modellierung respektiver biologischer Effekte. Solche Entwicklungen erlauben uns mikrodosimetrische Größen zu berechnen, die die Strahlungsfelder beschleunigter Nukleonen und Kerne charakterisieren. Im Besonderen wurden die TEPC-Geometrien sorgfältig in MCHIT implementiert unter Benutzung der reichhaltigen Möglichkeiten in Geant4. Die Ergebnisse unserer

Monte-Carlo-Simulationen wurden verglichen mit neuesten experimentellen Mikrodosimetriedaten, gemessen mit verschiedenen TEPCs.

Unsere Studien zeigen, dass MCHIT in der Lage ist die TEPC-Ansprechbarkeitsfunktion, sowie die mikrodosimetrischen Parameter einer breiten Auswahl von Ionenstrahlen und Strahlenergien, die relevant für die Weltraumforschung und Ionenstrahl-Krebstherapie sind, gut zu beschreiben. Im Besonderen haben wir gezeigt, dass mikrodosimetrische Spektren für Protonen, die für einen TEPC makroskopischer Größe gefüllt mit verdünntem Gas berechnet wurden, gut übereinstimmen mit dem Mikrodosimetriespektrum, welches für ein äquivalentes mikroskopisches Wasservolumen berechnet wurde. Auf diese Weise wurde die Grundannahme des Mikrodosimetrietechnik durch Monte-Carlo-Simulationen mit MCHIT validiert.

Die Messungen mikrodosimetrischer Spektren hinter einem erweiterten Medium eröffnen andere Möglichkeiten Monte-Carlo Transport-Codes zu validieren. Kernfragmentationsreaktionen, die zum Beispiel im Abschirmungsmaterial eines Raumfahrzeug oder in Elementen angeordnet vor einem Patienten in Strahlrichtung passieren, führen zu einer signifikanten Modifikation der Strahlungsfelder im interessierenden Bereich, d.h. Zellkerne oder im sensitiven Volumen des TEPC. Während ein TEPC auf der Strahlachse durch primäre Ionen und Sekundärteilchen bestrahlt wird, tragen weit weg von der Strahlachse nur Sekundärteilchen zur Energiefreisetzung bei. Deshalb ist eine korrekte Modellierung der Kernfragmentierungsreaktionen entscheidend für die Beschreibung der Mikrodosimetriespektren, sowohl auf der Strahlachse als auch weit weg vom Strahl. Beiträge zum primären Strahlkern und sekundären Fragmenten wurden gründlich mit MCHIT evaluiert und mit existierenden experimentellen Daten verglichen.

Zwei Kernmodelle von GEANT4 für die schnelle Phase der Kernkollisionen, nämlich Light Ion Binary Cascade und Quantum Molecular Dynamics, stellten sich als gleichermaßen passend heraus um die allgemeinen Eigenschaften der mikrodosimetrischen Spektren zu beschreiben. Jedoch unterschätzen beide Modelle die Flüsse von Protonen und Neutronen weit weg vom Strahl und das Erzeugen von Alphateilchen. Das indiziert die Notwendigkeit Kern-Kern-Kollisionsmodelle beim berechnen der Winkel- und Energieverteilung sekundärer Nukleonen und leichter Fragmente zu verbessern. Weitere Verfeinerung der Kernfragmentierungsmodelle könnten die Beschreibung der mikrodosimetrischen Daten verbessern und daher ein besseres Verständnis der Strahlungsauswirkungen therapeutischer Strahlen auf leichte Kerne ermöglichen.

Der Beitrag von δ-Elektronen zur Energie, freigesetzt im TEPC wurde auch untersucht. Offensichtlich variiert sie bei verschiedenen Detektor-Positionen im Strahlungsfeld. Die Ausbreitung energetischer Strahlkerne durch ein TEPC wird begleitet durch die Produktion energetischer δ-Elektronen, welche dem sensitiven Volumen entkommen könnten und somit Energie nach außen transportieren und freisetzen. Dieser Effekt ist weniger wichtig am Bragg-Peak und auch weit weg von der Strahlachse für die Detektoren, welche nur von Sekundärnukleonen betroffen sind, da sie Niederenergie-Elektronen mit kurzen Reichweiten produzieren.

Die Mikrodosimetriespektren innerhalb und außerhalb des Feldes für therapeutische Ionenstrahlen wurden mit MCHIT in einem konsistenten Ansatz berechnet. Unsere rechnerische Methode ist nützlich um die biologischen Auswirkungen komplexer Strahlungsfelder bei therapeutischen Strahlen abzuschätzen, einschließlich der

Effekte von Sekundärneutronen, produziert in Kernreaktionen. Der Beitrag von Sekundärneutronen zur Out-of-field-Dosis wurde mit MCHIT abgeschätzt für bleistiftartige Kohlenstoffstrahlen, welche typisch in der Strahltherapie sind. Es wurde gezeigt, dass der relative Beitrag der Neutronen sich rapide erhöht, wenn der Detektor sich von der Strahlachse weg bewegt, sowie rückwärts zum Strahl. Da experimentelle Identifikation von Neutronen unhandliche Detektoren erfordern würde, die außerhalb des Phantoms platziert würden, stellen solche mikrodosimetrische Messungen die einzige Möglichkeit bereit die Obergrenzen für die Dosis durch Neutronen und ihre Strahlungsqualität in der Nähe des Targetvolumens im Phantom abzuschätzen.

Zusätzlich zu mikrodosimetrischen Berechnungen mit MCHIT durchgeführt zur physikalischen Charakterisierung des Strahlungsfeldes von Ionen haben wir auch die biologischen Eigenschaften des Ionenstrahls, z.B. seinen RBE, mittels eines radiobiologischen Modells, nämlich des modifizierten Microdosimetric-Kinetic Model (MKM) untersucht. Das MKM benutzt die stochastischen Muster der Energiefreisetzung auf Mikrometerskala beim Beschreiben der Zellansprechbarkeit auf Strahlung. MCHIT+MKM erlauben uns RBE und die biologische Dosis therapeutischer Ionenstrahlen an mehreren Orten in einem gewebeartigen Phantom abzuschätzen, was relevant ist für die Ionenstrahl-Krebstherapie.

Wir haben MCHIT+MKM angewendet um die Auswirkungen von Kernfragmentationsreaktionen auf die biologische Effektivität von Ionenstrahlen zu evaluieren. Der Aufbau der Fragmente reduziert den RBE aufgrund des Verlustes von Strahlenteilchen, welche charakterisiert werden durch ein höheres Bremsvermögen als alle Fragmente zusammen. Im Besonderen wird das RBE_{10} (RBE auf einem Niveau von 10 % Anteil überlebender Zellen) für HGS-Zellen in der Nachbarschaft des Bragg-Peak abgeschwächt. Es ist klar, dass die Auswirkungen von Kernreaktionen in Behandlungsplanungs-Systemen für Ionenstrahl-Krebstherapie nicht vernachlässigbar sind. Die Variation der biologischen Effektivität der Ionen hat auch Implikationen für die Wahl der Materialien und der Abschirmungsdicke beim Bau von Raumfahrzeugen.

Physikalische und biologische Dosisverteilungen monoenergetischer Ionenstrahlen in gewebeartigen Medien wurden mit MCHIT+MKM untersucht. Die Modelle sagen sehr gute biologische Dosentiefenprofile für Helium- und Lithiumstrahlen voraus, ähnlich zu dem des Kohlenstoffstrahls. Diese Kerne sollten also zu Recht als Optionen für die Ionenstrahl-Krebstherapie betrachtet werden. Sie haben einen reduzierten Fragmentierungswirkungsquerschnitt im Vergleich zum Kohlenstoffkern, was sie für tiefsitzende Tumore interessant macht. Zudem haben sie auch eine reduzierte laterale Streuung im Vergleich zum Protonenstrahl. Gleichzeitig ist die biologische Effektivität dieser Strahlen nur leicht niedriger als die des Kohlenstoffstrahls. Diese Ergebnisse empfehlen, dass Helium- und Lithiumstrahlen auch erfolgreich für die Strahlentherapie verwendet werden können.

Detaillierte Simulationen wurden auch für sogenannte spread-out Bragg peaks (SOBP) durchgeführt, welche erforderlich sind, um extensive Tumore in der Ionenstrahl-Krebstherapie zu behandeln. Ein Algorithmus, um SOBP für leichte Kerne aus monoenergetischen Strahlen verschiedener Projektile zu simulieren, wurde entwickelt. Wir haben angepasste biologische Dosisverteilungen für $^{1}\mathrm{H}$, $^{4}\mathrm{He}$, $^{12}\mathrm{C}$ und $^{16}\mathrm{O}$ mit einem sehr flachen SOBP plateau mit MCHIT+MKM berechnet. Dies erlaubt uns die RBE und den Überlebensanteil an Zellen unter Bedingungen zu studieren,

welche hochrelevant für die Strahltherapie sind.

Aus SOBP-Simulationen mit MCHIT+MKM haben wir $RBE_{10,mix}$-Profile für Protonen, ^{4}He, ^{12}C und ^{16}O berechnet, wobei $RBE_{10,mix}$ für RBE_{10} eines SOBP-Strahls steht. Wir fanden heraus, dass die Formen der $RBE_{10,mix}$-Profile für ^{4}He, ^{12}C und ^{16}O einander ähnlich sind, während das $RBE_{10,mix}$-Profil für Protonen fast konstant über die gesamte Tiefe in Wasser ist.

Um Nebenwirkungen der Ionentherapie wie Radionekrose zu reduzieren, sollte der Schaden an umliegendem gesundem Gewebe so weit wie möglich reduziert werden. Mit Hilfe unseres MCHIT-Modells, verbunden mit dem modifizierten MKM-Modell wurde die Schwere dieses Schadens evaluiert durch Berechnung des Zellenüberlebensanteils in gesunden Geweben für mehrere therapeutische Strahlen, nämlich ^{1}H, ^{4}He, ^{12}C und ^{16}O. Wir betrachteten die Fälle normaler, hoher und niedriger Radiosensitivität von Geweben im Tumorvolumen und darum herum. Im Falle früh ansprechender Gewebe induzieren alle vier geladenen Teilchenstrahlen ernsten Schaden nicht nur am Targetvolumen, sondern auch darum herum. Da in diesem Fall der Bereich hohen Schadens nicht mit dem Targetvolumen konform geht, verliert die Behandlung mit geladenen Teilchen ihren Vorteil gegenüber der Behandlung mit Protonen. Im Falle normaler Radiosensitivität verschonen ^{4}He- und ^{12}C-Strahlen Gewebe im Eingangskanal eher als die von ^{1}H und ^{16}O. In allen Fällen sind die Zellenüberlebensanteile berechnet für den Eingangskanal und das Targetvolumen ähnlich für ^{4}He und ^{12}C. Jedoch sobald es wichtig wird gesundes Gewebe hinter dem Rand des SOBP-Plateaus zu verschonen, ist ^{4}He aufgrund der reduzierten Kernfragmentation dieser Projektile empfehlenswerter. Was den Sauerstoffstrahl angeht wurden keine definitiven Vorteile gegenüber Kohlenstoff gefunden, mit Ausnahme einer verstärkten Wirkung dieser schwereren Projektile auf radioresistente Tumore.

Das Verfahren, welches in dieser Arbeit entwickelt wurde, wurde angewandt um die Wechselwirkung zwischen Ionen und gewebeähnlicher Materie zu charakterisieren. MCHIT+MKM erlaubten uns die physikalischen und biologischen Eigenschaften von Ionenstrahlen zu untersuchen. Im Besonderen hilft unsere komparative Studie die angemessensten Ionen für spezifische Behandlungsfälle in der Ionenstrahl-Krebstherapie zu evaluieren. Unser Ansatz kann auch dazu benutzt werden, um den RBE und den Zellüberlebensanteil für andere Ionenarten abzuschätzen.

Contents

Introduction

High-energy ions[1] are found in cosmic rays. Besides, fast nuclei are delivered by accelerator machines present nowadays not only in particle and nuclear physics laboratories but also at hospitals. The interaction of such ions with matter and the related effects are very important to physics, radiobiology, medicine and space science and technology. Studying physical, chemical and biological reactions initiated by the passage of fast ions through a medium helps to understand the effects of such ionizing radiation. This knowledge is fundamental to radiobiology, which studies the impact of ionizing radiation on biological systems, and radiation protection, which deals with techniques to protect human beings and environment from the threats imposed by ionizing radiation.

When fast ions traverse a biological medium, they eject electrons from atoms and molecules producing free radicals in a similar way to any other kind of ionizing radiation. As a consequence, ions cause deleterious effects to those irradiated cells by damaging their macromolecules and cell structures. Several important effects are observed which range from damage of individual cells to damage of whole animal or human organs. The damage of DNA which can eventually lead to cell death thus shortening the natural lifespan of the cell is of great importance. This may be considered as a positive effect when a cancerous tissue is irradiated with a result of tumour shrinkage. Indeed, for longer than a century ionizing radiation has been applied to treat diseases in radiation therapy, specially as a part of cancer treatment. Even though a large number of successful radiation therapy methods has been conceived so far, the enormous complexity of the cell response does not allow a full and error-free description of the biological effects after exposure to radiation.

Various strategies are applied to investigate the effects of radiation fields of ion beams. While early studies were performed with particles emitted by radioactive nuclei, the last decades witnessed the growing role of accelerators to radiobiology experiments and patient treatment. Studies of irradiation of cells and pre-clinical trials with ion beams as well as the progress in accelerator technology led to the development of the most advanced radiotherapy modality today known as ion-beam cancer therapy[2]. It applies beams of protons or carbon ions to treat patients with localized tumours which cannot be removed by surgery. There are several theoretical models which are able to describe the cell response to irradiation. In these models the relative biological effectiveness (RBE) of accelerated nuclei depends on ion mass,

[1] Ion is generally defined as an atom or molecule with a net positive or negative charge. Along all the text, however, the term is restricted to and used as a synonymous for fully ionized atom, *i.e.*, proton or heavier nucleus.

[2] External beam radiotherapy with ions is also usually called particle therapy, hadrontherapy or, more specific to the nuclei applied, proton and carbon-ion therapy.

charge, kinetic energy and cell type.

A powerful method to characterize the interactions of ionizing radiation with biological systems was developed in the field of microdosimetry. The microdosimetry technique is used to measure the fluctuations of energy deposition and associated quantities in single events when ionizing particles traverse a microscopic object. The energy imparted to objects of few micrometres in size which is the typical dimension of the nuclei of mammalian cells is the main quantity measured in microdosimetry. This is done by using a special detector called a tissue-equivalent proportional counter (TEPC) filled by dilute gas to emulate a tissue-like volume of micrometre dimensions and quantify the stochastic energy deposition events. The response function of a TEPC defines the variation of the dose delivered by the radiation field to a nucleus of a cell or other sub-nuclear structure. For this reason, microdosimetry spectrum is a relevant source of information for modelling radiobiological effects.

Theoretical studies of physical processes induced by ionizing radiation in tissue-like media have contributed to the current knowledge of the cell response to ions. Experimental measurements and theoretical modelling are complementary approaches to understanding radiation effects at the microscopic scale. A computational model which is able to simulate the propagation of energetic nuclei in extended media serves as a powerful tool in investigating these effects. Calculations of spatial distribution of energy deposition on macroscopic and microscopic scale by analytical and Monte Carlo methods play a major role in such studies. In particular, patterns of energy deposition around the ion track and the response function of a TEPC can be simulated by the Monte Carlo method.

Future space travels shall take humans to the Moon for extended periods and even beyond the Moon orbit in interplanetary missions. Not only further technological developments are necessary, but also a better understanding of the health risks to crew members exposed to cosmic radiation. Galactic cosmic rays are composed of leptons and hadrons and include nuclei ranging from hydrogen to iron. The exposure to energetic ions in space is a threat to electronic devices and human beings in exploratory missions. Microdosimetric measurements in ground-based facilities and in space flights have been applied for investigations of energy deposition patterns by high charge and energy (HZE) particles. The calculation of microdosimetry spectra by Monte Carlo technique allows to investigate different combinations of particles, energies and shield materials that would be possible with particle accelerators or flight experiments.

Microdosimetry spectra have also been measured for proton and carbon beams for application in radiation therapy. In particular, small size TEPC detectors immersed in tissue-like phantoms allow a spatial characterization of the radiation field inside a patient. Then, radiobiological models can be used to estimate the dose and biological effectiveness both inside and outside the treatment field. This approach can be extended with Monte Carlo to different media and ion beams.

In the present thesis we are mainly concerned with the modelling of radiation fields created by therapeutic ion beams in tissue-like media. A major part of the study is dedicated to physical characterization of ion fields by microdosimetry calculations. Further, modelling of biological effects after ion irradiation is also considered. Our Monte Carlo model for Heavy-Ion Therapy (MCHIT) is applied for modelling the physical interactions of ions with matter. MCHIT is based on the

general-purpose Monte Carlo code GEANT4. Originally being developed for experiments in high-energy physics, the GEANT4 toolkit is now widely used for modelling in medical physics and space research. MCHIT was developed at Frankfurt Institute for Advanced Studies to benchmark GEANT4 physics models for applications in radiation therapy with ions. MCHIT can reproduce well the depth-dose profiles for light nuclei as well as the yields of secondary neutrons and charged fragments in nuclear collisions between the primary ion and nuclei of the medium. Besides, distributions of positron-emitting nuclei relevant for PET monitoring in ion-beam cancer therapy were also successfully calculated with MCHIT. The code has been further developed within the context of the present thesis. The new capabilities include the modelling of microdosimetry measurements for neutrons and ion beams with different TEPCs detectors. Microdosimetry spectra calculated with MCHIT allow us to estimate the biological properties of ion beams by means of a radiobiological model, namely the Microdosimetric-Kinetic model (MKM), which uses microdosimetry data to describe the energy deposition in sub-nuclear cell domains.

Outline of the thesis

- The fundamentals of interactions of ions with matter is discussed in Chapter 1, **Radiation Fields of Ion Beams**. The principles of the microdosimetry technique are introduced along with description of measurements with ion beams performed by other groups. The biological effectiveness of ions is introduced and the radiobiological MKM model, which uses microdosimetric quantities for estimating biological effects of radiation fields of ion beams is presented.

- In Chapter 2, **Monte Carlo Modelling of Radiation Fields**, the Monte Carlo method for modelling of interactions of ions with matter is presented. A general introduction to the GEANT4 toolkit is given. Then, the MCHIT model, which is used in the following chapters for the description of radiation fields of ion beams, is presented.

- Simulations of microdosimetry measurements of nuclei from galactic cosmic rays are presented in Chapter 3, **Microdosimetry for HZE Particles from Cosmic Rays**. Electromagnetic and hadronic models in MCHIT are benchmarked with microdosimetry spectra from protons, helium and heavier nuclei. In addition, the yield of secondary nucleons and nuclei in nuclear fragmentation reactions is evaluated.

- In Chapter 4, **Microdosimetry for Ion-Beam Cancer Therapy**, microdosimetry measurements for a pencil-like carbon beam are simulated. Such beams are typical for radiation therapy with active beam scanning. Issues related to the beam size and finite dimensions of the TEPC are investigated. Since microdosimetry data obtained with pure neutron beams are also well described by MCHIT simulations, this model is used to quantify the role played by secondary neutrons produced in the interactions of carbon nuclei with tissue-like media.

- The biological properties of monoenergetic beams of light nuclei, namely protons, helium, lithium and carbon, are investigated with MCHIT+MKM in Chapter 5, **RBE of Monoenergetic Ion Beams**. The possibility to use helium and lithium beams as new modalities for ion-beam radiation therapy is investigated.

- In Chapter 6, **RBE and Cell Survival Fraction for SOBP Ion Beams**, biological properties at spread-out Bragg peaks of light nuclei, namely protons, helium, carbon and oxygen ions are investigated with MCHIT+MKM in the light of possible future beam modalities for radiation therapy. The relative biological effectiveness and survival fraction of cells for different tissue radiosensitivities are calculated.

- The results of all investigations are summarized in Section 6.2.4 **Summary**. Besides, the outlook for further developments and applications of MCHIT is also presented.

Chapter 1

Radiation Fields of Ion Beams

First studies of the interaction of ions with matter were performed using α-particles from radioactive decay and also using cosmic rays. Decades later particle accelerators made available fast ions to investigate the fundamental properties of matter. Nowadays nuclear beams are used for ion implantation, production of isotopes and ion-beam cancer therapy.

Accelerated ions are ionizing radiation. It means that when they travel trough a medium they lose energy in ionization of atoms and molecules. The impact of radiation on living cells is twofold: on the one hand it is a health hazard which should be avoided using radiation protection techniques; on the other hand it is valuable for radiotherapy purposes where the killing effect of ions is used to control tumour growth. In both cases the understanding of radiation induced by interaction of ions with matter is of uppermost importance.

The spatial distribution of energy deposition in the medium caused by the passage of ions is continuous along beam axis only at macroscopic scale. The microscopic pattern of discrete energy deposits depends on the radiation quality, *i.e.*, particle type and energy. Besides, the radiation effect observed for a given amount of energy deposited in the medium depends on a specific pattern how the energy is deposited (*e.g.*, number of events, distribution of energy deposits in each event or spatial distribution of the interaction points). This means that knowledge of the total energy deposition (physical dose) alone is not enough to predict the radiation effect, but also understanding a comprehensive picture of the interactions of the radiation field with the medium is necessary. A summary of the relevant physical processes taking place during the ion penetration through matter is presented in Section 1.1.

The impact of ionizing radiation on eukaryotic cells is defined by the energy imparted to the cell volume (*i.e.*, by the absorbed dose) and the total number and spatial correlations of local energy deposits to DNA molecules inside the cell nucleus. Such deposits lead to spatially distributed DNA lesions caused mainly by free electrons which surround a track of a fast ion. The pattern of stochastic impacts on DNA resulting in single, double or more complex breaks of DNA strands essentially depends on the projectile charge, mass and velocity. It is defined by the number of electrons per unit of the track length as well as on their energies. All these characteristics differ for photon, electron, proton and nuclear beams. In particular, carbon nuclei successfully used for treating localized tumours are characterized by elevated biological effectiveness in the Bragg peak region as compared to photons

and protons [1, 2]. This difference has been associated with a much higher density of ionization events for low-energy carbon ions resulting in more complex damages to DNA. Thus, not only the delivered physical dose but also the respective biological effects of ion beams should be taken into account while developing treatment planning systems used in ion-beam cancer therapy [3–5].

Since DNA molecules are typically confined inside cell nuclei, which are structures of a few-micrometre size, it is desirable to study energy deposition patterns on the micrometre scale. In particular, the in-beam microscopy is used in experiments on irradiation of living cells. With this tool, the tracks of charged particles can be well explored, when they are visualized by biological markers for DNA damage [6]. Measurements of stochastic energy deposition events by radiation to objects of micrometre dimensions is the speciality of microdosimetry. The patterns of energy deposition at this scale can be transferred to radiobiological models of cell response to radiation. In this thesis, microdosimetry calculations are used to characterize the stochastic distribution of energy deposition by ions. Section 1.2 presents the technique and relevant experiments with ion beams.

In many applications the correct estimation of the energy imparted by ions to the medium should be complemented by predicting respective biological effect. In the case of ion-beam cancer therapy, for example, physicians should prescribe the dose required for tumour control while keeping the dose to healthy tissues as low as possible to avoid normal tissue complications. Therefore, the response of cells to radiation has to be modelled prior the treatment to prevent undesirable outcomes. As fast ions are also found in the galactic cosmic rays, their radiation effects will play a special role in assessing the risks of future space missions. In addition to causing deleterious effects to instruments of the spacecraft, they also impose health risks on crew members. In Section 1.3, different approaches for modelling of radiation effects by ions on biological systems are reviewed. Special attention is given to a particular model, used in this thesis, which applies microdosimetry data to estimate the biological effectiveness of ions.

1.1 Interaction of ions with matter

When ions penetrate matter they interact with the constituents of the medium. In successive collisions ions are mainly subjected to scattering (angular deflection), stopping (loss of kinetic energy) and nuclear reactions (production of secondary fragments). Figure 1.1 presents a few physical processes relevant to radiation therapy and space flights, namely excitation and ionization of target atom or molecule, multiple scattering and nuclear fragmentation. The probability of each process depends on ion specie, energy and medium and it is defined by the cross section.

Electromagnetic collisions are the dominant processes due to the larger range of the Coulomb force compared to the nuclear forces. A high energy transfer to target electrons may be sufficient to eject them in ionization events while a lower energy transfer leads to atomic excitations only. High-energy ions create a sort of electromagnetic cascade in which several fast electrons (known as δ-electrons or δ-rays) are generated and take part in the energy transfer to the medium. The interaction points are distributed randomly around the ion track. In addition to

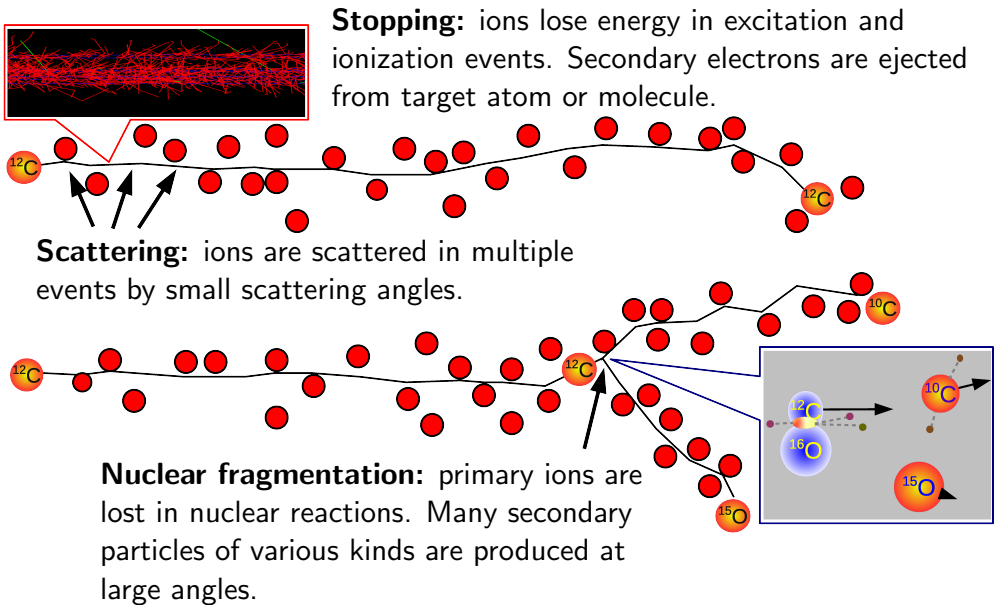

Figure 1.1: Main physical processes taking place during the ion propagation in matter in the energy range relevant to ion-beam cancer therapy and space research.

these energy-loss processes, elastic scattering of ions in collisions with the nuclei of target atoms and molecules take place throughout the penetration. The succession of many scattering events gives rise to the observed divergence of a collimated ion beam.

Despite of a much smaller cross section, nuclear reactions also play a role. They happen when the nuclei from the incoming ion and a target atom overlap. A substantial fraction of primary ions may be lost in nuclear collisions. Besides, secondary nucleons and excited nuclei are produced with broad energy and angular distributions impacting the spatial distribution of energy deposition.

Primary physical interactions are followed by a succession of chemical and biological processes. Ionized atoms and molecules interact chemically and further dissipate the energy absorbed by the passage of fast ions. Such a chain of reactions can cause relevant biological consequences at a later time due to modifications of biological structures. Physical, chemical and biological interactions take place on well separated time scales. In this thesis, physical interactions are explicitly simulated using a computational model while observed biological effects resulting from chemical and biological reactions are estimated using a radiobiological model.

1.1.1 Cross section

A central concept in the modelling of penetration of ions in matter is the probability of each collision type between the particle being transported (primary ion or its secondary particles) and the constituents of the medium. The probability of a given interaction process is governed by an effective area σ called cross section. Different cross sections are observed for each outcome of a collision (*e.g.*, scattering or nuclear fragmentation).

1.1.2 Stopping

There are different processes leading to energy loss of ions penetrating matter. For example, excitation and ionization of target atoms or molecules, momentum transfer to target nuclei, changes in the internal state of the projectile or emission of radiation are some of them. The main mechanisms for energy loss are classified as electronic energy loss and nuclear energy loss. Electronic energy loss (electronic stopping) is characterized by the transfer of kinetic energy of the projectile to potential or kinetic energy of target electrons in excitation or ionization, respectively, of atoms or molecules of the medium. Differently, nuclear energy loss (nuclear stopping) happens due to the momentum transfer to target nuclei. A specific contribution of each mechanism depends on the kinetic energy of the projectile. At high projectile energy, the electrons of the target can be considered as free and the electronic stopping dominates. However, as the projectile gets slower, the binding energy of target electrons cannot be neglected in modelling collisions and the contribution from electronic stopping decreases. Finally, at low kinetic energy the nuclear stopping dominates the energy-loss process.

The energy loss of particles penetrating a given thickness of matter is characterized by the stopping force (stopping power). This quantity is a property of the stopping medium and it is defined as a ratio dE/dx of the energy loss to the penetration length. Ions of hundreds of MeV per nucleon energy are relativistic. At these ion velocities the energy-loss rate in the slowing-down process is dominated by electronic stopping and can be well described by the relativistic version of the Bethe-Bloch formula:

$$-\frac{dE}{dx} = \frac{4\pi e^4 Z_t Z_p^2}{m_e v^2}\left[\ln\frac{2m_e v^2}{\langle I\rangle} - \ln\left(1-\beta^2\right) - \beta^2 - \frac{C}{Z_t} - \frac{\delta}{2}\right] , \qquad (1.1)$$

where Z_p and Z_t denote the nuclear charges of the projectile and target, m_e and e are the mass and charge of the electron, $\langle I\rangle$ is the mean ionization potential of the target atom or molecule, C/Z_t is the shell correction term, and $\delta/2$ the density effect correction [7].

Equation (1.1) presents a $dE/dx \sim 1/v^2$ dependence which results in the increase of the energy-loss rate with stopping of the ion. Ions present a well defined maximum of stopping power close to the end of the particle track known as Bragg peak, named after Sir William Henry Bragg who first observed this effect in the stopping of alpha particles in air, in 1903. In particular, dE/dx reaches its maximum value for carbon ions at specific energy of 350 keV/u [7]. The presence of Bragg peak justifies the use of ions to treat localized tumours in radiation therapy due to the possibility of reducing dose to healthy tissues while keeping the same clinical dose to the target volume as in photon radiation.

At very low kinetic energies, $E \leq 10\,\mathrm{keV/u}$, nuclear energy loss dominate the stopping process. Ions travel only few micrometres before complete stopping. For most applications, however, the partial contribution of nuclear stopping to the total energy deposition can be neglected [7].

1.1.3 Scattering

Elastic collisions between the ion and atomic nuclei results in deviations of the ion direction. The scattering angle of ions in each individual encounter is typically very small specially in comparison to the scattering of particles with much lower mass as electrons. Nonetheless, the cross section for elastic scattering is large resulting in many successive deflections for ions crossing extended medium. Therefore, the build-up of many successive scattering collisions along the penetration leads to relevant divergence of the initial direction of the ion. The divergence of the ion beam is responsible for a penumbra of the lateral dose distribution depositing energy to healthy tissues in the vicinity of the tumour in ion-beam cancer therapy. Because the scattering is smaller for heavier particles, carbon ions show a smaller spread of the dose for deep seated tumours compared to protons. The modelling of the lateral spread of the dose is important for estimating the dose to organs at risk. Due to the large number of small deviations, the modelling of the scattering process is usually performed using an approach called multiple Coulomb scattering. It considers only the global effect after a given track length, *i.e.*, the net scattering angle, instead of simulating each individual scattering event.

1.1.4 Nuclear fragmentation

An ion with kinetic energy above few MeV per nucleon can overcome the Coulomb barrier and overlap with the nucleus of a target atom. This process is not frequent when ions cross a thin layer of material. It can be explained by a small geometrical nuclear cross section and a short range of nuclear forces. The situation changes when the thickness of the medium increases as found in ion-beam cancer therapy and irradiation of spacecraft by galactic cosmic rays. At ion energies of several hundreds MeV per nucleon and ions traversing thick materials, the impact of nuclear reactions cannot be neglected. In this case a considerable fraction of the ions undergo nuclear collisions before fully stopping in the medium. Such violent nuclear reactions are characterized by partial of full overlap of the interacting nuclei. An internal exchange of energy and momentum between the participant nucleons redefine the configuration of the nuclear system. Emission of nucleons and fragmentation of the nuclei give rise to a zoo of secondary particles which may have enough energy to penetrate further into the medium.

1.2 Microdosimetry of ion beams

The microdosimetry technique originated from the efforts of Harald H. Rossi and co-workers in the 1950's to describe the microscopic picture of energy deposition in irradiated matter. The theoretical concepts and experimental technique were developed further and compose nowadays a well-established field for description of the interactions of radiation with matter and the subsequent effects [8].

Detectors are used to measure the energy deposition in a sensitive volume per passage of a single ionizing particle of the radiation field. In particular, small chambers filled with low-pressure gas are employed. When an ionizing particle cross the gas chamber of the detector it ionizes gas molecules. The measurement is based on

the counting of electrons from electron-ion pairs created in such ionization events. The ejected electrons are driven by electric potential applied to a collector wire. The detector operates with a high electric potential in order to amplify the signal by promoting electric avalanches near the collector wire. The charge collected in each event is proportional to the number of primary ionizations induced by the passage of the particle. Therefore, the measured electronic signal can be converted to the energy imparted in each energy deposition event [9, 10].

The principle of microdosimetry is that the energy deposition in a low-density medium by a traversing particle is the same as the energy deposition when traversing an equivalent volume of smaller dimensions but higher density. This is possible by choosing properly the chemical composition of the gas and detector components. Then, the ratio of the diameters of the gas chamber and the tissue-equivalent volume is proportional to the ratio of the densities of the tissue-equivalent medium and the gas. A detector applying this principle is called tissue-equivalent proportional counter (TEPC). The cavity, filled with low-pressure tissue-equivalent gas, is used to emulate a tissue-equivalent region of a micrometre size (the density of liquid water is commonly used as a reference for human tissue). In this way, the energy deposited to the sensitive gas volume of this device can be related to the energy that would be deposited to a cell nucleus or even to a smaller volume [8].

1.2.1 Basics of microdosimetry technique

Several concepts were introduced in the microdosimetry technique to relate the features of the spatial distribution of energy deposition in the medium to the size of structures being affected [8]. In particular, the cell nucleus or a sub-nuclear structure of few micrometre in size is considered as a fundamental target of the ionizing radiation. Due to the stochastic nature of interactions of particle with matter [8] the amount of energy ϵ delivered to the TEPC sensitive volume representing such a target by particles traversing the detector fluctuates. The response function of the detector gives the probability density distribution for the imparted energy $f(\varepsilon)$. Such distribution is sensitive to the radiation quality and it can be used to characterize it.

In microdosimetry energy deposition events are characterized by the lineal energy $y = \varepsilon/\bar{l}$, where $\bar{l}$ is the mean chord length of the detector chamber, and the specific energy $z = \varepsilon/m$, where m is the mass of the tissue-equivalent region. If one assumes that particles representing a homogeneous radiation field traverse a spherical sensitive volume of diameter d randomly at various impact parameters, then $\bar{l} = 2d/3$. The lineal energy is a stochastic quantity analogous to linear energy transfer (LET), giving a ratio of energy deposition per track length. LET has been commonly applied to characterize radiation effects. However, there are limitations regarding the use of this quantity to describe the effects induced in microscopic structures such as cells. On the contrast, the lineal energy seeks to overcome this limitation.

The probability density $f(y)$ as well as its first and second moments are commonly used to investigate radiation fields. The frequency-mean lineal energy $\bar{y}_F$, given by

the first moment of the $f(y)$-distribution

$$\bar{y}_F = \int_0^\infty y f(y) \mathrm{d}y \ , \tag{1.2}$$

serves as a measurable approximation for LET. The second moment, called dose-mean lineal energy $\bar{y}_D$, is related to the quality of radiation. It is calculated as

$$\bar{y}_D = \int_0^\infty y d(y) \mathrm{d}y = \frac{1}{\bar{y}_F} \int_0^\infty y^2 f(y) \mathrm{d}y \ , \tag{1.3}$$

where $d(y) \equiv y f(y)/\bar{y}_F$ is defined as the dose probability density. In order to account for the saturation of biological effects induced by high-LET radiation, a quantity called saturation-corrected dose-mean lineal energy y^* was also introduced,

$$y^* = \frac{y_0^2 \int_0^\infty \left[1 - \exp\left(-y^2/y_0^2\right)\right] f(y) \mathrm{d}y}{\int_0^\infty y f(y) \mathrm{d}y} \ , \tag{1.4}$$

where y_0 represents a saturation parameter.

For a spherical sensitive volume filled with gas, the total dose D is given by a useful formula [8]:

$$D = \frac{0.204}{d^2} \bar{y}_F \ . \tag{1.5}$$

Here d corresponds to the diameter of the sensitive volume expressed in µm, $\bar{y}_F$ in keV/µm and D is obtained in Gy.

Probability distributions and average quantities are also defined for z. The specific energy is also a stochastic quantity, however it can represent the summation of energy imparted in more than one event. For this reason, the average quantities from the $f(z)$-distribution do not represent the fluctuations of z in single events. In particular, the frequency-mean $\bar{z}_F$ and dose-mean $\bar{z}_D$ specific energy per event are defined as

$$\bar{z}_F = \int_0^\infty z f_1(z) \mathrm{d}z \ , \tag{1.6}$$

$$\bar{z}_D = \frac{1}{\bar{z}_F} \int_0^\infty z^2 f_1(z) \mathrm{d}z \ , \tag{1.7}$$

where $f_1(z)$ is the single event distribution of z [8].

1.2.2 Measurements with TEPC

Since many years measurements with TEPC [8] are considered as a practical tool for studying patterns of energy deposition to micrometre-size objects by various kinds of radiation. As demonstrated by several authors, see *e.g.* Refs. [11, 12], microdosimetric variables are directly related to the radiation quality factor used to quantify risks from various kinds of radiation. TEPCs are commonly applied for microdosimetric measurements in radiation environments such as radiation therapy and space dosimetry.

There were several experimental [13–15] and theoretical [16, 17] studies of TEPC responses to ions. In these measurements and calculations the dependence of ϵ on

the impact parameter of the ion track was investigated in detail. As demonstrated by Taddei and co-authors [17], Monte Carlo calculations based on the GEANT4 toolkit can successfully reproduce the performance of a walled TEPC irradiated by ^{4}He, ^{12}C, ^{16}O, ^{28}Si and ^{56}Fe nuclei.

Due to its compactness the TEPC device can be located at various positions inside and outside of phantoms irradiated by therapeutic beams. Microdosimetry measurements with a monoenergetic 400 MeV/u ^{12}C beam [18] were made together with the identification of charges of secondary fragments by scintillation counters by the time-of-flight method. In this way the microdosimetry technique supplements the measurements of fragment yields by particle identification made outside the phantom with more bulky detectors, see *e.g.* Ref. [19]. Further measurements were performed with phantoms irradiated by 290 MeV/u ^{12}C beam with a traditional walled TEPC [20], also with fragment charge identification. Microdosimetry measurements without tagging fragments using spread-out Bragg Peaks (SOBP) for 160 MeV proton, 150 MeV/u ^{4}He and 290 MeV/u ^{12}C beams were also reported [3, 4]. Recently, a wall-less TEPC was applied for microdosimetry measurements [21, 22] of monoenergetic 160 MeV proton, 150 MeV/u ^{4}He, 290 MeV/u ^{12}C and 490 MeV/u ^{28}Si beams. In all these experiments the TEPCs were located on the beam axis characterizing, therefore, the energy deposition in a region under direct irradiation.

Microdosimetry measurements were reported [23] on the beam axis as well as off-axis in a water phantom irradiated by pencil-like 185 MeV/u ^{7}Li and 300 MeV/u ^{12}C beams. Similar studies at carbon-ion and proton radiotherapy facilities with passive beam delivery were also performed at TEPC positions outside the treatment field [24].

All the aforementioned microdosimetry data challenge the theoretical methods aimed to describe particle transport in matter and energy deposition at the micrometre scale. They provide information which can be used in benchmarking various physical models of interactions of ions with tissue-like media.

1.3 Radiation effects induced by ions

Biological effects induced by ions are initiated by the ionizations caused by these particles along their passage through living cells. Electrons are ejected from the atoms and molecules present in the sub-nuclear structures and thus create free radicals. Such radicals are highly reactive and seek an electron for chemical stabilization which might create a reaction chain. The biological impact is either caused by structural changes at the time of initial physical impact or due to chemical and biological reactions induced by free radicals.

Ionizing radiation is known to damage DNA. The structure of the DNA can be directly affected by hitting it by ions and δ-electrons. Besides, reactive atoms or molecules existing in the surrounding medium may also harm it by indirect processes. Cells have their own mechanisms to repair DNA damages. The success of the repair process depends on the complexity of the damage which triggers the cell response. The repair of complex damages is error-prone and results either in cell death or alteration of the genetic code. In particular, low-energy carbon and heavier nuclei cause a high density of ionizations along their tracks which increases the

probability of complex damages. Numerous secondary electrons produced by the ion passaging the nucleus of a cell accounts for a high probability of hitting the DNA more than once in a small segment of its double-helix structure. This leads to a higher number of double or complex strand breaks compared to irradiations with protons or photons. The repair process becomes troublesome and the odds of the cell dying increases. In the case of a mutation, however, the cell may be unable to reproduce itself or, in the worst scenario, the damage may trigger a reproduction at an uncontrolled rate or other cancer manifestations. If the damage is not complex enough to determine cell death, the risk of cell mutation due to miss-repair increases.

The prediction of the radiation effects for each specific irradiation scenario is a key problem in radiobiology and radiation protection. The effects depend on several variables including the quality of the radiation field as well as intensity and duration of exposition[1]. Besides, observed effects can be deterministic or stochastic. Radiation effects caused by acute dose are well known. A high dose received at once harms many cells causing a misfunction of tissues and organs which might lead to the subject's death. Such effects are mostly deterministic and the severity of the outcome is highly correlated with the amount of dose received. Radiation syndromes present well-known dose thresholds. When a threshold is overcome, all individuals of a population demonstrate similar effects. On the other hand, apart from cataract formation, effects due to chronic exposure cannot be directly determined. They are stochastic and their outcomes are estimated only with a certain probability. The risk of developing cancer after chronic exposure is an example of stochastic effect, while radiation "sickness" or nausea, skin reddening and sterility are examples of deterministic effects after acute exposure.

In space missions crew members may be subject to acute exposure during a major solar particle event. Even though they can be protected by storm shelters while inside the spacecraft, they will most likely develop radiation syndromes if exposed during an extravehicular activity. Additionally, cosmonauts receive constantly a chronic dose from galactic cosmic rays. This is a matter of great concern for long-term health problems to crew member under exposure to space radiation.

In proton and carbon-ion therapy a high and localized dose is applied to treat deep seated tumours, specially those close to organs at risk when conventional radiotherapy with photons impose higher risks to the patient. Health tissues in the beam path, however, are also subject to a substantial dose which might result in normal tissue complications. Relatively small doses delivered to those tissues outside the treatment field due to secondary particles like neutrons may also cause long-term effects such as the development of secondary malignancies. Decreasing the probability of late effects in ion-beam cancer therapy is crucial to paediatric patients.

Knowledge about cell and tissue responses to radiation has been developed along many years of conventional radiotherapy and from cohort studies of the nuclear bomb survivors. In addition, radiobiological experiments help to evaluate the dependence of cell response on specific irradiation conditions. For instance, it has been demonstrated that cells do not present the same radiation effect for a given dose when irradiated by photons or ions. The so-called relative biological effectiveness

[1]Radiation exposure is usually classified as acute or chronic. An acute exposure means that a high dose was received in a short period of time while in chronic exposure the dose is received in a much longer period.

(RBE) was defined to specify the difference in biological effect between two radiation fields. This was a necessary step to translate the long experience developed in radiation therapy with photons to treatment planning for ion-beam cancer therapy. For such an application, however, it is also important to be able to predict the biological effects from model calculations so that a physician can choose the best treatment parameters (*e.g.*, number of beams, angle of incidence and the like). Different radiobiological models have been developed which can be integrated in treatment planning systems to account for RBE variations at different positions of the ion field.

1.3.1 Relative biological effectiveness

The results of irradiation of biological structures depend both on the characteristics of the radiation field and the medium being irradiated. For a given received dose the effect might not be the same when the particles present different LET values or track structure (which is a function of charge and velocity of the particle). The survival fraction of cells S after the impact of the radiation dose D can usually be well represented by the linear-quadratic (LQ) model:

$$S(D) = \exp\left[-\alpha D - \beta D^2\right] , \tag{1.8}$$

where α and β are model parameters. The ratio α/β characterizes the radiosensitivity of the cells. In the case of photon radiation, early responding tissues present typical values of $\alpha/\beta \sim 10$ Gy while $\alpha/\beta \sim 2$ Gy is characteristic for late responding tissues [25]. Figure 1.2 shows typical curves for survival fraction of cells when irradiated by photons and heavy ions. At the same dose level the survival fraction is

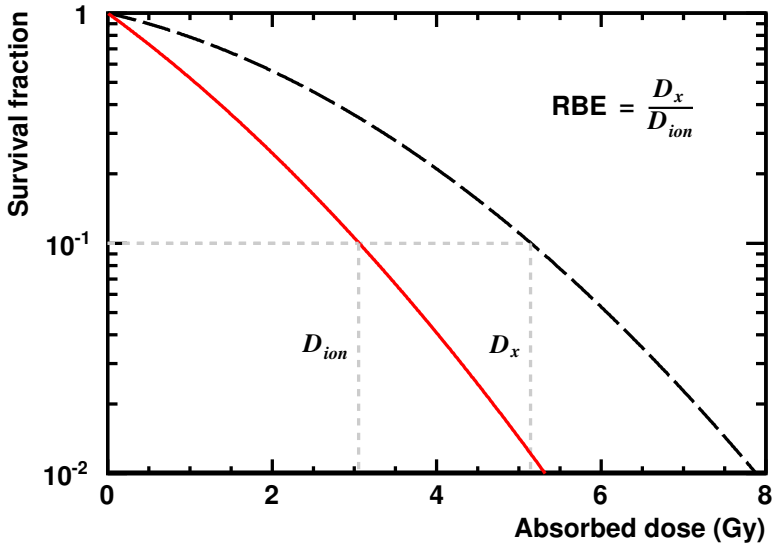

Figure 1.2: Typical survival fraction of cells when irradiated by heavy ions (solid line) and photons (dashed line).

always smaller when the cells are irradiated by photons. Likewise, the same survival fraction is attained with less dose when irradiating with heavy ions. In order to

quantify the physical dose D_{ion} required by ions to produce the same effect as the physical dose D_x for a reference radiation field (typically x-rays or gamma rays) the RBE is used, where:

$$\mathrm{RBE} = \frac{D_x}{D_{ion}} \tag{1.9}$$

The RBE depends not only on particle type, but also on energy, dose level, cell or tissue type and biological endpoint [26–29]. The product of RBE and physical dose is called biological dose or isoeffective dose (expressed in unit of GyE which stands for gray-equivalent). In ion-beam cancer therapy, the change of RBE along the irradiated volume must be considered in order to deliver the prescribed clinical dose to treat the target volume and estimate correctly the side effects to healthy tissues.

Assuming that the survival fraction of cells after their irradiation by photons and ions can be described by the linear-quadratic model, one can show that

$$\mathrm{RBE} = \frac{2D_x}{\sqrt{\left(\frac{\alpha_{ion}}{\beta_{ion}}\right)^2 - 4\frac{1}{\beta_{ion}}\ln S} - \frac{\alpha_{ion}}{\beta_{ion}}}, \tag{1.10}$$

where D_x is the delivered dose by photons at survival fraction S and α_{ion} and β_{ion} are the LQ-model parameters for the ion field. It has been shown that the RBE is mainly determined by the α_{ion}/β_{ion} ratio [30]. In case the parameters α_{ion} and β_{ion} are known, Eq. (1.10) can be used to calculate the RBE and the required D_{ion} by the ion field to yield the same survival fraction S as obtained with D_x.

The RBE dependence on the radiation field can be estimated either in experiments or by modelling. The first approach consists in *in vitro* biological experiments where cell cultures are irradiated in well-defined conditions. As for RBE estimations for ion-beam cancer therapy, a large number of irradiation conditions need to be investigated in order to consider the different scenarios which are patient specific. Not all possible scenarios can in fact be investigated. Besides, cells behave differently when exposed to irradiation *in vitro* or *in vivo*. Consequently, some compromise should be taken in this case. The second approach relies on the modelling of the biological response to the irradiation conditions using *ab initio* calculations or phenomenological models. Modelling allows estimating radiation effects induced by ions at various clinical scenarios and it has been integrated in treatment planning procedures [30].

1.3.2 Modelling of biological effects

Models for the estimation of biological effects due to ionizing radiation have been developed for many years applying different strategies. The so-called mechanistic method is used to describe the impact of radiation from first principles by modelling the complete chain of physical, chemical and biological processes [31, 32]. While the induction of DNA damages can be reasonably well simulated by *ab initio* calculations, such models ultimately fail in describing the complex response of the cell in the processing and repair or misrepair of the initial damages. These biological mechanisms are characterized by highly regulated and not well-understood networks

of different interacting proteins. Up to now the mechanistic models do not achieve the level of precision sufficient for clinical applications [30].

An alternative and rather simpler strategy is to apply a phenomenological description of the radiation effect which does not require a detailed modelling of the repair mechanisms that follow the radiation insults. For example, one could be interested in modelling the difference in radiation effectiveness between photons and ions while using the cell response after photon radiation (*e.g.*, the survival curve) as an input to the model. In this way, the complex repair mechanisms are indirectly accounted in the effect caused by photons and the problem is reduced to the modelling of RBE.

The phenomenological approach sketched above is used in the well-known Local Effect Model (LEM) [30]. In order to model the biological effect for a particular cell type and endpoint after ion irradiation the corresponding cell response to photons is used. It is considered that the impact of radiation to a small sub-volume (nanometre dimensions) of the cell nucleus is solely due to the pattern of energy deposition in this region and it does not depend on the type of particle which deposited energy. The main assumption is that equal local doses correspond to equal local effects. In order to estimate the radiation effects induced by ions, the local dose for infinitesimally small regions inside the nucleus is obtained from an amorphous track structure model which gives the radial dose profiles expected for the ion tracks. The number of lethal lesions created in each sub-volume of the cell nucleus is calculated using the local dose and the cell survival curve after photon irradiation. Therefore, the difference between the biological actions observed for photons and ions is due to their peculiar spatial energy deposition patterns inside the cell nucleus, *i.e.*, the RBE is related to the track structure.

Another model widely used for estimating biological effects induced by ions is the Microdosimetric-Kinetic Model (MKM) [33–35]. It relates the impact of stochastic energy depositions in μm regions of the cell nucleus with the creation of repairable and lethal lesions. This approach allows to apply experimental microdosimetry data to the modelling of biological effects [36]. Due to the fact that microdosimetry is employed in this thesis to characterize the physical interactions of ions with matter, the MKM is discussed in more details below and further used to model biological properties of ion beams.

It has been shown that LEM and MKM provide a good description of different experimental data for cell survival [36]. This justifies the use of these two models for RBE calculations in ion-beam cancer therapy. In addition, the simplicity and computational speed of the calculations presented by both models make them suitable for integration in treatment planning systems [36].

Microdosimetric-Kinetic Model

The MKM [33–35] uses a phenomenological approach for the description of the biological effects that follow the initial physical insults in cells due to ionizing radiation. The theory combines a microdosimetric description of energy deposition events in compartments of a cell nucleus called domains with a kinetic description of creation and repair of radiation-induced lesions. The domain is conceived as a sub-micrometre volume containing DNA. Inside this domain the ionization events

are able to create lesions. The dose received by a domain after exposure to ionizing radiation is a random quantity. Lesions created in a domain are proportional to the microscopic dose absorbed in its volume and to the DNA content of the domain.

Two types of lesions can be produced, type I and II. The first type is unrepairable and lethal to the cell. The second type is repairable but can be transformed into the type I by a few processes. It is postulated that type II lesions can diffuse through the domain and may interact in pairs to produce a type I lesion before the repair mechanism takes place. The domain acts as a microscopic reaction vessel, *i.e.*, primary DNA lesions and their transformations takes place in this region [34]. By definition type II lesions can only interact with those from the same domain. Thus, the domain gives a measure of separation of primary lesions that can interact with finite probability before they are removed by repair. The size of a domain has been estimated as being of the order of 0.5–1.0 μm using the relationship between RBE in the limit of zero dose and LET [35].

A mathematical description of the processes of creation of type I and type II lesions and transformations of type II lesions is formulated using mass action kinetic equations. Solving the equations for the case when the average number of lesions per domain is small – approximation valid for doses much less than 125 Gy, usually the case in mammalian cellular radiobiology and radiation therapy [34] – one obtains the number of lethal lesions L per cell as

$$L = (\alpha_0 + \beta \bar{z}_D)\, D + \beta D^2 \ , \tag{1.11}$$

where $\bar{z}_D$ is the dose-mean specific energy deposited by a single event in the domain, α_0 is a function of the number of type I and type II lesions produced per gray per cell and β is a function of the number of type II lesions produced per gray per cell [35]. Assuming a Poisson distribution of lethal lesions among the cells, the survival fraction of cells can be expressed as

$$\begin{aligned} S &= \exp\left[-L\right] \\ &= \exp\left[-\left(\alpha_0 + \beta \bar{z}_D\right) D - \beta D^2\right] \\ &= \exp\left[-\alpha_P D - \beta D^2\right] \ . \end{aligned} \tag{1.12}$$

The effect of increasing LET on cell survival is modelled by $\bar{z}_D$ confined in the value of the α_P parameter. The β parameter in the quadratic term is independent of radiation quality (LET). In this approximation of Poisson distribution of lethal lesions, the theory implies that the survival curve for high-LET radiation, that looks linear (β equal zero), is of linear-quadratic form with the same value of β corresponding to the survival curve for low-LET radiation. This is possible due to a larger value for the α_P parameter which is mainly affected by fluctuations of energy deposition on the domains [33].

Comparison of model predictions using Eq. (1.12) with experimental observations of cell response to radiation shows that MKM gives a generally true picture of the process of radiation-induced cell death [34]. However, the linear-quadratic relation for the surviving fraction of cells as presented above is only valid for low-LET radiation where the distribution of lethal lesions follows a Poisson distribution [33]. It ultimately fails to describe the overkill effect as the LET increases above hundreds

of keV/µm. In order to correct for this effect, a non-Poisson distribution of lethal lesions in the nucleus of the cells is considered [35]. It is postulated that increasing the LET will induce non-random clustering of lethal lesions in some cells deviating from a Poisson distribution of lesions. This non-random clustering of lesions accounts for some cells that do not receive any dose, allowing them to survive [35]. In this extension of MKM to high-LET radiation, the picture of domains is replaced by a sensitive nuclear volume which refers to a region of the nucleus including all the DNA content and the surrounding medium where reactions may lead to DNA lesions. The clustering is then considered to happen inside the sensitive nuclear volume and it is shown that the mean number of lethal lesions per cell is given by

$$L = \alpha^* D + \beta D^2 \ , \tag{1.13}$$

with

$$\alpha^* = (\alpha_0 + \beta \bar{z}_D) \left\{ \frac{1 - \exp\left[- (\alpha_0 + \beta \bar{z}_D)\, \bar{z}_{Dn} - \beta \bar{z}_{Dn}^2 \right]}{(\alpha_0 + \beta \bar{z}_D)\, \bar{z}_{Dn} + \beta \bar{z}_{Dn}^2} \right\} \tag{1.14}$$

where $\bar{z}_{Dn}$ is the dose-mean specific energy per event in the sensitive nuclear volume.

An alternative approach to extend MKM to high-LET radiation was proposed by Kase *et al.* [3]. It replaces the dependence of the linear parameter in Eq. (1.11) on the dose-mean specific energy to

$$L = (\alpha_0 + \beta z_{1D}^*)\, D + \beta D^2 \ , \tag{1.15}$$

with

$$z_{1D}^* = \frac{1}{\rho \pi r_d^2} y^* \ , \tag{1.16}$$

where ρ and r_d are the density and radius of a domain, and y^* is the saturation-corrected dose-mean lineal energy (see Eq. (1.4)). This modified version of MKM allows to use microdosimetry spectra measured by TEPCs emulating a domain to estimate survival fraction of cells and RBE for high-LET radiation as those from ions.

The modified MKM is used in this thesis to model the biological effects induced by ions on the basis of microdosimetry spectra. In particular, the endpoint of 10 % survival fraction of cells was chosen for calculating RBE at different positions inside the radiation field. Then, using Eq. (1.10) and taking $S = 0.1$,

$$RBE_{10} = \frac{2 D_{x,10}}{\sqrt{\left(\frac{\alpha_{ion}}{\beta_{ion}} \right)^2 - 4 \frac{1}{\beta_{ion}} \ln 0.1} - \frac{\alpha_{ion}}{\beta_{ion}}}, \tag{1.17}$$

with

$$\alpha_{ion} = \alpha_0 + \frac{\beta}{\rho \pi r_d^2} y^* \ , \tag{1.18}$$

$$\beta_{ion} = \beta \ , \tag{1.19}$$

where α_0 and β are obtained from a reference radiation field and y^* is calculated from the microdosimetry spectrum. Equation (1.18) establishes a common relationship between y^* and the α-parameter of the linear-quadratic model irrespective of the

specific ion species. This relation reflects the fact that an excessive local energy deposition is inefficient to boost a given biological effect [8]. It leads to the reduction of the RBE estimated for very high-LET radiation. As shown in Refs. [3, 37], the microdosimetric parameter y^* is well suited to estimate the α-parameter for human salivary gland (HSG) cells and other cell lines for a large variety of projectiles including proton, helium, carbon and neon nuclei. Therefore, the RBE values for various therapeutic beams can be obtained from the corresponding microdosimetry spectra.

Chapter 2

Monte Carlo Modelling of Radiation Fields

The modelling of interactions of ions with matter is relevant to many applications. One could be interested in predicting, for example, the radiation hardness of components in the design of a new satellite which will be under constant irradiation by nuclei from galactic cosmic rays. Another particular problem is the precise estimation of the treatment dose for a patient under ion-beam cancer therapy which is required to kill a tumour while sparing as much as possible healthy tissues.

In order to study the interaction of radiation with matter, a number of dedicated radiation detectors have been designed. However, it is not always possible to use an experimental approach. For example, it is impossible to place detectors inside a patient's body to obtain profiles of the absorbed dose. In such cases theoretical modelling is more appropriate. Various modelling procedures can be applied depending on what is being investigated. Analytical calculations can be used among other things to estimate the average energy deposited by ions along the penetration depth. However, if one is interested, for example, not only in the average value but also in the fluctuations of energy deposition in some micrometre volume irradiated by a complex radiation field, then a different approach is necessary. In particular, the stochastic nature of the interaction and energy transfer mechanisms naturally leads to the choice of Monte Carlo modelling.

The Monte Carlo method is a statistical approach usually applied to solve problems in mathematics, physics, chemistry, biology, finance and economics. The method has its roots in the Manhattan Project being applied to solve the transport of neutrons for the development of nuclear weapons [38]. It relies on a repeated random sampling procedure for estimating a quantity of interest which can not be easily evaluated by a deterministic approach. It is suitable for simulating stochastic interactions of ions with atoms and molecules of the medium. The general concept of the Monte Carlo modelling of the transport of particles in matter is presented in Section 2.1.

The exponential increase of computational power seen in the last decades fostered the development of a number of Monte Carlo codes for the transport of particles in matter. Such codes are usually very specific and optimized for their particular applications, including among others the transport of particles in treatment planning systems for radiotherapy. However, several general-purpose Monte Carlo transport

codes have also been developed. A few of them, which can be applied for the transport of ions in extended medium, are mentioned in Section 2.2. Special attention is given to the publicly available GEANT4 toolkit. It was applied to build our Monte Carlo model for Heavy-Ion Therapy (MCHIT), described in Section 2.3. The in-house MCHIT code was exclusively developed for investigations related to ion-beam cancer therapy.

2.1 Monte Carlo modelling of particle transport

The transport of a given particle through matter consists in the successive interaction processes between the particle and constituents of the medium, *i.e.*, atoms and molecules. In the Monte Carlo modelling of particle transport, cross sections are used to randomly select the distance of travel to the next interaction point and the kind of process that takes place. The outcome of a given interaction, *e.g.*, energy loss, scattering angle or reaction products, may also be stochastic and needs to be sampled from the corresponding probability distribution. Due to this sampling procedure, pseudo-random number generators play a fundamental role in Monte Carlo transport codes.

Let us consider a photon travelling through a medium. Depending on the photon energy and medium, photoelectric effect, Compton scattering, Rayleigh scattering or pair production happen at different probabilities specified by partial cross sections, σ_k, where k denotes a specific interaction process. The total cross section, σ_{tot}, given by the sum of all partial cross sections, defines the total probability of an interaction and it can be used to estimate the mean free path, λ, for such a photon in the medium. The travel distance (step length), s, to the next interaction point can be sampled using

$$s = -\lambda \ln(1 - \xi), \tag{2.1}$$

where ξ is a (pseudo-)random number, with $0 \leq \xi < 1$. Then, the specific process which takes place at the end of the step is selected by generating a new random number, ξ', and using the cumulative distribution function P_i,

$$P_i = \frac{1}{\sigma_{tot}} \sum_{k=1}^{i} \sigma_k. \tag{2.2}$$

In particular, it is chosen the process of type i which satisfies

$$P_{i-1} \leq \xi' < P_i. \tag{2.3}$$

Thereafter, changes in the photon kinematics are performed by modelling the interaction process. It may lead to the creation of secondary particles, *e.g.*, the ejection of an electron due to the photoelectric effect. After calculating the final state of all particles involved in the reaction, the procedure starts over in order to determine the next step for each particle.

As for the transport of electrons, two different approaches were developed, namely the detailed history approach and the condensed history approach. The first one, known as microscopic approach, simulates explicitly each interaction of each elec-

tron. This approach is applied when the transport of all secondary electrons is important (*e.g.*, in nanodosimetry). However, it can be too time consuming and impractical for many applications due to a huge number of interactions and secondary particles produced which also need to be transported. The condensed history approach was developed to overcome this problem in the case of macroscopic calculations, when the explicit accounting of all secondary particles produced in electromagnetic cascades becomes not feasible or unnecessary. In many applications the simulation of all individual interactions and transport of soft electrons – largest number of secondary electrons ejected in ionizations which travel only few nanometres – do not affect the outcome. Therefore, much more efficient Monte Carlo codes are implemented by grouping individual interaction events and transporting only those secondary particles that may affect the results of simulations. For example, the final effect of small scattering angles in many successive elastic scattering events along a given path can be accounted by one multiple-scattering event reducing the computation time. Likewise, the energy loss in many successive ionization events can be modelled by the stopping-power theory.

The transport of ions can also be modelled in both condensed history or detailed history approach. In addition to accounting for electromagnetic processes, it is also necessary to consider hadronic interactions (*e.g.*, nuclear fragmentation reactions). Therefore, partial cross sections are required for both electromagnetic and hadronic processes in order to sample the step length and the particular interaction process which happens at the next point.

2.2 Geant4 toolkit

The design of modern sophisticated detectors for experiments in particle and nuclear physics is one of the factors which foster the development of a number of general-purpose Monte Carlo transport codes. The versatility of such codes paved the way for a range of applications which are far more extensive than initially foreseen. For example, simulations of radiation fields induced by ion beams in space research and radiation therapy have been performed using such codes, namely FLUKA [39, 40], Geant4 [41, 42], MCNP6 [43], PHITS [44–46] and SHIELD-HIT [47, 48].

The use of Monte Carlo methods in ion-beam cancer therapy has increased significantly in the last decade. In particular, the TOol for PArticle Simulation (TOPAS) [49] based on the Geant4 toolkit provides a user-friendly toolkit for simulations in proton therapy. It has been extensively tested in a variety of proton therapy applications and it has been used at several proton therapy centres worldwide. Such a tool can also be extended for radiation therapy with carbon-ions. Before that, the benchmarking of the models describing the physical interactions in Geant4 or any other Monte Carlo code is crucial in order to verify whether the codes are suitable for such applications.

Geant4 (for GEometry ANd Tracking) is a platform for the simulation of the propagation and interactions of particles in matter [41, 42]. It was originally developed for a new generation of experiments in high-energy physics to be performed at the Large Hadron Collider (LHC). Nowadays, the code is also widely used for

modelling in other research fields like medical physics and space research. The code has been developed and maintained by a worldwide collaboration of scientists and software engineers. The support comes from many universities, laboratories and institutes including CERN, CIEMAT, IN2P3 and INFN in Europe, KEK in Japan, and SLAC, Fermilab and TRIUMF in North America.

GEANT4 comprises software libraries with a broad set of functionalities for the simulation and analysis of particle propagation in various media. It provides an abundant set of physical models to handle the interaction processes over a wide energy range and different particle types. It also includes tools for geometry handling, particle tracking, detector response, visualization and user interface. The source code, written in object-oriented C++ programming language, is freely available from the website of the project, http://geant4.cern.ch/.

In order to perform Monte Carlo simulations using the GEANT4 toolkit, users must implement their own software application using the libraries distributed with the source code. Therefore, a minimum of programming expertise is required in contrast to other general-purpose Monte Carlo codes where users need only to write scripts. A GEANT4-based application can be tailored to the particular research task using only the necessary components of the toolkit. Besides, users are able to change default settings in the platform (*e.g.*, the specific choice of physical models) or they can even implement their own models. Such capabilities of the toolkit do not impose limits to the user.

An implementation of a GEANT4-based application must include, at least, three classes, the so-called detector construction, primary generator action and physics list. The first class, detector construction, specifies the geometry (shape, size and position) and material composition of all the components present in the simulated set-up. In addition, electromagnetic fields can also be modelled in this class. The second class, primary generator action, determines the particle source, *i.e.*, it creates the primary particles to be transported. The third class, physics list, assigns physical processes and models to the particles as well as the associated cross sections. A detailed description of the available physical models is given in the GEANT4 Physics Reference Manual [50]. A set of models which are relevant to a particular problem should be activated by the application developer. Such models are usually grouped in separate physics lists. In order to simplify the choice of physical processes and models, the GEANT4 collaboration provides predefined physics lists adapted to specific application purposes. Therefore, users have the choice of loading predefined physics lists, implement customized physics lists, or even use a combination of these two options.

In addition to the three mandatory classes, the application developer needs to implement classes to handle and score physical quantities of interest, *e.g.*, energy deposition, fluence, energy spectrum and so on. The toolkit provides a number of methods to access such physical quantities at different stages of the simulation. Besides, users can implement classes which emulate the sensitive region and response of a detector.

2.3 MCHIT

The Monte Carlo model for Heavy-Ion Therapy (MCHIT) was originally developed at FIAS to study physical phenomena relevant to ion-beam cancer therapy [51–56]. MCHIT is a software model which schematically represents a hadrontherapy installation and simulates dose delivery to tissue-like materials during treatment of a localized tumour.

The MCHIT code is a GEANT4-based application inheriting, therefore, all the functionalities of the GEANT4 toolkit. Classes were implemented to model all fundamental aspects of simulations. They establish, for instance, an appropriate selection of physical processes and models or geometrical description of components inserted in a beam line. Additionally, each particular simulation may be customized via input parameters provided by a set of user interface commands. They define for a MCHIT run the beam particle, energy distribution, beam parameters (including spot size and angular divergence), as well as the dimensions and composition of the phantom, beam line elements and detectors used in the simulated experimental set-up.

MCHIT has been used to describe a wide set of experimental data of ion irradiation, including depth and radial energy deposition profiles for protons and carbon nuclei in tissue-like materials, energy spectra and angular distributions of secondary neutrons, yields of secondary nuclear fragments and distribution of positron-emitting nuclei after irradiation. For the purposes of the present thesis, the MCHIT code was further developed as described in our publications [57–62] to simulate microdosimetry measurements with walled and wall-less TEPC devices for neutron, proton and ion beams.

2.3.1 Geometry set-up

The model contains implementations of a number of different physical volumes (geometry with associated material composition) including phantom, collimator, range shifter, ridge filter, ripple filter and TEPCs. Figure 2.1 presents an illustrative set-up where several beam elements are placed in front of a simple phantom irradiated by a pencil-like carbon beam. Lines show the trajectories of the primary and secondary particles while dots show the interaction points.

A commercial walled TEPC (Far West Technology Inc., model LET-1/2) was modelled in MCHIT for the specific purposes of this thesis, see Fig. 2.2. The implemented geometry includes an external aluminium cap, wall of the gas container and an inner spherical gas cavity of 12.7 mm in diameter. The actual TEPC dimensions and the chemical composition of materials were implemented as accurate as possible. It was assumed that the tissue equivalent gas was propane C_3H_8 (55 %) with addition of CO_2 (39.6 %) and N_2 (5.4 %). The spherical gas container with a wall thickness of 1.27 mm was defined in simulations as a shell of tissue-equivalent plastic composed of H (10.1 %), C (77.6 %), N (3.5 %), O (5.2 %), F (1.7 %) and Ca (1.9 %), in accordance with the properties of the NIST material Shonka A-150 plastic. The wall thickness may be customized via an input command in order to model different detector specifications. Even though the aluminum outer shell of the TEPC was also introduced, simulation results were found to be rather insensitive to

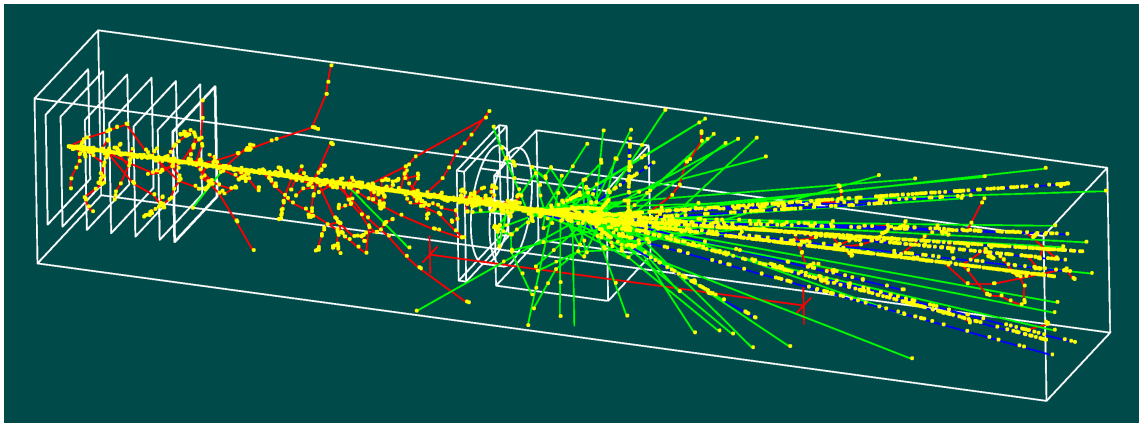

Figure 2.1: Illustrative set-up simulated with MCHIT. Red lines show trajectories of secondary electrons; green lines, neutrons and gammas; and blue lines, charged fragments.

the presence of the Al shell because of its small thickness. The cathode and anode elements located inside the gas sphere were not considered in the simulations. Following Taddei *et al.* [15], it was assumed that quite rare events in which a projectile particle interacted with these components can be neglected. The bending of the simulated tracks due to the voltage applied to the detector was also neglected.

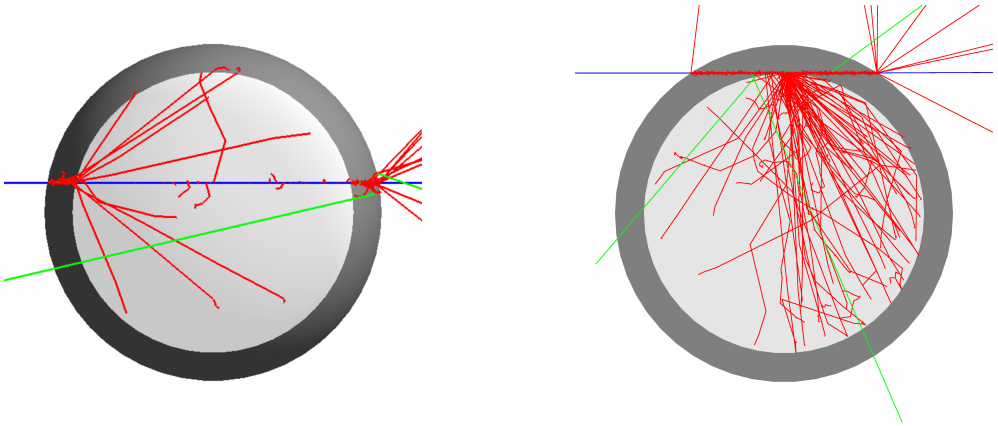

Figure 2.2: Geometry of a walled TEPC implemented in MCHIT with tracks of secondary particles produced in one event for a ^{12}C nucleus (blue track). On the left a central crossing is shown while on the right an ion cross the TEPC wall near the interface region between wall and gas cavity. Red and green tracks represent secondary electrons and gammas, respectively. The external aluminium cap is not shown.

A wall-less TEPC [21, 63], developed at the National Institute of Radiological Science (NIRS), Japan, was also modelled in MCHIT. The implementation, illustrated in Fig. 2.3, includes the anode, cathode, insulators, field tubes and beam window components. The helical geometry of the cathode is simulated by small torus segments displaced along and rotated around the anode wire. A total of 360 torus segments per pitch is used. The material composition of each component was modelled as reported [21, 63].

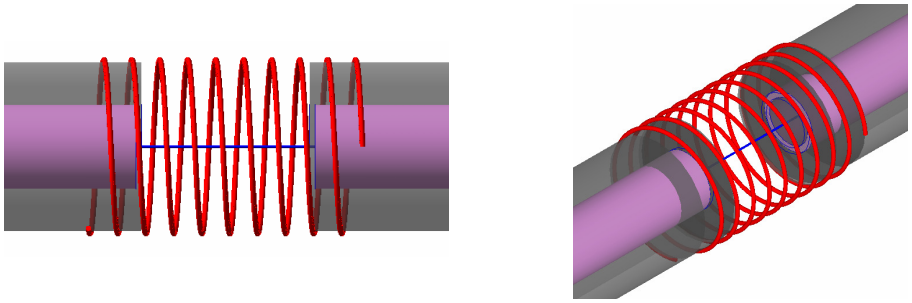

Figure 2.3: Inner geometry of a wall-less TEPC implemented in MCHIT. The anode wire is shown in blue, cathode wire in red, insulators in grey and field tubes in magenta. The beam window is not shown.

2.3.2 Physics models

In MCHIT we make use of the so-called predefined physics lists along with customized ones. The predefined physics lists are provided by the toolkit developers and distributed along with the GEANT4 source code. Separate physics lists for electromagnetic and hadronic physics are kept for convenience. Regarding electromagnetic interaction, the most relevant processes for simulations in this thesis are ionization energy loss and multiple Coulomb scattering. As for hadronic processes, the nuclear fragmentation reaction is required to account for loss of beam particles and yield of secondary fragments in nuclear collisions along the penetration in extended medium.

Electromagnetic processes

The electromagnetic processes are described by means of several predefined and customized physics lists. The predefined physics list called "Standard Electromagnetic Physics Option 3" is recommended by GEANT4 developers for simulations related to ion-beam cancer therapy. As demonstrated [64], the measured positions of the Bragg peak for carbon nuclei of various energies in water are well reproduced with this physics list. However, one should be careful when simulating events inside the gas cavity of a TEPC because the energy threshold for production of secondary electrons may impact the results. Therefore, three different predefined physics list are employed in calculations presented in this thesis. Two of them use the condensed history approach, namely G4EmStd (which uses the "Standard Electromagnetic Physics Option 3") and G4EmPen (which uses the Penelope models for low-energy processes). The third predefined physics list, G4DNA (which uses the GEANT4-DNA models [65]), applies the microscopic approach for description of electromagnetic interactions in liquid water.

The involved physics models simulate the energy loss and straggling of primary and secondary charged particles due to their interaction with atomic electrons. G4EmStd and G4EmPen are based on continuous slowing-down approximation and algorithms of multiple Coulomb scattering of charged particles on atomic nuclei. At each simulation step the ionization energy loss of a charged particle is calculated according to the Bethe-Bloch formula or interpolated between values listed in a table, depending on the particle type and energy [50]. In particular, the Bethe-Bloch formula with the shell, density and high-order corrections is applied (in the class

`G4BetheBlochModel`) to protons with kinetic energy above 2 MeV. Below 2 MeV, stopping power parameterizations [66] are used for protons (`G4BraggModel`). The same methods are applied to alpha particles taking into account the corresponding mass scaling with respect to proton. An interpolation of stopping power tables [67] is implemented (`G4IonParametrisedLossModel`) to calculate electromagnetic energy loss of ions heavier than helium with energies below 1000 MeV/u relevant to our study. The lowest kinetic energy for the production of δ-electrons in the G4EmStd physics list is 990 eV. The emission of δ-electrons with energies below 990 eV is not simulated, but their energies are attributed to the local energy deposition. The G4EmPen predefined physics list extends the capability of electromagnetic models to produce and transport δ-electrons down to 100 eV. Further details on the electromagnetic models included in these physics lists can be found in Ref. [68] and references therein.

The physics list G4DNA explicitly simulates each single electromagnetic interaction (detailed history approach). Therefore, it mainly differs from G4EmStd and G4EmPen in the capability of models to produce and transport low-energy δ-electrons. While energy thresholds for production of δ-electrons are used in G4EmStd and G4EmPen, all δ-electrons are produced and transported by G4DNA. Therefore, this list allows investigation of radiation effects on microscopic scale and it is employed in the following studies to analyse the effect of soft δ-electrons on the simulation of microdosimetry spectra.

Additionally to the aforementioned predefined physics lists, a customized physics list, named G4EmPen+IonGas, is also employed. It basically uses G4EmPen for modelling of electromagnetic processes in condensed medium while applies different models to describe the ionization of gas media by nuclei heavier than proton. This approach is relevant to the case of low-energy ions propagating in very-low density medium where the effective charge approach for the ion has to be replaced by a sampling of the exact charge state.

In order to reduce the CPU time without affecting the accuracy of calculations, different cuts for production of electrons were applied in each physical volume. This technique avoids, for example, transporting low-energy electrons far away from a TEPC when calculating microdosimetry spectra. The cuts used in the simulations are listed in Table 2.1. The cut in range for the tissue-equivalent (TE) gas was defined by the lowest energy of electrons which can be produced by the corresponding models. This limitation in the electromagnetic models amounts for a cut in range of 9 mm for G4EmStd and 3 mm for G4EmPen at 12 kPa. Since 9 mm is of the same order as the diameter of the sensitive volume for the walled TEPC, the comparison of results between the standard and Penelope models helps to understand how this limitation undermines the results. In the plastic shell of the walled TEPC detector the cut in range for electrons was reduced to 10 µm. This helps to simulate accurately grazing interactions of particles with the plastic shell, as secondary particles produced in plastic can propagate further into gas. According to the default settings of GEANT4, all produced particles (including electrons) are transported down to zero kinetic energy.

Table 2.1: Cut in range and energy production threshold for electrons in the water phantom and TEPC components applied in MCHIT simulations with predefined physics lists G4EmStd and G4EmPen.

Material	G4EmStd		G4EmPen	
	Cut in range (mm)	Energy threshold (keV)	Cut in range (mm)	Energy threshold (keV)
Water	0.1	85.	0.1	85.
A-150 TE plastic	0.01	17.6	0.001	0.3
TE gas (12 kPa)	9	0.99	3	0.1

Hadronic processes

A customized physics list was implemented for the modelling of hadronic processes. It is well known that a reliable modelling of inelastic nucleus-nucleus interactions is a fundamental issue to the description of yield of nuclear fragments in ion-beam cancer therapy. Modifications in our hadronic physics list with respect to previous studies [51–56] concern the physics models used to describe the fast stage of nucleus-nucleus collisions.

The overall probability of hadronic interactions for nucleons and nuclei propagating in the media is determined by the total inelastic cross section for nucleon-nucleus and nucleus-nucleus collisions, respectively. Parametrizations by Wellisch and Axen [69] that best fit experimental data are used to describe the total reaction cross sections in nucleon–nucleus collisions. Systematics by Shen *et al.* [70] and Tripathi *et al.* [71, 72] are used for the total nucleus–nucleus cross sections.

The nuclear fragmentation reaction cannot be easily described by a set of formulas or approximations due to a high number of possible decaying channels. Therefore, such nuclear reactions are better described by *ab initio* Monte Carlo models. A nucleus-nucleus collision is modelled in GEANT4 in two separate stages. The first stage describes the initial collision stage when the incoming nucleus overlaps with the target nucleus. The participant nucleons interact strongly in a short time interval while the spectator matter is not so much affected by the collision. It is quite probable that some participant nucleons are knocked-out from the nucleus. Such stage of the reaction can be modelled by intra-nuclear cascade or quantum molecular dynamics models. At the second stage of the reaction de-excitation processes of residual exited nuclei are simulated by statistical models.

In the present study we considered two GEANT4 models to describe the first stage of nucleus-nucleus collisions, namely, the Light Ion Binary Cascade (G4BIC) [73] and the Quantum Molecular Dynamics (G4QMD) [74] models. In earlier studies [56] the G4BIC and G4 abrasion models were employed to describe such reactions. Recent improvements in the G4QMD code [74], as well as the conclusions based on the comparison of G4BIC and G4QMD [75], suggest that the G4QMD model can be also successfully used for modelling nuclear fragmentation of carbon nuclei. Therefore,

in calculations presented here both options to simulate nuclear collisions, G4BIC and G4QMD, are used. G4BIC is applied for proton, helium and lithium projectiles while G4QMD is used for heavier nuclei.

Excited nuclear fragments are frequently produced in addition to free nucleons as a result of the simulation of a nucleus-nucleus collision event by the G4BIC and G4QMD models. Therefore, the class `G4ExcitationHandler` of GEANT4 is used to simulate subsequent decays of excited nuclear fragments by applying various de-excitation models depending on the mass and excitation energy of these fragments. The Fermi break-up model (`G4FermiBreakUp`) is applied to excited nuclei lighter than fluorine. It is designed to describe explosive disintegration of excited light nuclei [76] and it is highly relevant to collisions of light nuclei with nuclei of tissue-like materials. As demonstrated [55], G4BIC linked with `G4FermiBreakUp` better describes the production of lithium and beryllium nuclei, as well as secondary neutrons by ^{12}C nuclei in water and PMMA compared to the option of G4BIC linked with the nuclear evaporation model. As demonstrated by Böhlen *et al.* [75], the combination of G4QMD and `G4FermiBreakUp` also describes data well. Therefore, we use `G4FermiBreakUp` to de-excite light fragments also in the present thesis. For heavier excited nuclei either the evaporation model [77] can be used at low excitations (below 3 MeV/u), or the statistical multifragmentation model (SMM) [76] at higher excitation energies. Generally, the inclusion of fragmentation reactions helps to describe the yields of intermediate-mass fragments.

2.3.3 Scoring physical quantities

Physical quantities are scored in MCHIT by different procedures. Spatial energy deposition in the phantom, for example, is retrieved after each step along the transport of particles using the class `G4UserSteppingAction`. Other quantities such as yield of secondary fragments, energy and angular spectra or fluences are also scored in this way. The spatial distribution of positron-emitting nuclei, however, is scored using the class `G4UserTrackingAction` by retrieving the information on the final position of the nuclei, *i.e.*, the end of the particle track.

On the other hand, the primitive scorer classes of GEANT4 are applied to accumulate simulation results for physical quantities inside the TEPC sensitive volume characterizing, in this way, the detector response in each event. The energy ϵ deposited to the TEPC is accumulated by means of the `G4PSEnergyDeposit` scorer. This scorer stores a sum of energy deposits by particles to the sensitive volume in each event. The number N of tracks that pass through the detector, but do not start or stop inside it, is accumulated by employing `G4PSPassageCellCurrent`. In particular, this means that numerous low-energy δ-electrons which are produced by energetic nuclei but stop inside the TE gas are not counted by this scorer. Finally, `G4PSPassageTrackLength` is used to accumulate the total track length l inside the TEPC in single and multi-particle events. With this scorer the track length is defined as the sum of step lengths of the particles inside the volume, and again only tracks which traverse the volume are taken into account. This means that newly-generated or stopped tracks inside the TE gas are excluded from the calculation of l. The employed `G4PSPassageTrackLength` scorer is thus insensitive to those secondary electrons which were produced by a fast particle inside the sensitive vol-

ume, but stopped inside it. The total track length is scored in order to evaluate the mean track length through the detector for comparison with the mean chord length ($\bar{l} = 2d/3$ for a spherical cavity) in the standard conditions of microdosimetry measurements.

Chapter 3

Microdosimetry for HZE Particles from Cosmic Rays

For decades space exploration has fostered developments in many fields of science. The first manned space flight dates back to 1961 when the Russian astronaut Yuri Gagarin made one orbit around the Earth. Just 8 years later, in 1969, the American Neil Armstrong was the first person to walk on the Moon. In the present time, humans are continuously orbiting the Earth in the International Space Station (ISS). Future plans of space exploration include the construction of a station on the Moon and travelling to Mars [78, 79]. However, space is not a safe environment to humans as they need to cope with several health problems due to low gravity, isolation and radiation [80]. One of the most important issues related to such exploration projects is the health hazard to astronauts caused by exposure to radiation in space. Several research programs are in progress to investigate the physical and biological effects of space radiation and develop mitigating strategies to reduce risks to crew members [81, 82].

The radiation environment in deep space – far from the magnetic field of the Earth – is usually classified in two components: the solar particle events (SPE) and the galactic cosmic rays (GCR). Particles present in these radiation components cause highly ionizing radiation. While humans are well shielded on Earth by the atmosphere and magnetosphere, an astronaut will lack such an effective protection in future space travels. Therefore, radiation effects due to SPE and GCR must be understood.

SPE are highly energetic ejections of electrons, protons, alpha particles and heavier nuclei emitted by the Sun. These particles can cause severe damages to unshielded crew members and components of a spacecraft [80]. In fact, one of the largest detected SPE occurred in 1972 between the Apollo missions 16 and 17. The radiation level was high enough to kill crew members if they were exposed for more than 10 hours outside the magnetosphere [83]. Strategies to mitigate the effects due to SPE include using proper shielding and scheduling missions during phases of low solar activity [80].

GCR consist of nuclei ranging from proton up to uranium originated, for instance, from supernova explosions. The majority are protons with only 1 % of nuclei heavier than alpha particles. The maximum of the spectrum for specific GCR nuclei is between 100–1000 MeV/u. The fluxes of 10 GeV/u nuclei are two orders of magnitude

lower [80]. Even though the fluxes of heavy nuclei (*e.g.* Fe) are much lower than the flux of protons or helium nuclei, the energy deposition of a nucleus scales with the square of the nuclear charge. As a result, the physical dose from iron nuclei is comparable to one from GCR protons. As soon as the biological effectiveness of each particle is considered, the equivalent dose delivered by iron nuclei, for example, becomes even higher than by protons [84].

Shielding of crew members is crucial for their protection from protons of SPE and nuclei of GCR. However, shielding from GCR is much less effective because of their energy spectra extending to high energies. For this reason, GCR make up more than 80 % of the effective dose to the crew on ISS [80]. High-charge (Z) and energy (E) nuclei from GCR, known as HZE particles, cannot be stopped by any shield available in space missions. The high biological effectiveness of HZE particles results in a considerable contribution to the received biological dose. Besides, the LET of a HZE particle increases when traversing the spacecraft materials and a complex radiation field is created due to nuclear fragmentation reactions. Since HZE particles cannot be effectively shielded during the space flight, following chronic radiation effects are expected to be significant [85]. Therefore, the radiation effects due to HZE particles must be thoroughly investigated.

Dose monitors for space radiation fields shall be able to cover a broad LET spectrum. Experiments which investigate radiation effects in space have employed several types of detectors on the board of the Space Shuttle [86–88] and at the ISS [89]. Due to their compact size, TEPCs (see Section 1.2) are frequently employed for microdosimetry measurements in space. TEPCs are continuously flying on-board the ISS for on-line monitoring of the radiation level inside the spacecraft [83]. Such kind of detectors has also been used in ground-based experiments with HZE particles from accelerators to model irradiation in space. Several experiments performed with the Heavy Ion Medical Accelerator in Chiba (HIMAC) at the National Institute of Radiological Sciences (NIRS), Japan and the Alternating Gradient Synchrotron (AGS) at Brookhaven National Laboratory (BNL), United States used TEPC detectors for microdosimetry measurements of HZE particles in the energy range of 80–1000 MeV/u [13–15, 22]. Future studies for space exploration shall continue to use TEPCs following the recommendations of the National Council on Radiation Protection and Measurements (NCRP) [90]. The Facility for Antiproton and Ion Research (FAIR), Germany which is currently under construction, will allow microdosimetry measurements and radiobiological experiments with HZE particles at higher energies [91]. This will help to reduce the uncertainties in estimating the health risks to astronauts due to exposure to GCR in future long space flights.

In the following studies we apply available microdosimetry data for HZE particles to validate physical models of Geant4 using MCHIT. A particular set of the experiments employed a special set-up to identify and discard any event in the TEPC when the primary ion underwent nuclear fragmentation. We used the experimental data to evaluate the capabilities of electromagnetic models to reproduce the response function of the TEPC. Our results of this study, presented in Section 3.1, were published in Ref. [59]. In addition, it is also necessary to assess Geant4 models for hadronic processes since nuclear fragmentation reactions inevitably happen in the shield of the spacecraft resulting in complex radiation fields consisting of a mixture of primary nuclei and secondary fragments. We selected microdosimetry

spectra sensitive to nuclear reactions to investigate the impact of ion fragmentations. Section 3.2 presents results of this study published in Ref. [61].

3.1 Validation of electromagnetic models

Reliable simulations of the production and transport of δ-electrons in low-density medium are important for modelling microdosimetry measurements. Such electrons may travel distances as large as the sensitive volume of the TEPCs. Therefore, it is important to assess the validity of the different electromagnetic models available in GEANT4 and the effect of the thresholds applied in the production of secondary electrons to the description of the response function of the detector.

Experimental data collected at HIMAC/NIRS and AGS/BNL [13–15] are used to validate MCHIT for microdosimetry calculations with beams of HZE particles. In these experiments a walled TEPC detector was irradiated by ions with energies from 80 to 1000 MeV/u as presented in Table 3.1. Detectors placed upstream and downstream of the TEPC were used to measure the impact parameter of the incoming ion and reject projectile fragmentation events. Due to this event selection, the response functions of the TEPC measured in these experiments are sensitive only to electromagnetic processes induced by beam nuclei and secondary electrons in the TEPC, as the contribution of nuclear fragments is excluded.

Table 3.1: Experimental parameters of microdosimetry measurements of HZE particles at AGS/BNL and HIMAC/NIRS used in validations of GEANT4 electromagnetic models with MCHIT. Measurements were performed with a spherical walled TEPC.

Ion	Energy (MeV/u)	Pressure (kPa)	d* (μm)	Reference
^{4}He	225	13.2	3	Taddei *et al.* [15]
^{12}C	215	13.2	3	Taddei *et al.* [15]
^{12}C	389	4.4	1	Taddei *et al.* [15]
^{14}N	80	4.4	1	Guetersloh *et al.* [14]
^{16}O	385	4.4	1	Taddei *et al.* [15]
^{20}Ne	210	4.4	1	Guetersloh *et al.* [14]
^{28}Si	375	4.4	1	Taddei *et al.* [15]
^{28}Si	780	4.4	1	Guetersloh *et al.* [14]
^{56}Fe	200	4.4	1	Gersey *et al.* [13]
^{56}Fe	355	4.4	1	Taddei *et al.* [15]
^{56}Fe	360	4.4	1	Gersey *et al.* [13]
^{56}Fe	540	4.4	1	Gersey *et al.* [13]
^{56}Fe	700	4.4	1	Gersey *et al.* [13]
^{56}Fe	790	4.4	1	Gersey *et al.* [13]
^{56}Fe	1000	4.4	1	Gersey *et al.* [13]

* The diameter of the tissue-equivalent volume emulated by the TEPC.

Calculations presented below were obtained using MCHIT built with GEANT4

of version 9.5 with patch 1. Electromagnetic processes are simulated by means of the physics lists G4EmStd and G4EmPen (see Section 2.3.2). The Penelope models contained in G4EmPen were used with a lower energy threshold of 250 eV for production of δ-electrons compared to the standard electromagnetic models (with a threshold of 990 eV) in G4EmStd. Therefore, once differences in results obtained with these two physics lists are found, they indicate the importance of producing and transporting low-energy electrons with kinetic energies from 250 to 990 eV.

The geometry of the walled TEPC used in experiments is represented in simulations by a spherical cavity of 12.7 mm in diameter surrounded by a 2.54 mm thick plastic shell (see Section 2.3.1 for a discussion of TEPC modelling). The gas pressure is set to the particular value used in each experiment, presented in Table 3.1, emulating tissue objects with diameter of 1 and 3 µm. A total of 2×10^7 primary ions are simulated for each beam energy. In each event the energy deposition inside the gas cavity and the impact parameter b are scored to calculate the response function of the detector.

The response function of the TEPC irradiated by an uniform fluence of 210 MeV/u ^{20}Ne ions is presented in Fig. 3.1. Neon ions impart on average $\bar{\varepsilon} = 28$ keV per event to a sphere of 1 µm of tissue. The mean energy deposition is reproduced by MCHIT within 1.2 %. The function of energy imparted to the TEPC for ions traversing the detector with small impact parameters $b < 0.8$ mm is presented in Fig. 3.2. MCHIT successfully describes the experimental distribution with both sets of electromagnetic models. One can see that the selection of events with small impact parameters increases the mean energy imparted to the sensitive volume. This results from the larger amount of energy directly imparted by the ions along the longer trajectories through the gas cavity at central incidence compared to the uniform irradiation.

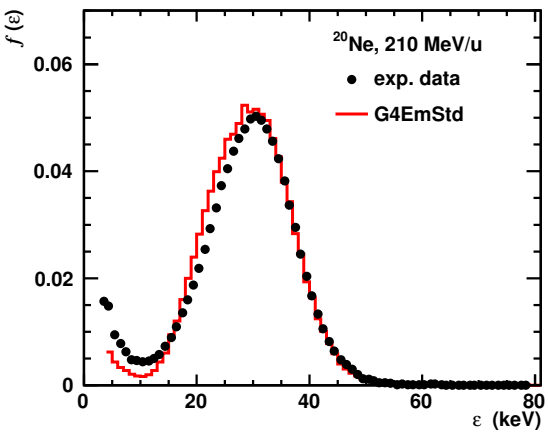

Figure 3.1: Energy imparted to the TEPC by 210 MeV/u ^{20}Ne ions for an uniform fluence. Experimental data from Ref. [13].

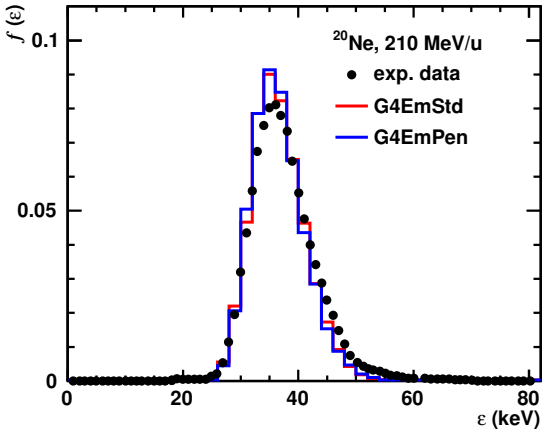

Figure 3.2: Energy imparted to the TEPC by 210 MeV/u ^{20}Ne ions at impact parameters $b < 0.8$ mm. Experimental data from Ref. [14].

Figure 3.3 demonstrates the mean energy deposition per event and the product of the LET and the chord length as a function of the impact parameter. MCHIT describes well the decrease of $\bar{\varepsilon}$ with increase of b for impact parameters smaller than the cavity radius (*i.e.*, $b < 6.35$ mm). At the interface between gas and plastic there

is a bump in the mean energy deposition in the experimental data and simulation results. This phenomenon, first experimentally observed by Rademacher *et al.* [92] and theoretically reproduced by Nikjoo *et al.* [16], is due to the enhancement of the influx of δ-electrons produced in the wall and propagated into the gas cavity when a primary ion grazes the gas/wall interface. Such δ-electrons elevate the energy deposition in grazing collisions. Both physics lists G4EmStd and G4EmPen describe this phenomenon well despite of different energy thresholds for production of δ-electrons. One can conclude that the production of δ-electrons with kinetic energy between 250–990 eV do not affect simulation results. The product of the LET and the chord length at a given impact parameter deviates from the experimental results and MCHIT simulations for $\bar{\varepsilon}$. This discrepancy results from the above-described enhancement of energy deposition in grazing collisions and also from violation of the charged-particle equilibrium [13] for this detector. Calculations of the mean energy imparted to the TEPC by 360 MeV/u ^{56}Fe ions as a function of impact parameter were performed with G4EmStd and G4EmPen. They provide again equivalent results with the lowest possible energy thresholds for production of δ-electrons (results not shown). Figure 3.4 presents simulation results only with G4EmStd but using various energy thresholds. We can see that the calculations with the energy threshold of 100 keV cannot reproduce the enhancement of energy deposition in grazing collisions, while with the energy threshold of 10 keV this phenomenon is reproduced. The mean energy imparted to the TEPC in events with impact parameter smaller than 3 mm is overestimated with both G4EmStd and G4EmPen physics lists even with the lowest possible energy thresholds for production of δ-electrons. The reason for this overestimation is not known and it needs further investigation which is out of the scope of the present study.

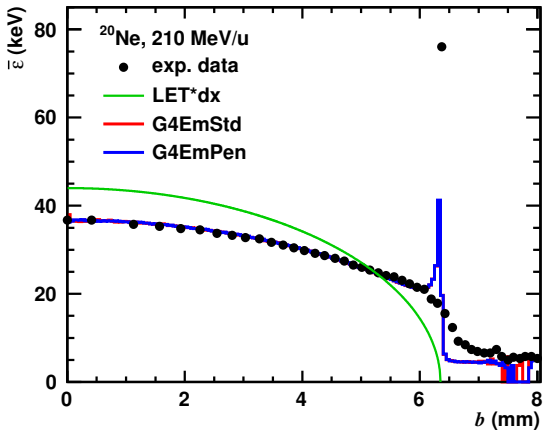

Figure 3.3: Mean energy imparted to the TEPC by 210 MeV/u ^{20}Ne ions as a function of impact parameter. Experimental data from Ref. [14].

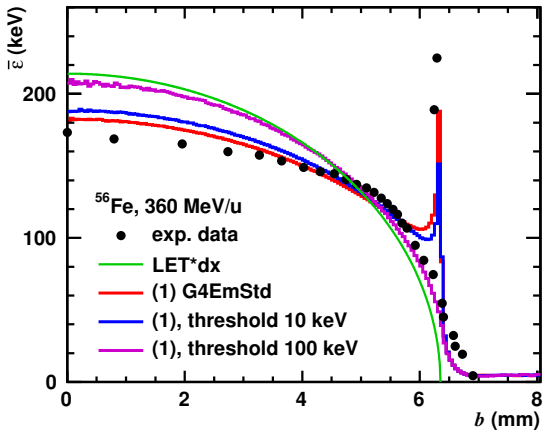

Figure 3.4: Mean energy imparted to the TEPC by 360 MeV/u ^{56}Fe ions as a function of impact parameter. Experimental data from Ref. [13].

Measured and calculated frequency distributions of energy deposition events were used to evaluate microdosimetry parameters. MCHIT results for the frequency-mean $\bar{y}_F$ and dose-mean $\bar{y}_D$ lineal energy for several ions obtained with the Penelope models are listed in Table 3.2. Experimental values [14, 15] and theoretical

results obtained with the Monte Carlo code FLUKA [93] are shown for comparison. Calculations with GEANT4 and FLUKA agree well with the experimental values. Unrestricted LET is also presented in Table 3.2 for comparison with micro-

Table 3.2: Results for microdosimetry parameters $\bar{y}_F$ and $\bar{y}_D$ simulated with MCHIT. Experimental data from Refs. [14, 15]. Simulation results with FLUKA from Ref. [93].

Ion	Energy (MeV/u)	LET (keV/µm)	$\bar{y}_F$ (keV/µm)			$\bar{y}_D$ (keV/µm)		
			exp.	FLUKA	MCHIT	exp.	FLUKA	MCHIT
^{4}He	225	1.68	1.56	1.67	1.61	2.58	2.52	2.41
^{12}C	215	15.6	13.4	14.41	14.0	16.1	17.11	16.4
^{12}C	389	11.2	9.93	10.2	9.95	12.4	12.97	12.2
^{14}N	80	43	44	43.8	42.3	47	48.3	46.0
^{16}O	385	19.9	17.9	17.54	17.2	20.8	21.68	20.8
^{20}Ne	210	44	42	43.5	41.5	48	48.1	45.4
^{28}Si	375	61.9	50.4	49.7	49.0	59.8	65	62.4
^{28}Si	780	46	39	41.6	41.3	47	47.7	46.4
^{56}Fe	355	219	184	186.4	183	224	228.3	220

dosimetry parameters. Although the TEPC does not measure LET directly, $\bar{y}_D$ for heavier ions approximates LET, as already pointed out by Gersey *et al.* [13]. This demonstrates the usefulness of microdosimetry data for estimating biological effects of radiation as several radiobiological models describe such effects as a function of LET. The correspondence between LET and $\bar{y}_D$ for heavier nuclei is confirmed by MCHIT calculations. Figure 3.5 presents results for iron ions with energy from 200 to 1000 MeV/u. A good agreement between simulations and experimental data is found. LET and $\bar{y}_D$ agree well especially at high energy. Therefore, $\bar{y}_D$ can be used as an approximation of LET for iron ions in this energy regime.

3.2 Validation of hadronic models

High-energy ions as those found on the GCR are subject to nuclear fragmentation reactions when crossing matter. Fragments of HZE particles produced in the shield may contribute to the events recorded by a TEPC inside the spacecraft. Therefore, measured microdosimetry spectra include energy imparted by primary GCR nuclei and secondary fragments. Such a change in radiation quality is also expected inside the body of astronauts (self-shielding). In the course of extra-vehicular activities, for instance, the skin is irradiated mostly by primary GCR while the inner organs are exposed to a complex field made of primary and secondary charged particles at various kinetic energies. The understanding of the role played by such secondary fragments via the measured microdosimetry spectra may help in the investigation of radiation effects caused by this complex radiation field.

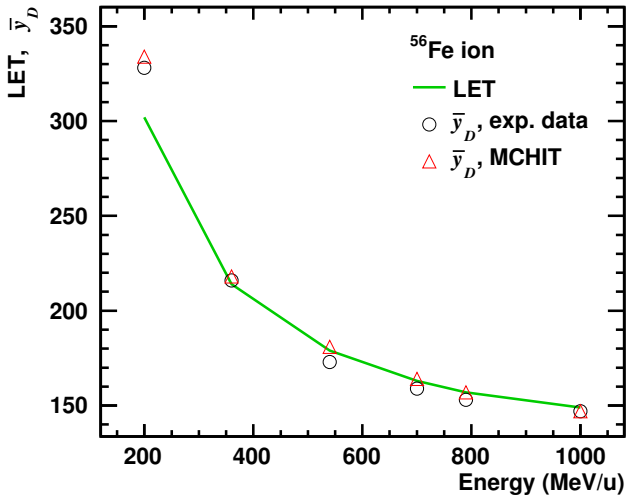

Figure 3.5: Comparison of LET with $\bar{y}_D$ for ^{56}Fe ions of several beam energies. Experimental data from Ref. [13].

It is helpful to examine the yield of secondary fragments in nuclear reactions before calculating microdosimetry spectra for a TEPC irradiated by a complex radiation field. Measurements [19, 94] for a 400 MeV/u ^{12}C ion beam irradiating a water phantom were performed at Gesellschaft für Schwerionenforschung (GSI), Germany. Figure 3.6 shows experimental data for attenuation of beam particles and yields of secondary nuclei as a function of depth in water. This can be considered as a self-shielding of a human body. The fast stage of nuclear collisions for carbon ions is simulated in MCHIT with the G4QMD model. MCHIT reproduces well the attenuation of carbon ions and the yield of most heavy fragments, namely lithium, beryllium and boron. The yield of hydrogen fragments is slightly overestimated by MCHIT while calculations underestimate the yield of helium fragments. This may be related to neglecting the cluster structure of carbon nuclei, which leads to the underestimation of decays of excited nuclei into channels containing alphas. It becomes clear that a TEPC placed on the beam axis is irradiated by smaller fractions of carbon nuclei when the device is moved to deeper positions. Besides, after the maximum range of carbon ions, the partial contribution of each secondary fragment to the fluence of particles crossing the TEPC and the lineal energy events also changes as a function of position due to the different kinetic energies, angular distribution and stopping powers of these particles. For example, at 270 mm depth the number of boron nuclei is higher than the number of lithium and beryllium nuclei but this changes with increasing depth.

Figure 3.7 shows the angular distributions of hydrogen, helium, lithium and boron fragments measured by detectors placed just before the Bragg peak at 258 mm. The magnitude and trend of the yields as a function of angle is generally well reproduced by MCHIT. The angular distribution is broader for lighter nuclei. Data for hydrogen and lithium nuclei are particularly well reproduced while helium nuclei are underestimated at all angles. Simulations predict a broader angular distribution for boron nuclei compared to experimental data. The energy distribution for helium fragments at the same depth and angle of 4 degrees is presented in Fig. 3.8. MCHIT reproduces well the shape of the experimental distribution and the average kinetic

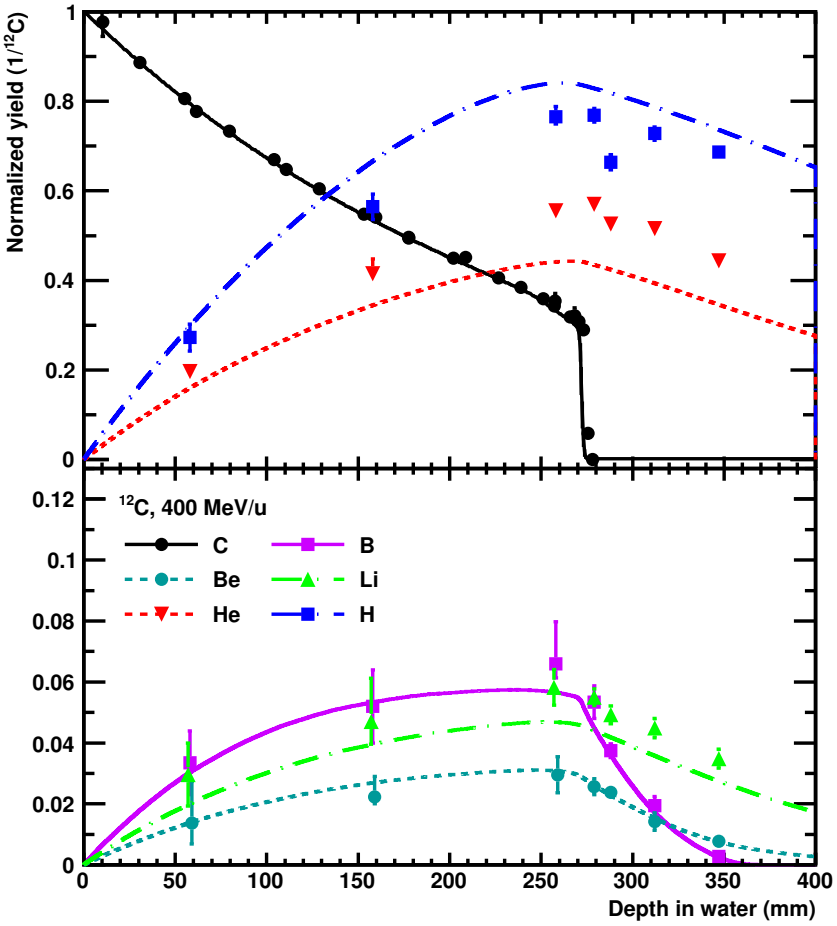

Figure 3.6: Yields of secondary nuclei for carbon fragmentation reactions in water. Lines show calculations with MCHIT while symbols indicate experimental data from Refs. [19, 94].

energy but slightly underestimate the He yields. Figures 3.7 and 3.8 demonstrate how complex is the radiation field at different positions respective to the initial trajectory of the primary ion. Besides, the lineal energy spectra for each particular fragment is expected to be as broad as the kinetic energy distribution. This results in different radiobiological properties of secondary fragments.

Our previous investigation of the response of TEPC to HZE particles [59] is extended to detailed simulations of microdosimetry spectra in the presence of nuclear fragmentation reactions. In the present section, microdosimetry spectra resulting from irradiation of extended media with protons, helium, lithium, carbon and silicon nuclei in the energy range of 150–490 MeV/u are compared to experimental data. The contributions of secondary fragments created in fragmentation of beam nuclei are calculated too. The measurements performed at NIRS for proton, helium and silicon ions [22] as well as at GSI for lithium and carbon ions [23] were selected for benchmarking of MCHIT. The corresponding experimental parameters are presented in Table 3.3.

The measurements at NIRS were performed with a wall-less TEPC emulating a cylindrical tissue volume of 0.72 µm in diameter. The TEPC was placed behind

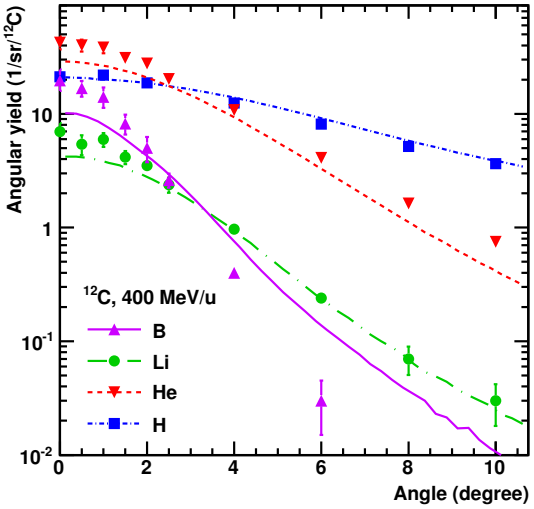

Figure 3.7: Angular yield of secondary nuclei for carbon fragmentation reactions in water at 258 mm (just before the Bragg peak). Lines show calculations with MCHIT while symbols indicate experimental data [19, 94].

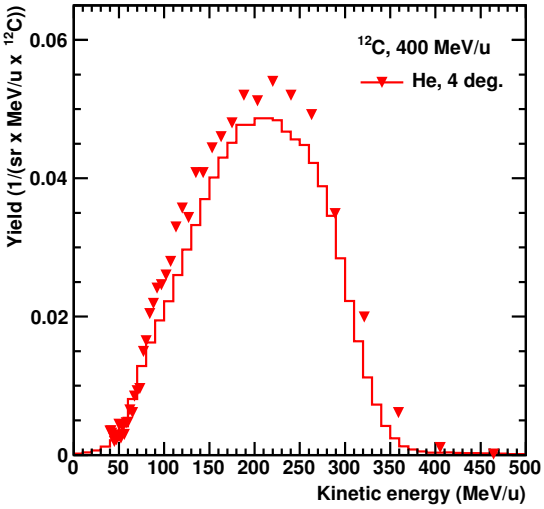

Figure 3.8: Energy distribution of helium fragments emitted at 4° in carbon fragmentation reactions in water at 258 mm (just before the Bragg peak). Lines show calculations with MCHIT while symbols indicate experimental data [19, 94].

range shifters of varying thickness made of PMMA. At GSI, a walled TEPC was applied emulating a spherical tissue volume of 2.7 µm in diameter. The walled TEPC was placed at several locations inside a water phantom.

In the calculations that follow, MCHIT is based on GEANT4 version 9.5 with patch 02. The electromagnetic processes are simulated by means of Penelope models including models for ionization process of gas media by ions (G4EmPen+IonGas). The fast stage of nucleus-nucleus collision is modeled by G4BIC for helium and lithium projectiles and by G4QMD for carbon and silicon projectiles. Further details on physics lists are presented in Section 2.3.2.

Microdosimetry spectra were simulated for various ions showing a general agreement with experimental data as presented in Fig. 3.9. Panel (a) shows the spectrum for homogeneous proton irradiation of a wall-less TEPC behind a range shifter of 163 mm-we (water-equivalent). The spectrum is peaked at $y = 1$ keV/µm extending up to 20 keV/µm. In panel (b) the spectrum for helium beam with same wall-less TEPC but behind a range shifter of 157.1 mm-we is presented. In this case the spectrum is peaked at ~ 15 keV/µm due to primary ions while secondary protons give the main contribution for events below 2 keV/µm. Lineal energy events due to helium projectiles extend up to 200 keV/µm. Panels (c) and (d) show the spectra measured with a walled TEPC irradiated by a pencil-like lithium beam inside a water phantom at the plateau and Bragg peak of the depth-dose distribution, respectively. The disagreement between experimental data and simulation results in panel (c) is likely related to pile-up of events during data acquisition in the experimental set-up (see the discussion in Section 5.2.4). The change of radiation quality with depth in water is clearly seen. Not only the contribution of lithium changes due to the reduc-

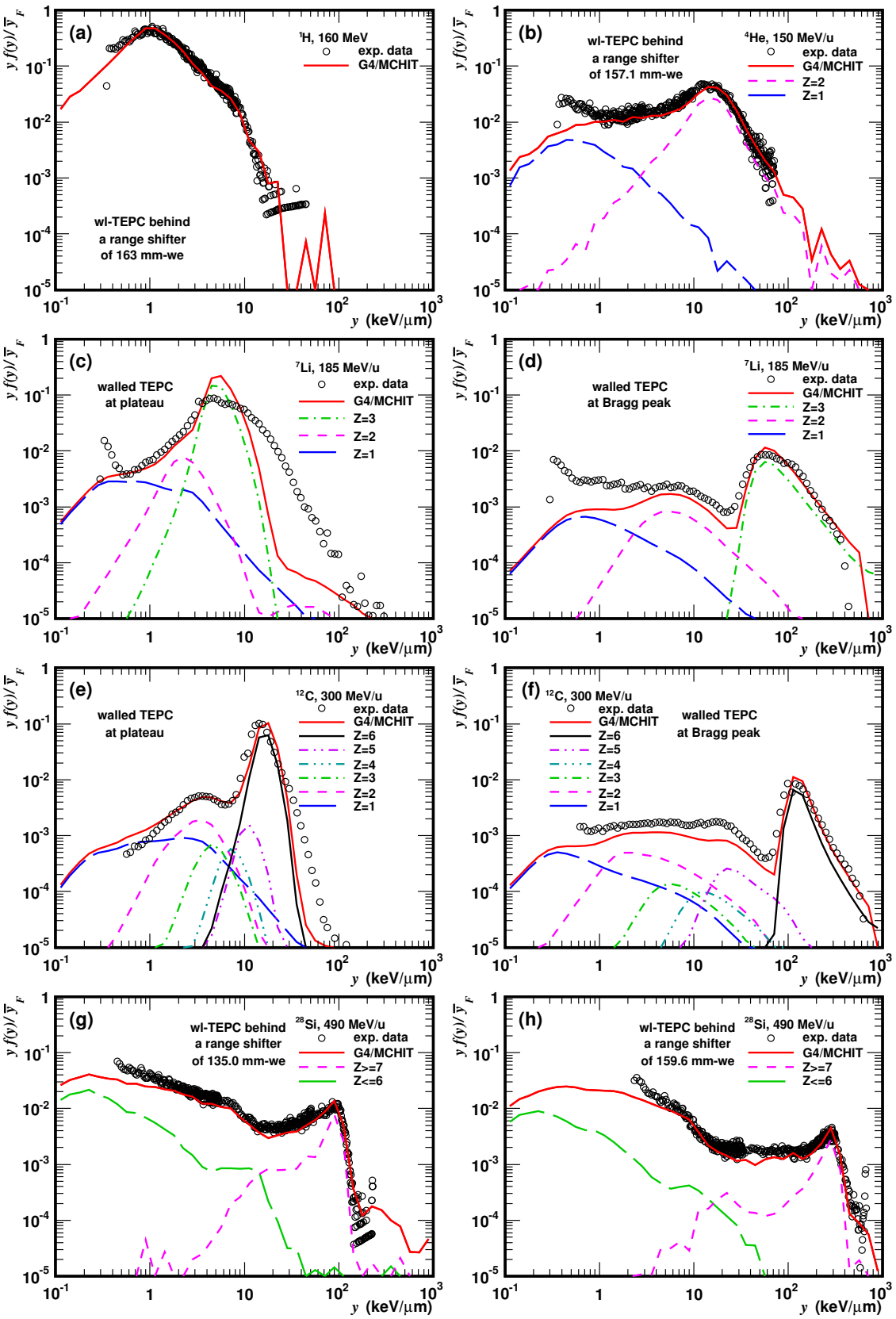

Figure 3.9: Microdosimetry spectra for (a) ^{1}H, (b) ^{4}He, (c-d) ^{7}Li, (e-f) ^{12}C and (g-h) ^{28}Si at different water-equivalent depths. Experimental data from Refs. [22, 23] are shown.

Table 3.3: Experimental parameters of microdosimetry measurements of HZE particles at SIS-18/GSI [23] and HIMAC/NIRS [22] used in validations of GEANT4 electromagnetic and hadronic models with MCHIT. Measurements were performed with a walled TEPC and a wall-less TEPC at GSI and NIRS, respectively.

Ion	Energy (MeV/u)	Pressure (kPa)	d* (μm)	Reference
^{1}H	160	13.3	0.72	Tsuda *et al.* [22]
^{4}He	150	13.3	0.72	Tsuda *et al.* [22]
^{7}Li	185	12.0	2.7	Martino *et al.* [23]
^{12}C	300	12.0	2.7	Martino *et al.* [23]
^{28}Si	490	13.3	0.72	Tsuda *et al.* [22]

* The diameter of the tissue-equivalent volume emulated by the TEPC.

tion of kinetic energy, but also the role played by secondary particles evolves. At the plateau position, the contribution of projectile-like helium fragments is seen between 0.2–18 keV/μm, and of target-like fragments between 18–100 keV/μm. This is explained by the fact that projectile-like fragments have velocities similar to the primary ion but smaller stopping power due to their smaller nuclear charges. The contribution of primary ions is broad and peaked at $\sim$5 keV/μm. When the TEPC is moved deeper into the phantom, the peak is shifted to $\sim$60 keV/μm and a shoulder in the spectrum at lower y values is clearly visible due to the contribution of helium and hydrogen fragments. Panels (e) and (f) show similar measurements with a pencil-like carbon beam at the plateau and Bragg peak positions, respectively. Also in this case a clear change of radiation quality is observed with depth where a variety of secondary particles along with the primary carbon ions contribute to the spectra. The maxima are observed at $\sim$16 keV/μm and $\sim$120 keV/μm at the plateau and Bragg peak, respectively. The underestimation of the satellite peak observed in the spectrum at the peak position indicates that the GEANT4 models for nuclear fragmentation may need further improvements as also indicated in Figs. 3.6 to 3.8. The panels (g) and (h) present the spectra measured with the wall-less TEPC behind two range shifters of different thickness irradiated by silicon ions. As seen, the shape of the calculated spectra is defined by light ($Z \leq 6$) and heavy ($Z \geq 7$) nuclei, which contribute to low ($y < 40$ keV/μm) and high ($y > 4$ keV/μm) linear energy events, respectively. Behind a range shifter of 135 mm-we the spectrum is peaked at 100 keV/μm, while the peak is shifted to 300 keV/μm when the thickness of the range shifter is increased to 159.6 mm-we. In general, the agreement of MCHIT results with experimental data is rather good. Noticeable discrepancies are found only in the region of small $y < 1$ keV/μm, see *e.g.* panels (b) and (d).

Conclusions

Our studies of microdosimetry spectra of protons, helium ions and HZE particles led us to the following conclusions:

- GEANT4/MCHIT describes well the TEPC response function as well as the microdosimetry parameters for a broad selection of ions and beam energies relevant to space research.

- Both electromagnetic physics lists G4EmStd and G4EmPen describe reasonably well the experimental microdosimetric data. MCHIT is able to describe the wall effect due to the enhanced production of δ-electrons which enter the gas cavity when a primary ion grazes the wall/gas interface.

- The measurements of microdosimetry spectra behind extended medium like a shield open another possibility to validate Monte Carlo transport codes. Microdosimetry spectra for hydrogen, helium, lithium, carbon and silicon ions in the energy range relevant to GCR can be successfully calculated with GEANT4/MCHIT.

- Nuclear fragmentation reactions which happen in a shielding of a spacecraft lead to a composite radiation field inside the spacecraft. This affects and the RBE of the radiation field to which astronauts are exposed (as discussed further in Section 5.3.2). Therefore, not only the physical dose, but also the resulting biological effects are affected by shielding.

Chapter 4

Microdosimetry for Ion-Beam Cancer Therapy

At present time the ion-beam cancer therapy is one of the most advanced methods in radiation therapy [1, 2, 7]. An elevated biological effectiveness of accelerated nuclei provides advantages in treatment of radioresistant solid tumours, but also requires a thorough treatment planning to reduce undesirable impact of radiation on healthy tissues. This should include, in particular, a realistic description of the production of secondary nuclear fragments. Such secondary particles deliver dose to the tissues located farther than the Bragg peak for primary nuclei and also around the primary beams.

Recently there were several experimental [19] and theoretical [47, 56, 75] studies which confirmed the need to consider nuclear fragmentation reactions in heavy-ion therapy. In particular, as shown by measurements with a 400 MeV/u ^{12}C beam, about 70 % of beam nuclei undergo fragmentation reactions [19]. Apart from the effect of primary beam attenuation, this means that the dose around the beam is delivered by light charged fragments, (*e.g.* protons and helium nuclei) and also by neutrons. In particular, neutrons may propagate large distances from their production points before they initiate secondary nuclear reactions.

As demonstrated by studies with various transport codes, such as SHIELD-HIT [47], FLUKA and GEANT4 [56, 75], the measured attenuation of the primary carbon beam and build-up of beam fragments are generally well reproduced by the theory. However, as follows from the same studies, there are problems with quantitative description of the yields, angular distributions and energy spectra for several kinds of fragments produced in fragmentation reactions in water. It is unlikely that such deficiency will be eliminated soon, as this will require combining dynamical and statistical models of nuclear reactions with sophisticated nuclear structure models into a unified, but still computationally effective tool.

Nuclear fragmentation models calculate the yields of secondary fragments as functions of their charges and velocities. However, the impact of specific particle species on living cells is rather correlated with their linear energy transfer (LET) values. The LETs of particles with different charges Z, but similar velocities are approximately proportional to their Z^2. At the same time ions of different velocities and charges may have similar LET [14]. Therefore, the reliability of nuclear fragmentation models, in particular used in GEANT4 calculations [56, 75], should be also

evaluated with respect to calculations of LET or related quantities.

The biological action of radiation is commonly characterized by microdosimetric quantities [8, 11, 12] such as lineal energy y, its probability density $f(y)$ and dose probability density $d(y)$. Frequency-mean, $\bar{y}_F$, and dose-mean, $\bar{y}_D$, lineal energies are defined as the first moments of the corresponding distributions, see Section 1.2.1 for their definitions. These distributions are routinely measured by means of tissue-equivalent proportional counters (TEPC) [9, 10].

In a complex radiation field different particles can eventually contribute with similar y. Therefore, the resulting y-distribution is built as the sum of contributions from primary and all secondary particles passing the TEPC. Measurements and calculations of microdosimetric quantities related to ion-beam cancer therapy were reported by several authors. In particular, microdosimetric quantities were used to characterize the biological dose from therapeutic ^{12}C beams [3, 4]. Measurements and simulations with the PHITS code were done for a wall-less TEPC irradiated by 290 MeV/u ^{12}C ions [21]. The energy deposition inside and around a 300 MeV/u ^{12}C beam measured with a walled TEPC in water [23] were calculated with SHIELD-HIT and FLUKA codes [95, 96], but without implementing the exact geometry of the TEPC detector and, respectively, without calculating y-distributions. The FLUKA code was also used to simulate responses of TEPC to various ions [93], including y-distributions for the detector located on the beam axis inside a water phantom irradiated by ^{12}C beam [97].

In previous studies [51–56] our MCHIT model was used to validate the GEANT4 toolkit [41, 42] for use in ion-beam cancer therapy simulations. Depth-dose distributions [52] and production of positron-emitting nuclei [53, 54] were calculated. Special effort was made to evaluate the quality of nuclear fragmentation models [55, 56] by comparing theoretical predictions with experimental data on fragment yields [19].

The main purpose of the present investigation, published in Ref. [58], consists in accurate modelling of in-field and out-of-field microdosimetry spectra, their averages and contributions from secondary neutrons for pencil-like ^{12}C beams, which are typical for facilities with scanned therapeutic beams. In this case a TEPC placed in a water phantom is impacted by a complex radiation field. It is either irradiated by a mixture of beam nuclei and secondary fragments or exposed exclusively to such fragments far from beam axis or beyond the Bragg peak.

In order to achieve the central goal of our study the following specific issues are investigated:

- the sensitivity of calculational results to the choice of the GEANT4 models and their parameters for nuclear reactions and production and transport of secondary electrons, *e.g.* the production thresholds;

- the accuracy of the MCHIT model in describing microdosimetry spectra of quasi-monoenergetic neutrons as a prerequisite for estimating the contribution of secondary neutrons from ^{12}C beam;

- the level of distortion of microdosimetry variables due to the impact of a focused ^{12}C beam with its width smaller than the TEPC diameter, *i.e.*, when the condition of random crossing of the detector by particles is violated, or due to several nuclei of fragments traversing the TEPC in a single event;

- the dose per beam particle at various points inside the water phantom and the distortion of the dose field measured with TEPC due to its finite size and gradients of the radiation field;
- the correspondence between calculated and measured $\bar{y}_F$ and LET of beam particles for various beam profiles and media surrounding the TEPC.

4.1 Modelling experimental set-up

In this study, published in Ref. [58], we calculate microdosimetric distributions and compare them with results of two experiments. In the first experiment a PMMA phantom was irradiated by broad quasi-monoenergetic neutron beams at the Japan Atomic Energy Research Institute (JAERI), Japan [98]. In the second experiment a water phantom was irradiated by carbon and lithium pencil-like beams at Gesellschaft für Schwerionenforschung (GSI), Germany [23]. The same type of TEPC device (Far West Technology Inc., model LET-1/2) was used by both groups. This allowed us to validate our calculational approach for this specific detector first with neutron irradiation data [98], and then extend it to the GSI measurements [23] with ^{12}C beam. In a previous study [55] we demonstrated that MCHIT can estimate reasonable well the energy and angular spectra of secondary neutrons produced by 200 MeV/u carbon beam in a thick water target. However, prior to calculating the contribution of secondary neutrons to the microdosimetry spectra for carbon beam one has to be confident that the response of TEPC to neutron irradiation is properly modelled. This can be proved with microdosimetry data collected with the same TEPC model, but for neutron beams. The TEPC implementation in MCHIT is described in Section 2.3.1.

Experimental results for a TEPC placed at 5 cm depth inside a PMMA phantom irradiated by 40 MeV and 65 MeV quasi-monoenergetic neutrons were selected from JAERI data to validate the MCHIT model. The energy spectra of neutrons used in the two sets of measurements [98] were modelled as superpositions of Gaussian peaks centred at 40 and 65 MeV, respectively, and broad plateaus. The ratios between the flux of neutrons with energies within the peak and the total neutron flux were set to 1:2.768 and 1:2.807 for 40 and 65 MeV spectra, respectively, following the estimations by Nakane *et al.* [98]. As proved by our simulations, the calculated $yd(y)$ distributions are not very sensitive to these ratios. For example, the calculations with these ratios set to 1:3.5 provide results similar to ones obtained with original ratios. In the following the above-described spectra composed of peaks and plateaus are referred to as "40 MeV" and "65 MeV" neutrons. The pressure of the tissue equivalent gas was 9.03 kPa which emulated a tissue sphere of 2.07 μm in diameter. The detector was located on the axis of the irradiation field and placed inside a PMMA phantom of $30 \times 30 \times 30\,\mathrm{cm}^3$. Neutrons were delivered to the phantom via a collimator of 10.9 cm in diameter, which was much larger than the diameter of the TEPC. Since neutrons traversed the device randomly at various impact parameters, the mean neutron path length $\bar{l}$ inside the sensitive volume amounted to 2/3 of its diameter. As explained in Section 1.2.1, this corresponds to the standard conditions of microdosimetry measurements [8]. A total of 4×10^8 primary neutrons were simulated for each beam energy.

In the second experiment [23] a water phantom of $30 \times 30 \times 30\,\mathrm{cm}^3$ (including side walls made of PMMA) was irradiated by a 300 MeV/u ^{12}C beam. In the simulations the parameters of the ^{12}C beam used at GSI were implemented as accurate as possible. The beam had a concentric spot with a size of 3 mm FWHM at beam exit window, an angular distribution with Gaussian profile of 1 mrad FWHM, and an energy distribution with Gaussian profile of 0.2 % FWHM. The $yd(y)$-distributions per beam particle measured at nine points inside the water phantom were reported [23]. They correspond to 0 cm, 2 cm and 10 cm radii and to three values of depth: at the plateau of the depth-dose curve, at the Bragg peak and in the tail region. In this experiment water was enclosed in a container with a 20 mm thick PMMA wall. Carbon nuclei also penetrated through a vacuum window made of aluminium, a scintillation detector and a parallel-plate ion chamber installed in front of the phantom. These beam-line elements and PMMA walls of the phantom were estimated by Martino *et al.* [23] as equivalent water thickness of 25.1 mm. This thickness was applied to the TEPC depth in order to compare the experimental data with simulation results, since calculations were performed with an equivalent wall-less water phantom of $30 \times 30 \times 30\,\mathrm{cm}^3$. It was found that a 2 mm shift to a deeper position of the detector is required in order to reproduce the peak in the $yd(y)$ spectrum for the TEPC positioned in the vicinity of the Bragg peak on the beam axis as well as the depth-dose profile. At this position the microdosimetry spectrum is highly sensitive to a few millimetres shift of the device. One can attribute this shift to uncertainties in the measurements of TEPC positions, beam energy and the equivalent water thickness in front of the water phantom. Some inaccuracy of the electromagnetic physics models of GEANT4 can not be excluded as well. For consistency this shift was applied to all detector positions as a systematic correction. The gas pressure was set to the experimental value of 12 kPa which corresponds to a sphere of tissue of 2.75 µm in diameter. The TEPC positions used in our simulations are listed in Table 4.1.

Using the axial symmetry of the set-up in the second experiment we replaced a single physical TEPC by a ring of identical virtual detectors located at the same depth and radial distance from the beam axis. During each run the lineal energy events were scored in a histogram corresponding to a particular ring. At the end of the run the number of events in each lineal energy bin were divided by the number of virtual counters in the ring and thus became equivalent to a single physical counter. With this method one can increase the simulated number of hits for those positions of counters where hits are scarce. This is particularly important for TEPCs located at large distances, *e.g.*, at 10 cm, from the beam axis. The number of counters in each ring and the positions of the rings with respect to the beam axis were chosen to avoid any crosstalk impacts on the virtual detectors. This was done to satisfy the condition that the particles produced inside one of the virtual counters, or which have just traversed it, should not hit other counters. Therefore, calculations for the nine positions listed in Table 4.1 were split into three independent runs. During the run "I" three outer rings of TEPCs of 10 cm in radius each consisting of 24 counters were placed in the water phantom. In the same run a counter on the beam axis and a ring of 2 cm in radius consisting of four detectors were placed at 27.71 cm depth. Each of the runs "II" and "III" was executed with a ring of 2 cm in radius consisting of four counters and with a single counter located at the same depth in the centre of

Table 4.1: Positions of the TEPC counters inside the water phantom used in MCHIT simulations and their labelling in the following text and figures. TEPCs were grouped into rings with a number of counters in each ring depending on the ring radius. Each detector position was modelled in a certain run labelled in the last column.

Radius (mm)	Depth (mm)	TEPC's position notation	Number of counters in the ring	Run label
0.	52.1	0 cm, plateau	1	III
0.	179.1	0 cm, peak	1	II
0.	277.1	0 cm, tail	1	I
20.	52.1	2 cm, plateau	4	III
20.	179.1	2 cm, peak	4	II
20.	277.1	2 cm, tail	4	I
100.	52.1	10 cm, plateau	24	I
100.	179.1	10 cm, peak	24	I
100.	277.1	10 cm, tail	24	I

the ring. Typically, the histories of 10^7 to 5×10^7 ^{12}C nuclei traversing the phantom were simulated in each run.

The MCHIT calculations were performed with different energy thresholds for production of δ-electrons (or with no production of δ-electrons taken as a limit case) using electromagnetic physics lists G4EmStd and G4EmPen, and also with two different nuclear fragmentation models, namely G4BIC and G4QMD. The sensitivity of calculated distributions to computational parameters can be studied by comparing these distributions with each other and with experimental data.

4.2 TEPC response to quasi-monoenergetic neutron beams

It is expected that radiation fields far from the axis of ^{12}C beam has a large contribution from neutrons produced in fragmentation of primary nuclei. Therefore, before performing microdosimetry simulations with carbon beam we checked the validity of the MCHIT code with respect to irradiation of the same TEPC model by neutrons. The experimental data obtained with quasi-monoenergetic neutron beams [98] were used for this purpose.

MCHIT results for a TEPC located at 5 cm in depth inside a PMMA phantom irradiated by "40 MeV" neutrons are shown in Fig. 4.1 together with the experimental data [98]. The results were obtained by simulating neutron-induced nuclear reactions using either G4QMD or G4BIC models. It must be mentioned, however, that G4QMD is not recommended for modelling nucleon-nucleus collisions. The number of simulated primary particles was such that the statistical fluctuations in

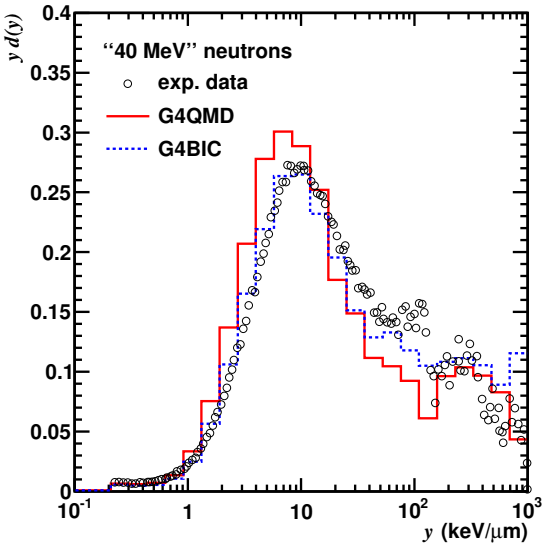

Figure 4.1: Calculated microdosimetric spectra for a TEPC at 5 cm depth inside a PMMA phantom irradiated by quasi-monoenergetic "40 MeV" neutrons. Theoretical results obtained with G4QMD and G4BIC models are presented by solid and dashed histograms, respectively. Experimental data [98] are shown by circles.

Table 4.2: Measured and calculated microdosimetry parameters for TEPC irradiated by quasi-monoenergetic neutron beams.

Beam	Parameter	Exp. data	MCHIT	
	(keV/μm)		G4BIC	G4QMD
"40 MeV"	$\bar{y}_F$	7.54	7.55	6.21
	$\bar{y}_D$	84.2	110	80.2
"65 MeV"	$\bar{y}_F$	5.51	5.33	4.75
	$\bar{y}_D$	75.2	86.1	84.2

the histogram are of the same order as those presented in the experimental data. No error bars were plotted due to the lack of error bars for the reported experimental points. Microdosimetry spectra calculated with G4BIC and G4QMD for the same set-up, but for the irradiation with "65 MeV" neutrons are shown in Fig. 4.2. The corresponding microdosimetry parameters, $\bar{y}_F$ and $\bar{y}_D$, calculated from the spectra shown in Figs. 4.1 and 4.2 are listed in Table 4.2.

Neutrons do not transfer their energy directly to the sensitive gas volume, but rather through secondary charged particles produced in neutron interactions with nuclei in the gas cavity, TEPC wall or even in surrounding layers of PMMA. Several recoil particles can be produced by a single neutron. MCHIT makes it possible to estimate partial contributions from each kind of recoil particles to the total $yd(y)$ curve. Such contributions were calculated as following. Firstly, the amount of energy deposited to the sensitive volume by every kind of particle is scored separately at

each lineal energy event. Secondly, the relative contribution to $yd(y)$ for each kind of particle in this event is calculated from the ratio between the energy deposited by particles of a given kind and the total energy deposited in the event.

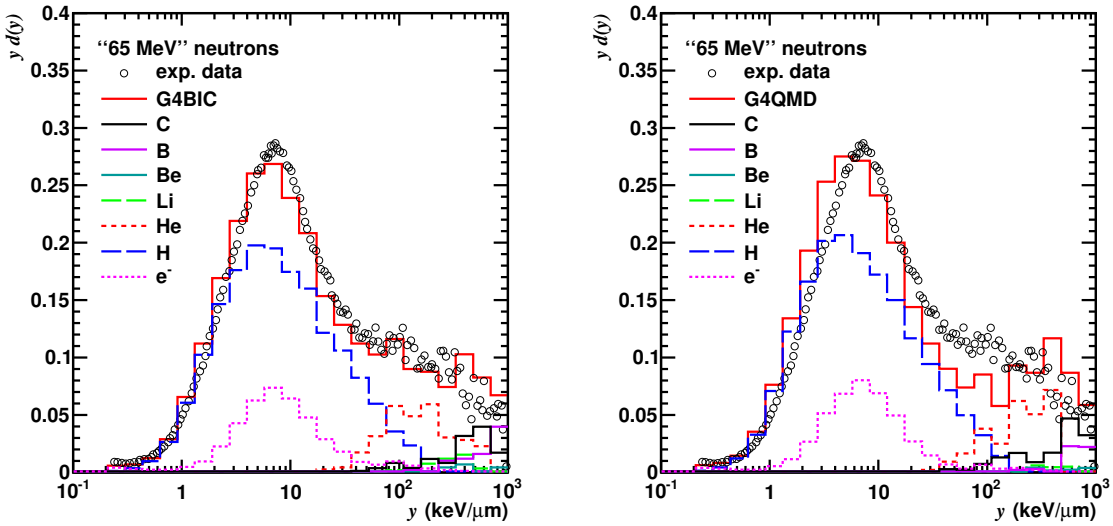

Figure 4.2: Calculated microdosimetric spectra for a TEPC at 5 cm in depth inside a PMMA phantom irradiated by quasi-monoenergetic "65 MeV" neutrons. Results of MCHIT calculations with G4BIC and G4QMD models are shown on the left and right panel, respectively. In addition to the total $yd(y)$ distribution the contributions of specific particles are shown by various histograms as explained on the legend. Experimental data [98] are shown by circles.

Contributions of specific secondary particles to the $yd(y)$ distribution for "65 MeV" neutrons obtained with G4BIC are shown in the left panel of Fig. 4.2. The origins of a peak at $y \sim 7$ keV/μm and a shoulder extending to higher y values can be identified. The peak is due to recoil protons, while the shoulder is formed by more heavy recoil nuclei, mostly by alpha-particles ($y > 30$ keV/μm) and carbon nuclei ($y > 100$ keV/μm). The contributions from boron, lithium and beryllium nuclei are much smaller and attributed mostly to $y > 200$ keV/μm. The microdosimetric distributions for "40 MeV" neutrons (not shown) were calculated in a similar way. In this case the maximum is located at $y \sim 9$ keV/μm due to less energetic primary neutrons. Therefore, neutrons transfer less energy to recoil protons, which get slower and therefore have higher stopping power.

Contributions of various recoil particles to $yd(y)$ distribution calculated with G4QMD for "65 MeV" neutrons are shown in the right panel of Fig. 4.2. MCHIT predicts more fast recoil protons (with lower stopping power) compared to experimental data. This leads to a shift of the peak of the calculated distribution to lower y. With regards to more heavy nuclei, the results obtained with G4QMD model differ from measurements at $y \sim 100$ keV/μm where energy deposition events are mostly caused by helium nuclei. This can be explained by an underestimation of alpha-particle yields in neutron-induced reactions simulated by this model.

As shown in this section, the MCHIT model with G4BIC applied to simulate neutron-induced reactions demonstrates a better agreement with experimental data compared to MCHIT with G4QMD. The maximum of the theoretical $yd(y)$ distri-

butions calculated with G4QMD is slightly shifted to lower y values with respect to the measurements [98]. The proton edge at $y \sim 100\,\mathrm{keV}/\mu\mathrm{m}$ is better reproduced by G4BIC. The measured $\bar{y}_F$ is well reproduced by G4BIC, but $\bar{y}_D$ is overestimated for "40 MeV" neutrons due to a higher probability of large size events. G4QMD underestimates the frequency-mean lineal energy by 14–18 % but better reproduces the dose-mean lineal energy compared to G4BIC. Nonetheless, the overall shape of the microdosimetry spectra and the magnitude of microdosimetry parameters for quasi-monoenergetic neutrons are reasonably well reproduced by MCHIT using both G4BIC and G4QMD models. One can note a better agreement between the measured [98] $yd(y)$ distributions and MCHIT calculations as compared with the PHITS code used for modelling [99] the same TEPC measurements [98]. This can be explained by the fact that in those PHITS calculations [99] the production and transport of δ-electrons were neglected, while these processes are taken into account in our MCHIT simulations.

4.3 TEPC response to a therapeutic ^{12}C beam

Now we turn to the central part of our study where we use MCHIT to model the response of the TEPC to a pencil-like therapeutic ^{12}C beam. We start with calculating the numbers of particles which traverse the detector placed at various positions in a water phantom and then continue with the distributions of the total track length inside the sensitive volume and with microdosimetry spectra.

4.3.1 Number of particles which cross the TEPC

As described above in Section 1.2.1, the lineal energy of a particle traversing a spherical TEPC can be estimated by dividing the energy ϵ imparted to the detector by the mean chord length $\bar{l} = 2d/3$, where d is the diameter of the sensitive volume. This estimation is based on the assumption that the device is placed in a homogeneous radiation field and traversed by a single particle per event. This corresponds to the simplest standard event topology characterized by a single track with $l \leq d$. This means that the particle traverses the sensitive volume by a straight-line trajectory, it is not stopped inside the volume, and secondary particles are not produced neither in the volume nor in the vicinity of it.

In the experiment with ^{12}C ions [23] the TEPC was irradiated either directly by a focused beam, or hit only by secondary particles at detector locations outside the beam spot. In this section we investigate the event topology relevant to both cases. Indeed, on the contrary to the measurements with neutron beams described in Section 4.2, the size of the ^{12}C beam was essentially smaller (3 mm FWHM) compared to the diameter of the sensitive volume ($d = 12.7$ mm). Therefore, for a TEPC placed on the beam axis at the plateau region of the depth-dose distribution and, possibly, close to the Bragg peak, the mean chord length will be larger than $2d/3$ due to mostly central beam incidence. Moreover, several secondary particles can impact the detector in a single event. In this section we investigate whether the irradiation conditions match the standard ones for which the mean chord length $2d/3$ is used to calculate lineal energy y for a single particle traversal.

Since a TEPC is only sensitive to the total energy ϵ deposited to its volume given by the number of ionized atom-electron pairs produced in the gas chamber, the number of tracks in each event and their length (event topology) can not be identified in experiment. However, one can retrieve this information from MCHIT simulations by scoring the number of tracks and their total length inside the detector. The probability distributions for the number of tracks $f(N)$ inside the sensitive volume are shown in Fig. 4.3. The distributions are calculated for the events with at least one particle traversing the TEPC, and they are given at nine positions in the water phantom listed in Table 4.1. These distributions are calculated per single beam particle and represent the probability for a detector placed at a certain position in the phantom to be traversed by N particles of any kind, where $N = 1$ corresponds to the standard event topology defined above despite of multiple δ-electrons stopped inside the sensitive volume. The tracks of the particles which do not deposit energy to the TEPC are also included.

The distributions presented in Fig. 4.3 were calculated with and without production of δ-electrons using the standard electromagnetic models. In the latter case only secondary nucleons and nuclear fragments were produced and counted while they traversed the TEPCs. As one can see from the distribution calculated at "0 cm, plateau", the detector at this location is traversed by a single particle with $\sim$0.85 probability. This reflects the attenuation of the primary beam in the first 5 cm of water. On the contrary, the probability to hit the device at "10 cm, tail" position far from the beam axis is only $\sim$0.0057 per beam particle. As deduced from the comparison of the distributions calculated with and without generating δ-electrons, TEPCs placed on the beam axis at the plateau and the Bragg peak are usually traversed by several electrons in addition to nucleons and nuclei.

The event topology associated with the traversing of the TEPC by one or several particles, can be characterized by the average number of tracks $\bar{N}$ calculated per event. These average numbers are presented in each panel of Fig. 4.3 for both calculational options – with and without δ-electrons. When the production of δ-electrons is neglected, the most probable events are characterized by a single particle track, with $\bar{N} = 1.5$ and 1.4 under the direct impact of the beam at the plateau and peak, respectively. However, when the production of δ-electrons is considered, $\bar{N} = 3.6$ at the plateau and $\bar{N} = 2.7$ at the Bragg peak position. Although these electrons deliver less energy to the sensitive volume when compared to beam nuclei, their contribution can affect the results of simulations. As demonstrated in Fig. 4.3, the N-distributions and $\bar{N}$ calculated for other seven positions are less affected by neglecting δ-electrons. At these positions the TEPCs are not directly impacted by the ^{12}C beam. When a lower energy threshold of 100 eV is used with the Penelope models, the average number of tracks on the beam axis is increased at the plateau to 3.7 and the Bragg peak position to 3.1, but for all other positions $\bar{N}$ does not change.

The probability distributions $f(l)$ for the total track length l scored for particles traversing the TEPC at different locations in the water phantom are shown in Fig. 4.4. The values of $\bar{l}/d$ calculated per event of detector traversing are also given for each position in the phantom. The irradiation of TEPCs by a thin ^{12}C beam is clearly reflected in the $f(l)$-distributions calculated for "0 cm, plateau" and "0 cm, peak". As one can note, these two distributions present a pronounced peak

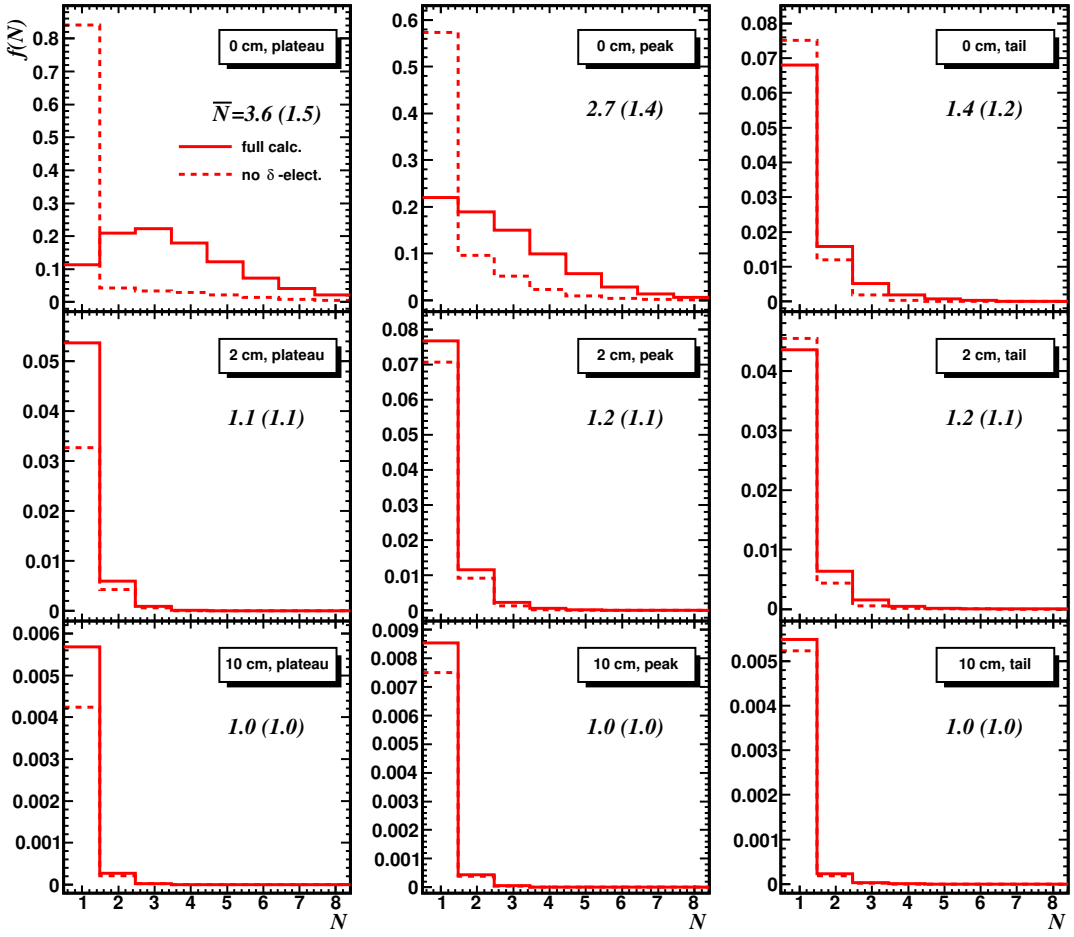

Figure 4.3: Probability distributions for the number of tracks in TEPCs at different locations in the water phantom irradiated by 300 MeV/u ^{12}C beam. The condition to have at least one track in the corresponding TEPC is applied. The distributions with and without simulation of δ-electrons are presented by solid- and dashed-line histograms, respectively, and calculated per beam particle. The average number of tracks $\bar{N}$ per traversing event are presented for each TEPC location, and the values obtained without δ-electrons are given in parentheses.

at the track length corresponding to the diameter of the gas cavity and a broad tail for higher track lengths with $\bar{l}/d$ much larger than $2d/3$ due to secondary electrons and beam fragments. These distributions contrast to the linear dependence of $f(l)$ versus l (for $l < d$) found at all other positions which indicates a random particle incidence on the gas cavity. At "0 cm, tail" $\bar{l}/d$ is still large, $\bar{l}/d \sim 0.936$, due to multiple tracks in a single event. Some events with two and three nucleons or nuclei in the TEPC are characterized by $l > d$ at "0 cm" positions, as already demonstrated in Fig. 4.3. The distributions at the radius of 2 cm still exhibit the presence of one and two tracks of nucleons or nuclei in the detector. The mean chord length is close to $2d/3$ only for the TEPCs at the radius of 10 cm. The probability of an event with two particles in the sensitive volume is negligible there.

The analysis of $f(N)$ and $f(l)$ distributions given in this section demonstrates different event topologies in the TEPCs placed at the beam axis and far from the

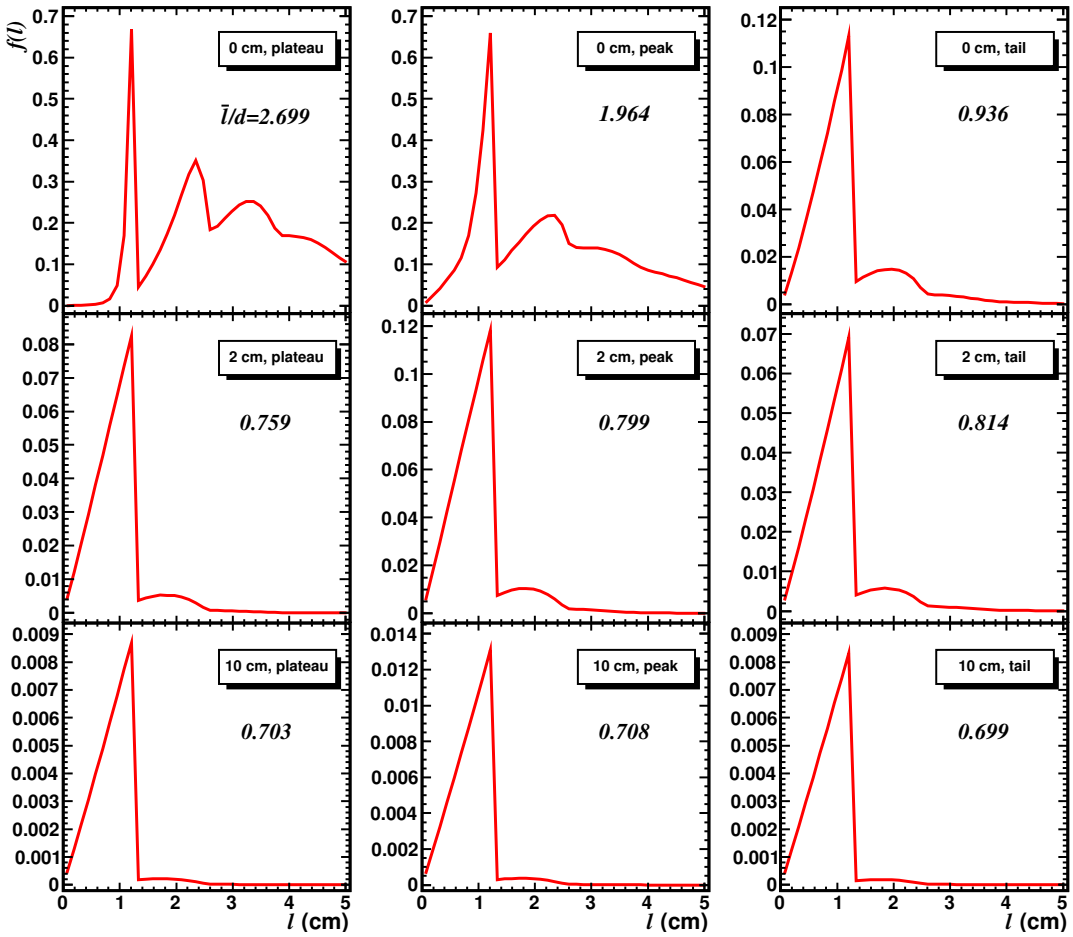

Figure 4.4: Probability distributions for the total track length for particles traversing the TEPCs at different locations in the water phantom irradiated by 300 MeV/u ^{12}C beam. The condition to have at least one track in the TEPC is applied. The calculations were performed with production of δ-electrons using the standard electromagnetic models. The average values of $\bar{l}/d$ calculated per event are listed for each TEPC position.

beam. In the latter case the events are mostly characterized by the simplest standard topology associated with a single track of nucleon or nuclear fragment traversing the sensitive volume. On the contrary, the events in the detectors placed on the beam axis at the entrance to the phantom ("0 cm, plateau") and at the Bragg peak ("0 cm, peak") are more complicated. A part of events is characterized by one or two tracks of beam nuclei, secondary nucleons and/or nuclear fragments traversing the sensitive volume. In addition, tracks of two, three or more energetic electrons are frequently present in the TEPCs placed on the beam axis.

4.3.2 Lineal energy spectra inside the water phantom

Following the consideration given above to the particle track patterns in TEPCs, in Figs. 4.5 and 4.6 we present calculated microdosimetric $yd(y)$ distributions. The experimental data [23] were reported only above 0.3–0.5 keV/µm. In order to facilitate the comparison with the experimental data this range was also used to plot cal-

culated microdosimetry spectra and calculate $\bar{y}_F$ and $\bar{y_D}$. We found that the integral of the $f(y)$ distribution normalized per beam particle measured at "0 cm, plateau" gives 1.17, while a value less or equal to 1.0 is expected. Due to a slight beam attenuation the integral of the distribution calculated with MCHIT amounts to 0.987 at "0 cm, plateau". The reason of this excessive recording of events of the experimental microdosimetry spectra is not known, but one can assume that this effect is present at all other TEPC positions. Therefore, in Figs. 4.5 and 4.6 we multiplied all measured $yd(y)$ distributions by a factor of $0.987/1.17 = 0.844$. This renormalization restores the consistency with the calculated numbers of events in the detector placed on the beam axis at the "0 cm, plateau" position.

As discussed in Section 4.3.1, for the detectors placed on the beam axis $\bar{l} > 2d/3$ since a certain number of events is characterized by more than one track traversing the sensitive volume, and events with small impact parameter are more frequent. However, in GSI measurements [23] $\bar{l} = 2d/3$ was assumed following the standard microdosimetry technique [8]. The same normalization was taken in our calculations of y for the sake of a direct comparison with experimental data.

The microdosimetric $yd(y)$ distributions measured at GSI [23] inside the water phantom irradiated by a 300 MeV/u ^{12}C beam are shown in Fig. 4.5 together with our simulation results. The distributions are given per beam particle for the same TEPC positions inside and outside the beam spot as listed in Table 4.1 and described in Section 4.1.

The influence of the energy threshold for production and transport of δ-electrons can be estimated by considering $yd(y)$ distributions obtained with and without simulating electron production, but with the same nuclear fragmentation model, as shown in Fig. 4.5. Here, the distributions calculated with these two options noticeably differ at the "0 cm, plateau" position close to the beam entrance to the phantom. In particular, the number of energy deposition events with $20 < y < 200$ keV/µm is much higher compared to the calculation with δ-electrons. At this point fast beam nuclei produce energetic electrons which may escape from the sensitive volume and thus reduce the energy deposited to the TEPC. However, the $yd(y)$ distribution calculated at the Bragg peak (at "0 cm, peak") is not affected by neglecting δ-electrons. Much more secondary electrons are produced close to the Bragg peak, but they are generally less energetic compared to those at "0 cm, plateau" and do not escape from the TEPC. This means that the energy deposited to the detector at "0 cm, peak" can be simply calculated from the stopping power of beam nuclei even without modelling δ-electrons.

As seen from Fig. 4.5, the production of δ-electrons changes the distributions in the range of $1 < y < 100$ keV/µm for the devices located at 2 cm from the beam axis. Similar, but smaller changes in the $yd(y)$ distributions associated with electron production are also found at 10 cm radii. At all these positions energy is deposited to the TEPC mostly by protons, and their contribution is reduced if secondary electrons are produced and escape the sensitive volume. The $yd(y)$ distributions with production and transport of δ-electrons are not sensitive to a change in the lowest energy threshold from 990 eV to 100 eV with Penelope models (results not shown).

MCHIT results obtained with G4BIC and G4QMD models used to simulate nuclear fragmentation are presented in Fig. 4.6 together with experimental data [23].

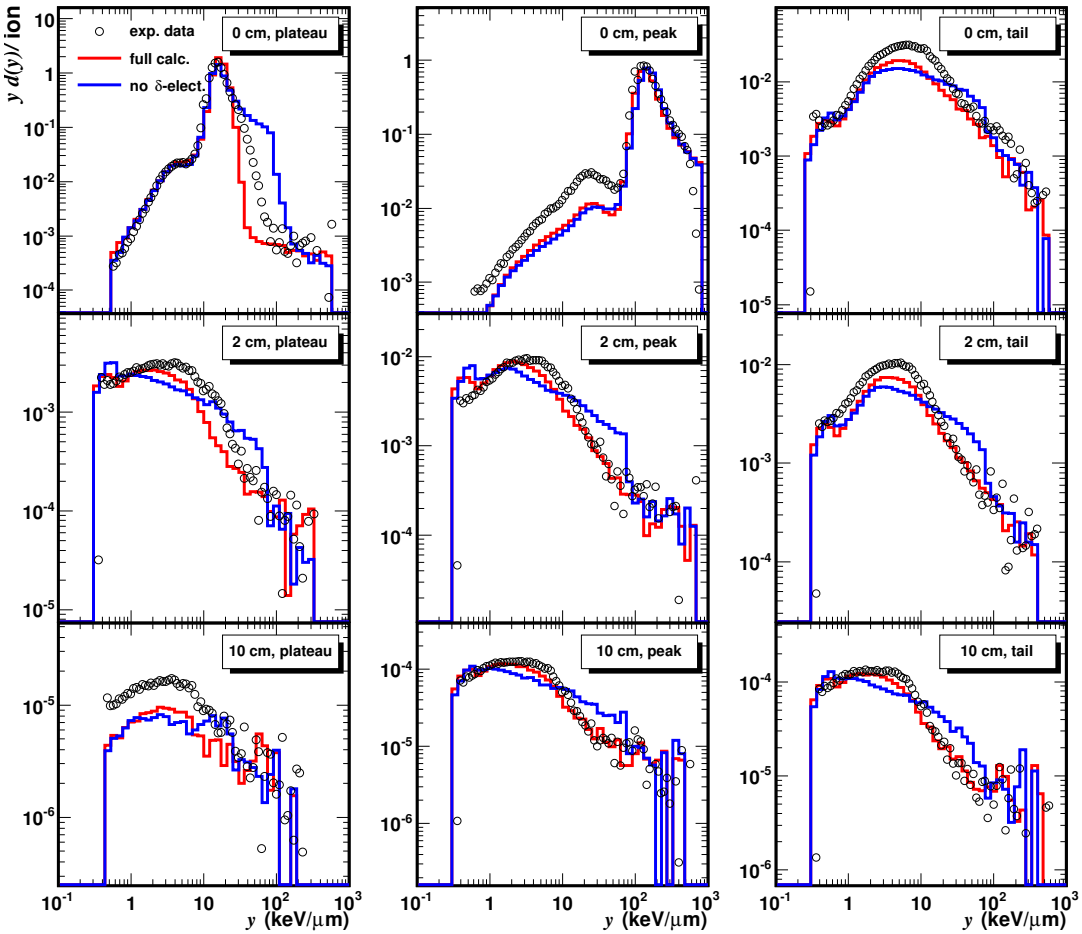

Figure 4.5: Microdosimetric $yd(y)$ distributions in water phantom irradiated by 300 MeV/u ^{12}C nuclei. Distributions calculated by MCHIT per beam particle with and without simulating δ-electrons are presented by red- and blue-line histograms, respectively. Electromagnetic interactions are simulated with G4EmStd, while nuclear reactions with G4QMD. Circles represent experimental data [23].

A detailed consideration of the contributions of specific nuclear fragments to the calculated microdosimetric spectra is presented in Sections 3.2 and 5.2.5. Here only general features of the $yd(y)$ distributions are discussed. One has to keep in mind the range of magnitudes of the distributions presented in the nine panels of Figs. 4.5 and 4.6. They are normalized per single beam particle and have a span of almost six orders of magnitude. This is because of the fact that TEPC hits at the position "10 cm, plateau" are approximately 10^4 times less frequent than at the Bragg peak ("0 cm, peak"), as described below in Section 4.3.3. The detectors located at 10 cm distance from the beam axis are hit exclusively by secondary particles (mostly nucleons) produced in nuclear fragmentation reactions. Therefore, the microdosimetry data [23] provide another possibility to validate the nuclear fragmentation models of GEANT4.

In the measurements [23] a sharp peak in the spectrum is observed at the position "0 cm, plateau". It is located at $y \sim 16$ keV/μm, and its position is well reproduced by the MCHIT simulations with both G4BIC and G4QMD. However, as seen from

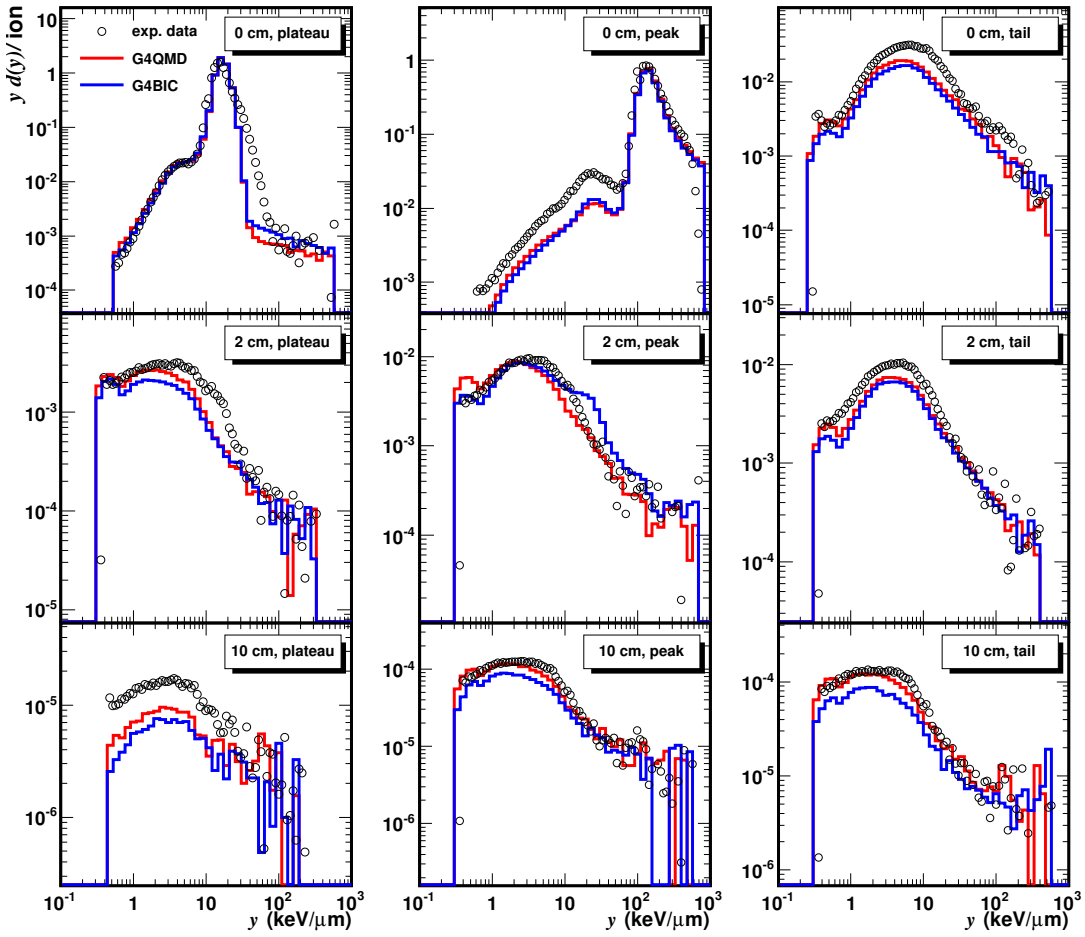

Figure 4.6: Microdosimetry spectra in water phantom irradiated by 300 MeV/u ^{12}C nuclei calculated by MCHIT with standard electromagnetic models including production and transport of δ-electrons and G4QMD and G4BIC options for nuclear fragmentation, shown as red- and blue-line histograms, respectively. Circles represent experimental data [23].

the corresponding panel of Fig. 4.6, MCHIT predicts a slightly sharper drop of $yd(y)$ at the right slope of the peak. This peak is due to energetic beam nuclei that traverse the TEPC at the entrance to the phantom. As discussed in Section 4.3.1, because of a relatively small beam diameter (3 mm FWHM) compared to the detector size, carbon nuclei propagate close to the diameter of the TEPC.

As seen in the panel "0 cm, peak", the peak in the $yd(y)$ distribution corresponding to ^{12}C nuclei becomes higher and broader as the detector is moved to the stopping point of beam nuclei. Compared to the "0 cm, plateau" panel, here the peak is shifted to a much higher value of $y \sim 131$ keV/μm, and it has a prominent satellite peak with a maximum at $y \sim 25$ keV/μm. The positions of both peaks are well reproduced by simulations. The observed shift of the main peak to larger y is due to increasing the LET of beam nuclei as they are slowing down with their penetration in water.

A common feature of the "0 cm, plateau" and "0 cm, peak" distributions consists in the presence of additional peaks at lower y values compared to the peaks of

beam nuclei. Such satellite peaks are present due to relatively heavy projectile fragments (boron, beryllium and lithium nuclei) propagating with velocities close to the velocity of beam nuclei. Since their Z^2 are smaller, their ionization energy-loss is reduced accordingly. This leads to reduced LET of secondary fragments compared to beam nuclei. While the satellite peak is accurately reproduced by theory at the entrance to the phantom at "0 cm, plateau", a similar peak at the position "0 cm, peak" is underestimated. This indicates, that the yields of secondary fragments are underestimated by the nuclear fragmentation models used in MCHIT.

The spectrum at the beam axis beyond the Bragg peak ("0 cm, tail") and all the six spectra at 2 and 10 cm radii do not demonstrate any sharp peak. This is because of contributions from various secondary light particles characterized by a broad range of kinetic energies and charges. It is expected that recoil charged particles produced in neutron-induced reactions also contribute to these spectra. This contribution is estimated below in Section 4.3.5. While the general trends of the distributions measured at these seven positions are reproduced by MCHIT, the absolute values are underestimated by a factor of two or slightly less. In view of a 10^4 difference in magnitude between "0 cm, tail" and "10 cm, plateau" distributions, such level of agreement between MCHIT and experimental data can be accepted. Nevertheless, this discrepancy suggests that there is still a room for improvements of the considered nucleus-nucleus collision models of GEANT4, G4BIC and G4QMD, or de-excitation models.

4.3.3 Hit probability, $\bar{y}_F$, $\bar{y}_D$ and dose inside the water phantom

We consider now the average microdosimetric quantities $\bar{y}_F$ and $\bar{y}_D$ defined in Section 1.2.1 as well as the total dose at various positions inside the water phantom irradiated by 300 MeV/u ^{12}C nuclei. The total dose calculated at various distances from the beam axis is shown in Fig. 4.7 as a function of the depth in water together with experimental results [23].

As explained by the caption of Fig. 4.7, calculated doses were obtained by two different methods. In the first method labelled as "MCHIT (TEPC)" the dose delivered to the tissue-equivalent gas was computed from microdosimetry spectra by calculating firstly $\bar{y}_F$ and then dose itself according to Eq. (1.5). In the second method calculations were performed in water without placing TEPCs. A set of concentric rings was defined inside the phantom with 0.1 mm steps in the depth and radius. At the end of each run the energy imparted to each ring was calculated and then divided by the mass of the ring and by the number of beam particles. Due to a finite size of the detector, particles traverse it at various distances from the beam axis. Therefore, in calculating the dose without TEPC one has to take an average dose value for a characteristic volume of a similar size. For example, the average dose for 0–6.35 mm radii was calculated to obtain the dose on the beam axis. The radial ring thickness for dose calculations was set to 2/3 of the diameter of the sensitive volume at other distances from the beam axis.

The calculated dose values obtained by MCHIT by explicit modelling of the TEPC agree well with the experimental data at most of the device positions, see Fig. 4.7. However, the dose at "0 cm, plateau" is underestimated due to the fol-

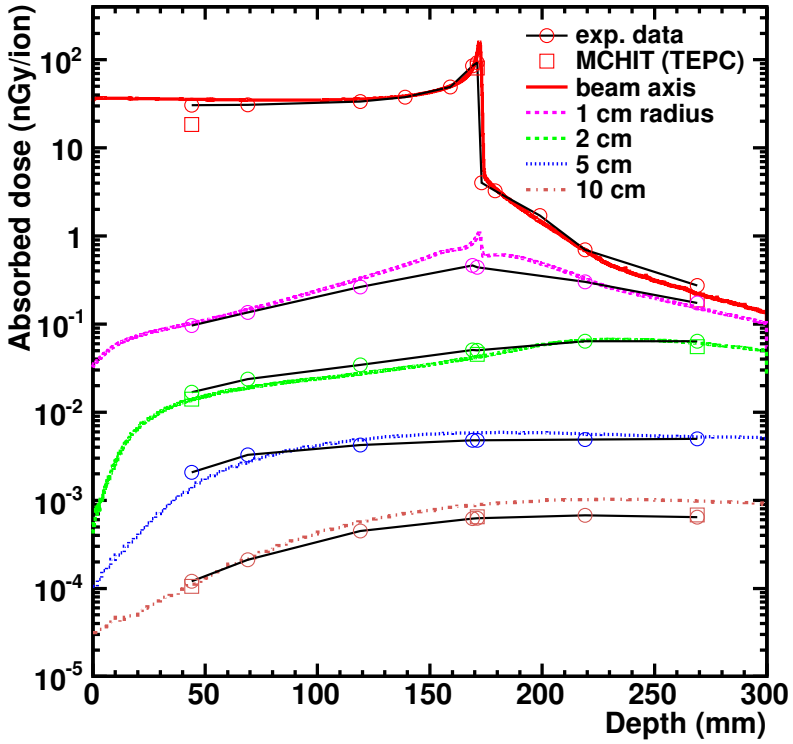

Figure 4.7: Calculated and measured total doses at various depths in the water phantom irradiated by 300 MeV/u ^{12}C nuclei. The doses calculated at 0, 2 and 10 cm radii from microdosimetry spectra by means of Eq. (1.5) are shown by open squares. Lines of various styles explained on the legend present total dose calculated in water by direct scoring of energy deposition at 0, 1, 2, 5 and 10 cm radii. The measured doses [23] are shown by open circles connected by dark solid lines to guide the eye.

lowing two reasons. Firstly, the number of events in the range $25 < y < 80$ keV/µm is underestimated at "0 cm, plateau", see Fig. 4.5. Secondly, the average number of events per beam particle which is estimated from the microdosimetry spectra measured at this point is higher than 1, on the contrary to what is predicted by simulations, as explained in Section 4.3.2.

The dose values calculated in the water phantom without detector agree well with the TEPC-based measurements and TEPC-based simulations except the points in the vicinity of the Bragg peak. As expected, these points are characterized by high dose gradients which are predicted by calculations without detector, *e.g.* at 1 cm radius. These dose gradients are smoothed by taking average values in water over the above-described rings. However, the dose in TEPC-based measurements still differs from the dose calculated without detector in the Bragg peak region at 1 cm radius.

Figure 4.8 gives further insight into the influence of a finite size of the device on microdosimetry measurements with therapeutic pencil-like beams. The doses from TEPC-based simulations, calculations without detector and measured doses agree well with each other at 2 cm distance from the beam axis. The same is true for the measurements performed on the beam axis in the tail. In all these cases

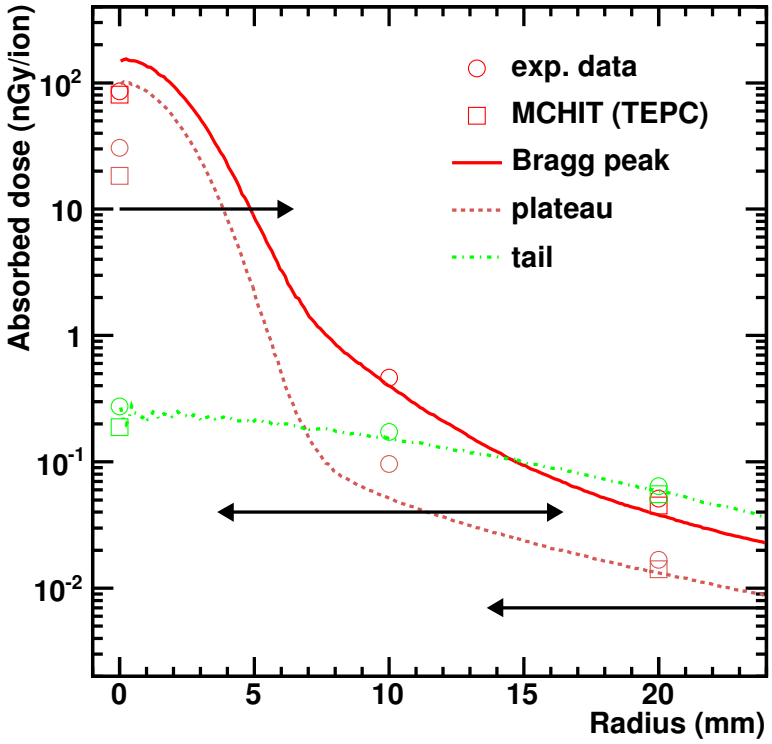

Figure 4.8: Calculated and measured total dose in the water phantom irradiated by 300 MeV/u ^{12}C nuclei as a function of the distance from the beam axis. The doses calculated on the beam axis and 20 mm away from it according to Eq. (1.5) are shown by open squares. Lines of various styles explained on the legend present total dose calculated in water by direct scoring of energy deposition at the plateau (44.04 mm depth), Bragg peak (171.04 mm) and tail (269.04 mm). The measured doses [23] are shown by open circles. Lines with arrows demonstrate the radial ranges covered by the TEPC placed at 0, 10 and 20 mm from the beam axis.

the spatial dose distribution is characterized by relatively small gradients inside the sensitive volume which suggests good agreement between calculations with and without detector. While a good agreement is observed between experimental data and TEPC-based simulations, direct calculations of the dose differ from both of them on the beam axis at the plateau and peak. As seen, the local dose at the centre of the sensitive volume is generally 2–3 times higher than the TEPC-measured and TEPC-simulated doses under the focused irradiation of this TEPC by 3 mm FWHM pencil-like beam. Our results suggest that a good agreement between measured and calculated doses can be obtained only by direct modelling of the detector geometry, and not by scoring the dose in simulations without TEPC, as done by other authors [95, 96].

The calculated frequency-mean $\bar{y}_F$ and dose-mean $\bar{y}_D$ lineal energies are given in Tables 4.3 and 4.4. The corresponding values calculated from experimental microdosimetric distributions are also given in these tables for comparison. In addition, the probability P_{TEPC} of energy deposition event at a given position is also listed in Table 4.3. From these probability values one can conclude, for example, that on average there is one deposition event per $\sim$3000 beam particles for the detectors

Table 4.3: Probabilities to deposit energy in the TEPC per beam particle at various positions inside the water phantom and the corresponding $\bar{y}_F$ calculated per energy deposition event. The calculations were performed with G4EmStd physics list. The results obtained with G4EmPen are given in the fourth column. The values of $\bar{y}_F$ calculated from experimental [23] $yd(y)$ distributions are given for comparison.

TEPC's position	P_{TEPC}	$\bar{y}_F$ (keV/µm)		
	MCHIT	MCHIT		GSI
	G4EmStd	G4EmStd	G4EmPen	experiment
0 cm, plateau	$9.87 \cdot 10^{-1}$	14.8	15.2	15.1
0 cm, peak	$6.44 \cdot 10^{-1}$	97.4	99.2	78.7
0 cm, tail	$5.10 \cdot 10^{-2}$	2.89	3.27	3.52
2 cm, plateau	$8.25 \cdot 10^{-3}$	1.24	1.34	1.69
2 cm, peak	$2.43 \cdot 10^{-2}$	1.39	1.54	2.01
2 cm, tail	$2.01 \cdot 10^{-2}$	2.13	2.36	2.41
10 cm, plateau	$3.19 \cdot 10^{-5}$	2.21	2.18	2.13
10 cm, peak	$3.62 \cdot 10^{-4}$	1.33	1.48	1.65
10 cm, tail	$3.87 \cdot 10^{-4}$	1.31	1.40	1.59

placed 10 cm away from the beam axis, both at the peak and tail regions. The MCHIT results for $\bar{y}_F$ obtained with the Penelope models are higher than those with the G4EmStd physics list by 1–10 % depending on the position. The measured $\bar{y}_F$ value on the beam axis at the plateau is well described by calculations while it is overestimated by $\sim$25 % at the peak. While calculated with G4EmPen $\bar{y}_F$ agree very well with $\bar{y}_F$ measured at "2 cm, tail" and "10 cm, plateau" positions, the calculated $\bar{y}_F$ are smaller compared to measured values by 10–20 % at other four positions where TEPCs are mostly hit by secondary protons and neutrons.

The calculated and measured $\bar{y}_D$ values are presented in Table 4.4. As seen from the table, $\bar{y}_D$ calculated with G4EmStd and G4EmPen physics lists agree well with each other and with experimental data at the beam axis. The difference between calculated and measured values increases as the distance to the beam axis increases. As only protons and neutrons contribute for TEPC positions far from the beam, this discrepancy points at the necessity to improve the description of production of these secondary particles by GEANT4 models.

4.3.4 Relations between $\bar{y}_F$ and LET

As discussed in Section 4.3.1, the TEPC response to focused and homogeneous irradiation is different. It can be also influenced by the media which surrounds the detector, as particles produced in this media, *e.g.* in fragmentation reactions, also hit the detector. In the continuous slowing down approximation, it is expected [8] that the relation:

$$\bar{y}_F = L \ , \tag{4.1}$$

Table 4.4: Calculated and measured [23] $\bar{y}_D$ per energy deposition event in each TEPC. The results obtained with G4EmStd and G4EmPen physics lists are given in the second and third column, respectively. The experimental values were obtained by integrating $yd(y)$ distributions normalized per event.

TEPC's position	$\bar{y}_D$ (keV/μm)		
	MCHIT		GSI
	G4EmStd	G4EmPen	experiment
0 cm, plateau	16.9	17.2	18.1
0 cm, peak	177.	181.	170.
0 cm, tail	13.3	13.7	14.3
2 cm, plateau	6.67	5.68	7.40
2 cm, peak	8.22	8.81	9.06
2 cm, tail	10.4	10.6	9.79
10 cm, plateau	14.7	12.5	13.5
10 cm, peak	11.5	16.8	10.6
10 cm, tail	11.3	15.0	9.25

should hold for a spherical TEPC randomly traversed by particles with a constant LET L, in the case when the production of δ-electrons and other secondary particles is neglected. The relations between measured, simulated $\bar{y}_F$ and LET under various conditions can be assessed by considering Table 4.5. In addition to $\bar{y}_F$ calculated with default physics settings of MCHIT and labelled with (a); the results obtained with the Penelope models used for production and transport of electrons (b); without simulating the production and transport of δ-electrons (c); and without simulating nuclear reactions (d) are presented.

In Table 4.5 the results for the TEPC placed at "0 cm, plateau" at the depth of 52.1 mm in water under the impact of 3 mm FWHM beam at the entrance of the phantom are presented, cases (1a), (1b), (1c) and (1d). At this position the energy of ^{12}C ions at the entrance to the TEPC volume is estimated as $\sim$218 MeV/u, and it is close to the beam energy of 220 MeV/u used by Taddei *et al.* [17] for homogeneous irradiation of a similar TEPC, but surrounded by air [17]. The thickness of the TEPC wall was twice as large (2.54 mm) compared to the TEPC used at GSI, and their detector operated at different tissue-equivalent gas pressure (effective diameter of 3 μm). Furthermore, those energy deposition events in the sensitive volume due to outcoming nuclei different from the incoming beam nuclei (fragmentation events) were ruled out in the experimental method. All these details were taken into account in our simulations. The comparison of these various irradiation conditions is presented in Table 4.5.

The $\bar{y}_F$ of 14.8 keV/μm calculated with MCHIT in the case (1a) for TEPC in water is quite close to the experimental result of GSI (15.1 keV/μm) and LET (15.23 keV/μm). In the case (1b) the Penelope models with the production and transport of δ-electrons extended to lower electron energy provide a larger $\bar{y}_F$, of

Table 4.5: Calculated and measured frequency-mean lineal energy $\bar{y}_F$ per energy deposition event in the TEPC. Results are given for a Gaussian-shape 3 mm FWHM beam profile (1,2) and for homogeneous irradiation of the TEPC (3) surrounded by water (1) or air (2,3). Calculations with various physics settings are marked by letters: (a) default MCHIT physics (*i.e.*, G4EmStd physics list and G4QMD model); (b) the Penelope model for electrons; (c) without simulation of δ-electrons; (d) without simulation of nuclear fragmentation. Experimental data by Martino *et al.* [23] (1) and Taddei *et al.* [17] (3) are given for comparison with MCHIT results. LET values calculated [100, 101] according to ICRU Report 73 [67] are also given.

Case	Beam energy (MeV/u)	Beam profile	Media	$\bar{y}_F$ (keV/µm)			LET (keV/µm)
				Calculation		Exp. data Martino *et al.*	
				MCHIT	Taddei *et al.*	Taddei *et al.*	ICRU 73
(1a)	218	Gaussian	water	14.8		15.1	15.23
(1b)	218	Gaussian	water	15.2		15.1	15.23
(1c)	218	Gaussian	water	16.2		15.1	15.23
(1d)	218	Gaussian	water	16.5		15.1	15.23
(2a)	220	central incidence	air	20.4			15.14
(3a,d)	220	flat	air	13.8	14.5	13.4	15.14
(3b,d)	220	flat	air	14.1	14.5	13.4	15.14

15.2 keV/µm, due to the enhancement of energy deposition inside the gas cavity by low-energy δ-electrons produced in the plastic shell. In the case (1c) the production of δ-electrons is neglected in the calculation, and $\bar{y}_F$ increases to 16.2 keV/µm and exceeds the corresponding LET. This is because of additional energy deposition in the sensitive volume which otherwise would be taken away by secondary electrons propagating beyond the TEPC. The case (1d) presents calculations performed with taking into account secondary electrons, but neglecting beam fragmentation. This means that instead of the mixture of ^{12}C beam nuclei and secondary fragments, which hit the TEPC in the cases (1a), (1b) and (1c), the detector is traversed only by ^{12}C nuclei and due to their higher Z^2 factor, $\bar{y}_F$ increases to 16.5 keV/µm, well above the measured $\bar{y}_F$ and also LET. This also explains the value of $\bar{y}_F$ calculated for the conditions of the second experiment, but with central incidence of ^{12}C nuclei on TEPC, case (2a). There the beam fragmentation outside the detector is negligible as it is surrounded by air. Since in this case the TEPC is traversed exclusively by ^{12}C nuclei along its diameter, this explains the largest energy deposition, and hence the largest $\bar{y}_F$ of 20.4 keV/µm calculated for this case.

In order to demonstrate the dependence of $\bar{y}_F$ on the beam shape, the case of a flat beam (3) was also considered. In this case $\bar{y}_F = 13.8$ keV/µm. This is noticeably smaller than $\bar{y}_F$ of the case (2a), 20.4 keV/µm, calculated for the central-incidence of ^{12}C ions of the same energy. The ratio between $\bar{y}_F$ for the random impact on the

TEPC (3) and for the central beam incidence (2) is remarkably close to the expected value of 2/3. One can note that the MCHIT results for the flat beam are closer to the experimental value than the value calculated by Taddei *et al.* [17] with another version (7.1) of the GEANT4 toolkit. We attribute this improvement to the changes in electromagnetic models done since the release of the version 7.1 and to differences in calculational parameters. However, all calculated and measured $\bar{y}_F$ for the flat beam are smaller by $\sim 10\,\%$ compared to LET.

Our results demonstrate that depending on the beam profile the measured $\bar{y}_F$ are either $\sim 35\,\%$ higher than corresponding LET for central beam incidence, case (2a), or $\sim 10\,\%$ lower than LET for homogeneous irradiation, case (3). At the same time, for the case of TEPC irradiation by the Gaussian-shape 3 mm FWHM beam typical for scanning-beam therapy facilities, which is an intermediate case with respect to (2a) and (3), the correspondence between calculated $\bar{y}_F$ and LET is good. As follows from this analysis, the exact modelling of TEPC irradiation conditions (the beam profile and surrounding media) is crucial for reproducing experimental data.

4.3.5 Contributions of secondary neutrons

The assignment of energy-dependent weighting factors is crucial for calculating equivalent doses for neutrons, *e.g.*, in radiation protection. As discussed in several publications, the calculations of dose from secondary neutrons in proton [102–104] and heavy-ion [105] therapy are prone to various uncertainties. First, there are common difficulties for all kinds of radiation in estimating the risks from low doses [106]. Second, depending on the kind of tissue under irradiation *in vivo* and neutron energy, the RBE varies from 2 to 50 [107] or even from 7 to 70 [108]. Third, the fraction of neutrons in complex radiation fields surrounding therapeutic beams should be also properly evaluated, as discussed in this section.

The calculations presented above in Section 4.2 demonstrate that fast neutrons deposit energy to tissue-like media mostly by recoil protons. Neutrons produced in fragmentation reactions during ion-beam cancer therapy can travel long distances before they interact, thus depositing energy all over the patient's body. This issue was specially investigated with MCHIT [51] with the conclusion that the neutron doses in carbon and proton therapy are of the same order, about 1 % of the total dose. As demonstrated by recent measurements [24], the dose from secondary neutrons in passive carbon-ion therapy is indeed comparable to the neutron dose in proton therapy. However, it is not yet clear whether neutrons produced during proton or carbon treatments essentially elevate the risk of secondary cancer [102–105].

The contributions of secondary neutrons to the microdosimetric spectrum can be measured applying a veto counter technique which classify events due to charged or neutral particles. This technique was used elsewhere for 290 MeV/u carbon beam in acrylic phantom [109] and 200 MeV/u carbon beam in water phantom [110]. Endo *et al.* found that the neutron contribution to the deposited dose in the tail was 18 % on the beam axis and 51 % at 10 cm radius [109]. For larger distances from the beam axis the neutron dose is predominant, increasing from 74 % in forward direction to 89 % in backward direction at 15 cm radius [109].

In GSI measurements [23] contributions to microdosimetric quantities from secondary neutrons were not identified. However, Monte Carlo simulations with MCHIT

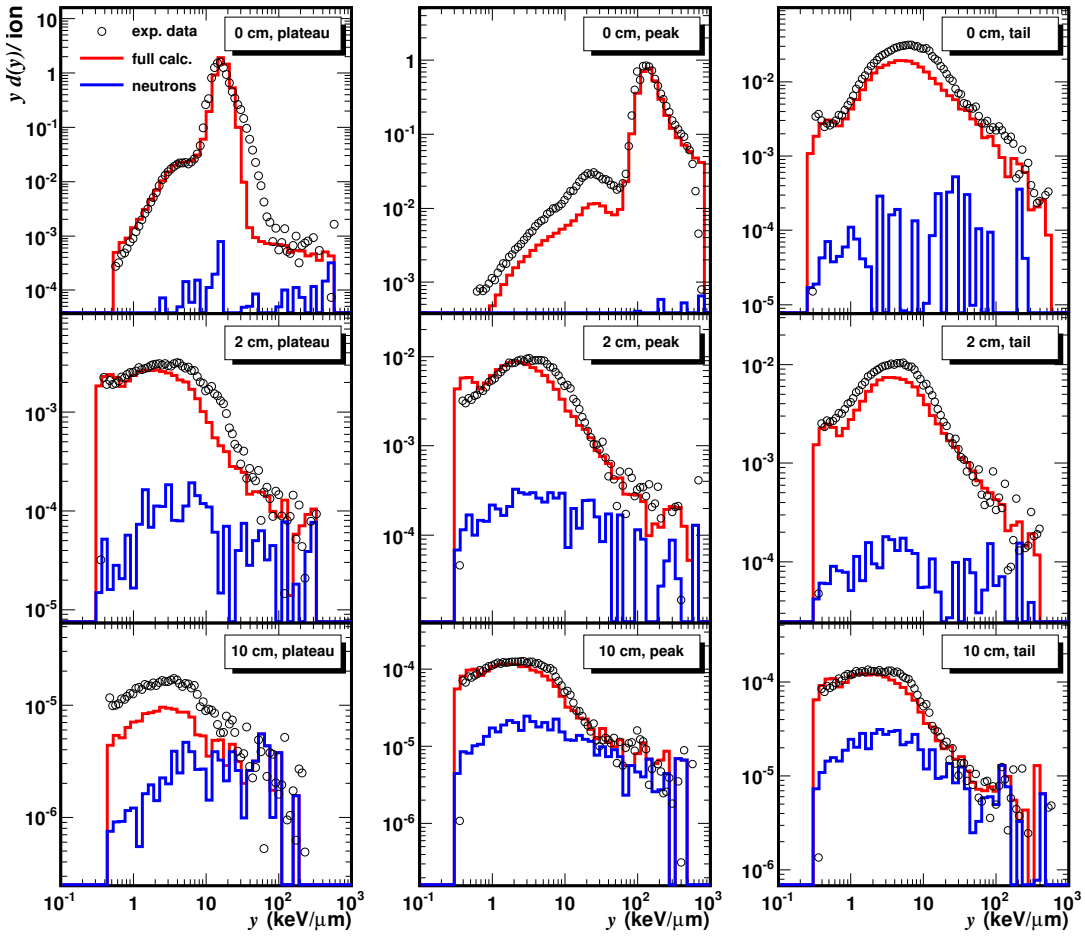

Figure 4.9: Contribution of secondary neutrons to the microdosimetry spectra in the water phantom irradiated by 300 MeV/u ^{12}C nuclei calculated with MCHIT. Simulations were performed with G4QMD for modelling of nuclear reactions. Circles represent experimental data [23].

make it possible to estimate the energy deposition due to interactions of neutrons. This is performed in two steps. Firstly, the energy deposition and lineal energy spectra are calculated taking into account all relevant physics processes, including production of secondary neutrons and their interactions with the phantom and TEPC. Secondly, calculations are performed for the same set-up including neutron production, but neglecting secondary interactions of neutrons. Thus, the difference between these two simulations provides the neutron contributions to the dose and $yd(y)$ distributions. The absolute and relative doses from neutrons obtained by MCHIT following this procedure are given in Table 4.6. They can be compared with the values of the total dose delivered by all particles as reported by Martino *et al.* [23] and calculated with MCHIT. One can also apply the correction to the experimental values in order to obtain a realistic number of TEPC events per beam particle as discussed in Section 4.3.2. As seen from Table 4.6, the corrected values of the total dose agree better with MCHIT results.

The contribution from secondary neutrons to the microdosimetric spectra is shown in Fig. 4.9. As seen, the relative neutron contribution increases with the

Table 4.6: Total dose, dose due to secondary neutrons and the relative neutron contribution to the dose in the water phantom irradiated by 300 MeV/u ^{12}C pencil-like beam. The column "per ion" contains the data by Martino *et al.* [23] multiplied by a factor of 0.844 for consistency with the calculated number of events in the TEPC at "0 cm, plateau", see Section 4.3.2.

TEPC's position notation	Total dose (nGy/ion)			Neutrons' dose (MCHIT)	
	GSI experiment		MCHIT	(nGy/ion)	%
	Martino *et al.*	per ion			
0 cm, plateau	30.6	25.8	18.4	$< 5.0 \cdot 10^{-3}$	< 0.03
0 cm, peak	93.4	78.8	80.6	$< 5.0 \cdot 10^{-2}$	< 0.06
0 cm, tail	$2.74 \cdot 10^{-1}$	$2.31 \cdot 10^{-1}$	$1.88 \cdot 10^{-1}$	$1.1 \cdot 10^{-3}$	0.6
2 cm, plateau	$1.68 \cdot 10^{-2}$	$1.42 \cdot 10^{-2}$	$1.41 \cdot 10^{-2}$	$7.8 \cdot 10^{-4}$	5.5
2 cm, peak	$5.04 \cdot 10^{-2}$	$4.25 \cdot 10^{-2}$	$4.52 \cdot 10^{-2}$	$2.0 \cdot 10^{-3}$	4.4
2 cm, tail	$6.42 \cdot 10^{-2}$	$5.42 \cdot 10^{-2}$	$5.56 \cdot 10^{-2}$	$1.6 \cdot 10^{-3}$	2.8
10 cm, plateau	$1.20 \cdot 10^{-4}$	$1.01 \cdot 10^{-4}$	$1.05 \cdot 10^{-4}$	$5.0 \cdot 10^{-5}$	47
10 cm, peak	$6.25 \cdot 10^{-4}$	$5.28 \cdot 10^{-4}$	$6.52 \cdot 10^{-4}$	$1.5 \cdot 10^{-4}$	23
10 cm, tail	$6.44 \cdot 10^{-4}$	$5.44 \cdot 10^{-4}$	$6.81 \cdot 10^{-4}$	$1.8 \cdot 10^{-4}$	26

distance from the beam axis. The neutron contribution at 10 cm radius increases from $\sim 25\,\%$ in the forward direction to $\sim 50\,\%$ in the backward direction. These results can not be directly compared to those of Endo *et al.* [109] as they correspond to different TEPC position and beam profiles. Nonetheless, the observed trend of increasing neutron contribution with respect to the distance from the primary beam is in agreement with their experimental findings. One should keep in mind, however, that the absolute doses are very small in these regions.

Conclusions

We applied the MCHIT model to calculations of microdosimetric quantities characterizing the radiation effects of accelerated nucleons and nuclei. The results of this study were published in Ref. [58]. The results of the calculations are compared with recent experimental data [23] obtained with a therapeutic 300 MeV/u ^{12}C beam and with microdosimetry data collected with quasi-monoenergetic neutrons [98]. To the best of our knowledge the present study is the first one which uses the GEANT4 toolkit for calculating microdosimetric quantities by a detailed modelling of TEPCs located in a phantom both inside and outside of a therapeutic ^{12}C beam. The in-field and out-of-field y-distributions are obtained in a consistent approach and the contributions of secondary neutrons to out-of-field doses are evaluated. Our computational methods can be useful to assess the biological effects of complex radiation fields from therapeutic ion beams, including effects of secondary neutrons produced in carbon-ion therapy [105].

Since a TEPC placed in a water phantom irradiated by nuclear beam inevitably changes the amount of material which is traversed by particles, the radiation field is distorted in the presence of the detector. The TEPC geometry was thoroughly implemented in the Monte Carlo simulations performed in this investigation with the MCHIT model. Realistic models from GEANT4 toolkit were used to describe particles propagation and energy deposition in non-uniform medium. This allowed us to obtain a good agreement between calculated and measured microdosimetric quantities for different detector positions inside the water phantom irradiated by the pencil-like beam of 300 MeV/u ^{12}C nuclei. Our main conclusions are as follows:

- The MCHIT model is able to describe the spatial distribution of the total dose in the water phantom despite of six orders of magnitude decrease of dose with increasing distance from the beam axis.
- The contributions of δ-electrons on the energy deposited to the TEPC varies at different detector locations in the water phantom. The propagation of energetic beam nuclei through a TEPC is accompanied by production of energetic δ-electrons, which may escape the sensitive volume, thus reducing the deposited energy. This effect is less important far from the beam axis for the detectors impacted only by secondary nucleons, as they produce low-energy electrons with small ranges.
- Contributions of primary beam nuclei and secondary fragments can be distinguished in the calculated and measured microdosimetric spectra on the beam axis.
- Proper modelling of nuclear fragmentation reactions is crucial for describing microdosimetric distributions both on the beam axis and far from the beam. The models for fast stage of nuclear reactions of GEANT4, namely G4QMD and G4BIC, are equally suitable for describing general features of the microdosimetric spectra, but they both underestimate the fluxes of protons and neutrons far from the beam. This indicates the necessity of improving nucleus-nucleus collision models in calculating the angular and energy distributions of secondary nucleons and nuclear fragments.
- The values of $\bar{y}_F$ and $\bar{y}_D$ for a TEPC under direct impact of projectile nuclei are sensitive to the beam profile.
- The MCHIT model describes well the $yd(y)$ distributions measured with the TEPC inside a PMMA phantom irradiated by quasi-monoenergetic neutrons. Therefore, one can expect that the response of the same detector to secondary neutrons of comparable energy from fragmentation of ^{12}C beam is also accurately calculated.
- The contribution of secondary neutrons to the out-of-field dose from ^{12}C beams estimated from MCHIT simulations amounts to about 50 % of the total dose far from the beam. Since experimental identification of neutrons would require bulky detectors placed only outside the water phantom, such microdosimetry measurements remain the only solution to estimate the upper limits for the dose from neutrons and their radiation quality close to the target volume.

Chapter 5

RBE of Monoenergetic Ion Beams

Presently proton and ^{12}C beams are successfully used for cancer treatment [2, 7, 111, 112]. Other projectiles, *e.g.* ^{4}He and ^{7}Li, may differ in their biological action from ^{12}C nuclei, but still have beam divergence similar to ^{12}C, and thus can be considered as new treatment options [113]. Beams of protons, helium, lithium, beryllium, carbon, and neon nuclei were recently compared [25] from the point of view of their advantage to spare healthy tissues with respect to radiobiological parameters (α/β ratio) of normal and target tissues. Other authors [113, 114] studied the depth-dose and linear energy transfer (LET) distributions of protons, ^{4}He, ^{7}Li and ^{12}C in water using the Monte Carlo codes SHIELD-HIT and FLUKA, respectively.

In view of possible applications of nuclei other than carbon in cancer therapy, the quality of radiation fields created by such projectiles has to be studied. In a recent publication [54] MCHIT was applied to compare the depth-dose distributions for various projectiles propagating in water. These calculations took into account the fragmentation of projectile nuclei in collisions with nuclei of the medium. The calculated dose profiles were compared with experimental data where available. In particular, the depth-dose profiles for ^{3}He nuclei in water were studied along with the distributions of positron-emitting nuclei produced by these projectiles [53].

While the capabilities of the GEANT4 toolkit to model propagation of protons and carbon nuclei in tissue-like media were already demonstrated in several publications, see *e.g.* Refs. [64, 115, 116], much less attention was paid to simulations with other projectiles, *e.g.* ^{4}He and ^{7}Li. One may expect that due to a reduced total reaction cross section of these light projectiles, the importance of fragmentation reactions on the corresponding dose distribution will be reduced with respect to ^{12}C. On the other hand one can note, that while boron or beryllium nuclei are frequently produced by ^{12}C with their Z^2 close to the projectile nucleus, ^{4}He usually fragments into a proton, a neutron and a deuteron resulting in a rapid drop of Z^2. This indicates that in addition to the known reduction of the total fragmentation cross section with the decrease of the projectile mass, the composition of secondary fragments has also to be taken into account. In turn, this will lead to different biological properties of such beams.

As demonstrated in Chapter 4, MCHIT describes well microdosimetry spectra for neutron and carbon-ion beams [58]. Here we present Monte Carlo calculations of microdosimetry distributions for proton, ^{4}He, ^{7}Li and ^{12}C beams in water and compare results with experimental data. The obtained microdosimetry spectra are

used to estimate the RBE of these nuclei both on the beam axis and away from it. Differences in the physical and biological properties of these therapeutic beams are discussed. Results presented in this chapter were published in Ref. [60].

5.1 Modelling experimental set-up

Microdosimetry data for light ions from two experiments were selected for this study. In the first experiment [22], microdosimetry spectra for 160 MeV proton and 150 MeV/u helium beams were measured at HIMAC/NIRS, Japan. The Bragg peaks in water for such proton and helium projectiles are located at the depth of ~ 175.6 and ~ 158 mm, respectively. A wall-less TEPC emulating a tissue volume of 0.72 µm in diameter was employed along with a range shifter for energy degradation. The modelling of the wall-less TEPC in MCHIT is discussed in Section 2.3.1. Microdosimetry spectra at various beam energies were measured at NIRS by changing the thickness of the range shifter. The range shifter is simulated as a water layer in front of the detector device. The uncertainties in the water equivalent thickness of the range shifter and beam elements in the experimental set-up were not reported. Taking into account that the precise dimension and material properties of the range shifter are unknown, and also that the calculation of water-equivalent thickness is influenced by uncertainties in the stopping power of ions, in our simulations we decided to adjust the thickness of the range shifter in order to reproduce the position of the main peak in microdosimetry spectra which is associated with primary beam particles traversing the detector. The water equivalent thickness used in the simulations are smaller than the estimated value [22] for the experimental set-up by about 3 % and 0.8 % for proton and helium beams, respectively. A total of 4×10^7 primary ions were simulated for each microdosimetry spectrum. The experimental data were reported as $yf(y)/\bar{y}_F$ distributions.

In the second experiment [23], microdosimetry measurements for 185 MeV/u ^{7}Li and 300 MeV/u ^{12}C beams were performed at SIS18/GSI, Germany at several positions inside a water phantom. A compact walled TEPC was employed to measure microdosimetry spectra for a tissue equivalent volume of 2.7 µm in diameter. The total water equivalent thickness of the PMMA wall of the water phantom and beamline elements used in experiment [23] amounts to 25.1 mm. Similar to the modelling of measurements for ^{1}H and ^{4}He beams described above, the TEPC positions were adjusted in order to reproduce the position of the main peak in the spectra when the TEPCs were placed on the axis in the vicinity of the Bragg peak of ^{7}Li and ^{12}C beams. The shift of the TEPC for the carbon beam (2 mm deeper position which corresponds to 1 % of the range of carbon ion) was discussed in Section 4.1. As for ^{7}Li beam, the microdosimetry spectrum measured for the TEPC located at the Bragg peak could be only reproduced by calculations if the TEPC is further shifted to deeper position by 6.7 mm. One must notice that our simulations have shown that the range in the water phantom for 185 MeV/u ^{7}Li beam is 5 mm deeper than the one for the 300 MeV/u ^{12}C beam. However, while it was reported [23] that the specific energies for the carbon and lithium beams in the experimental set-up were chosen such that the residual range in the water phantom is the same for both ions. The simulated geometry of the walled TEPC is presented in Section 2.3.1. A total

of 10^7 histories of primary ions and all their secondary particles were simulated for each microdosimetry spectrum. As explained in Section 4.1, each walled TEPC detector placed far from the beam axis was represented in simulations by a number of virtual TEPCs placed on a ring at the same depth. Due to this special arrangement of virtual TEPC detectors, the counting rate of events per primary track is significantly increased in each physical TEPC [58]. The experimental data were reported as $yd(y)$ distributions normalized to the number of incoming primary ions.

5.2 Microdosimetry simulations

5.2.1 Contribution of secondary fragments

The role of nuclear reactions to attenuate the intensity of ^{1}H, ^{4}He, ^{7}Li and ^{12}C beam particles while they propagate in water can be well understood from Fig. 5.1. The energy per projectile nucleon was taken as 152.6 MeV for ^{1}H, 152 MeV for ^{4}He, 176 MeV for ^{7}Li and 290 MeV for ^{12}C. With this choice of energies all the beams have the Bragg peaks at 161.6 mm depth in water. In Fig. 5.1 the fractions of surviving beam nuclei at certain depth (bottom) are plotted together with the corresponding depth-dose curves (top). As one can see, $\sim 50\,\%$ of ^{7}Li and ^{12}C beam nuclei are lost before they reach the depth of the Bragg peak, where they finally stop. Nuclear reactions are less frequent for ^{1}H and ^{4}He beams, as only $\sim 20\,\%$ of protons and $\sim 30\,\%$ of alphas participate in nuclear reactions before they stop.

In the experiments of Tsuda *et al.* [22] the ^{1}H and ^{4}He projectiles entered the TEPC after traversing 150–170 mm of water when their energies were reduced to 17–38 MeV/u. As seen from Fig. 5.1, this corresponds to a TEPC placed close to the Bragg peak. Even at this deep location $\sim$70–80 % of beam protons and alphas reached the TEPC without participating in nuclear reactions. Therefore, a relatively small contribution of secondary fragments to microdosimetry spectra is expected for ^{1}H and ^{4}He beams. Nevertheless, as demonstrated below, for ^{4}He beam the contributions of specific secondary fragments to microdosimetry spectra can still be identified. The contributions of secondary fragments to microdosimetry spectra obtained with ^{7}Li and ^{12}C [23] are expected to be much larger as compared with ^{1}H and ^{4}He beams. Indeed, as can be estimated from Fig. 5.1, a noticeable number of secondary fragments of ^{7}Li and ^{12}C traverse TEPCs placed at the depth of ~ 50 mm and especially near the Bragg peak in the measurements by Martino *et al.* [23].

The LETs of protons and ions vary significantly in the range of the kinetic energies used for radiation therapy. The lineal energy y, which is measured by the TEPC, serves as an estimation of LET and its frequency distribution includes contributions from various particles traversing the detector. However, since different particles may contribute to similar or overlapping domains of y, such contributions can not be easily disentangled in experiment [9], unless a complicated procedure to identify the charges of fragments is involved. Alternatively, specific contributions from certain particles can be scored and identified in calculations using the Monte Carlo method. Once the validity of Monte Carlo modelling is confirmed by a good agreement of calculated and measured spectrum, the contributions from specific particles can be reliably identified. The study of microdosimetry spectra collected far from the beam

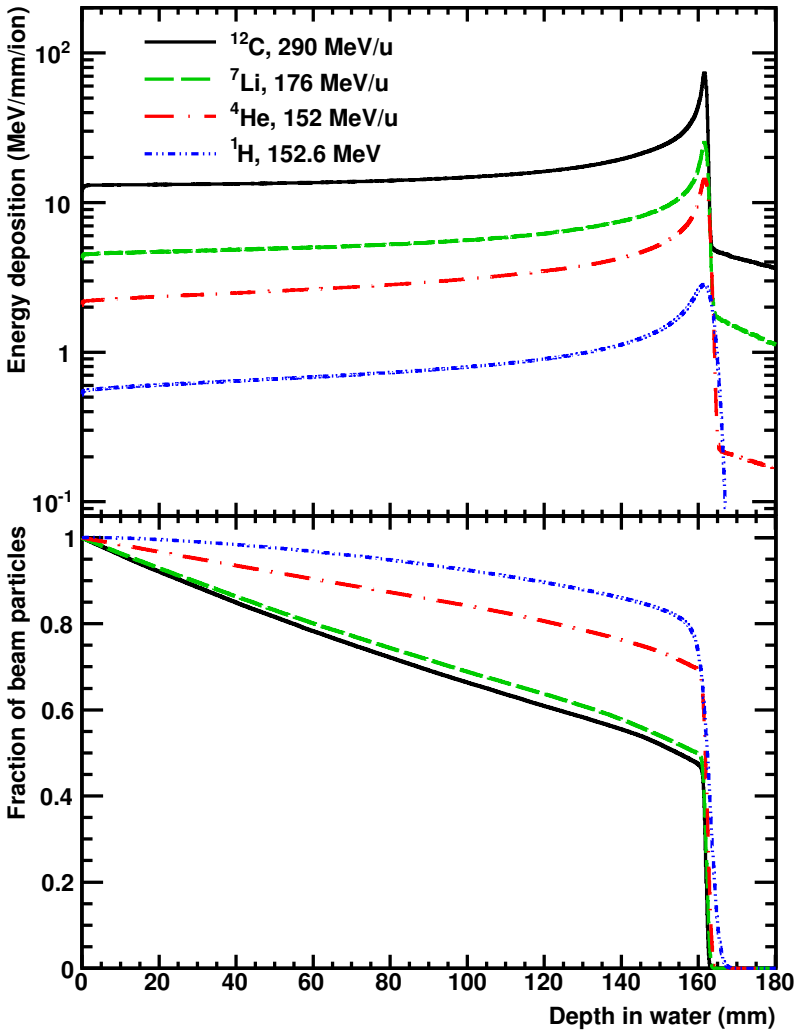

Figure 5.1: Calculated depth-dose distributions in water for ^{1}H, ^{4}He, ^{7}Li and ^{12}C beams considered in the present study (top panel) and the attenuation factor for these beams due to nuclear reactions (bottom panel).

helps to evaluate the accuracy of nuclear fragmentation models since such spectra are built entirely by secondary fragments. At the same time, the Monte Carlo modelling of microdosimetry spectra opens the possibility to understand the quality of radiation in mixed radiation fields.

5.2.2 Beam of ^{1}H in water

The simulated microdosimetry spectrum for a proton beam traversing a 163 mm range shifter made of water is shown in Fig. 5.2 along with experimental data [22]. This spectrum corresponds to the TEPC position at $\sim$13 mm before the Bragg peak. Similar results, but for a TEPC placed closer to the Bragg peak are shown in Fig. 5.3. In the latter case the TEPC is traversed by less energetic protons which have a higher LET. This is confirmed by the shift of the maximum of the microdosimetry spectra to larger y, which can be seen by comparing Fig. 5.3 and Fig. 5.2. One can clearly see that the model systematically underestimates events with very low

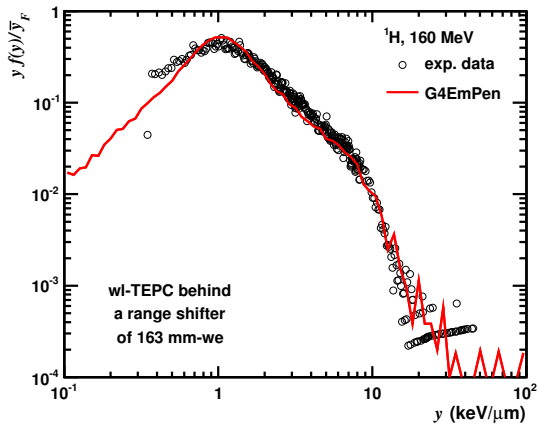

Figure 5.2: Microdosimetry spectrum calculated with G4EmPen behind the range shifter (163 mm-we) for a 160 MeV proton beam. Circles represent experimental data [22] corresponding to the estimated average proton energy of 38 MeV at the entrance to TEPC.

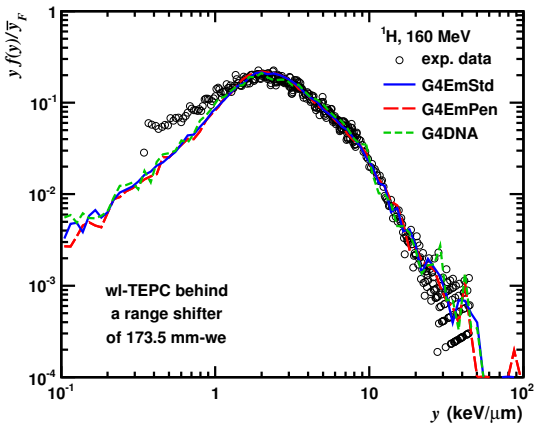

Figure 5.3: Microdosimetry spectra calculated with G4EmPen, G4EmStd and G4DNA behind the range shifter (173.5 mm-we) for a 160 MeV proton beam. Circles represent experimental data [22] corresponding to the estimated average proton energy of 20 MeV at the entrance to TEPC.

lineal energy ($y < 1$ keV/μm) in all simulations with the wall-less TEPC. In order to investigate whether this is related to the limitation for production of δ-electrons with G4EmStd and G4EmPen, we carried out a simulation with G4DNA with results also presented in Fig. 5.3. The distribution of particle energies downstream of the TEPC window was first calculated with G4EmPen and then used as an input to simulations with G4DNA. The simulated gas cavity of the TEPC was replaced in G4DNA simulations by a homogeneous water-equivalent volume. As shown in Fig. 5.3, G4EmPen and G4DNA provide statistically equivalent results even though the simulation with G4EmPen accounts for a detailed geometric description of the detector, while G4DNA works only with an equivalent cylindrical water volume. Since there are no low-energy limits for production of δ-electrons in simulations with G4DNA, one should conclude that the deficit of events with very low y is not related to limitations of electron transport.

As seen from Fig. 5.3, the microdosimetric spectrum of protons calculated for the macroscopic-size TEPC agree well with the microdosimetric spectrum calculated for the equivalent microscopic volume of water with the G4DNA physics list. This confirms the basic assumption of the microdosimetry technique and justifies the calculation of microdosimetric spectra using the continuous slowing-down approximation.

5.2.3 Beam of ^{4}He in water

Microdosimetry spectra calculated for helium beams with three physics lists, namely G4EmStd, G4EmPen and G4EmPen+IonGas are presented in Fig. 5.4. G4EmStd and G4EmPen give statistically equivalent results which, however, both slightly deviate from the experimental spectrum [22] at low y and also close to the

maximum. Once the models for the gas ionization by ions are involved in calculations in the G4EmPen+IonGas physics list, the agreement with the measured spectrum for $y > 1$ keV/µm is improved, in particular, close to its maximum. The shape of mi-

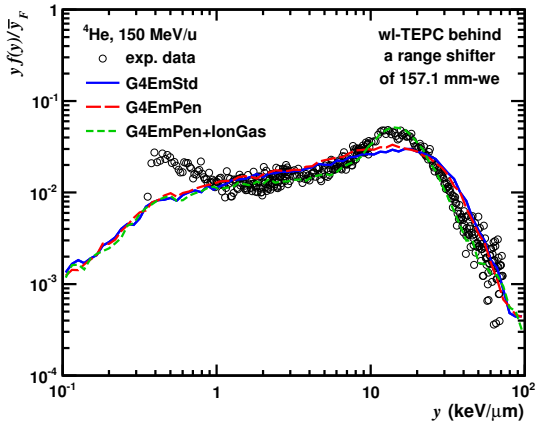

Figure 5.4: Microdosimetry spectrum behind a range shifter (157.1 mm-w.e.) for a 150 MeV/u ^{4}He beam calculated with G4EmStd, G4EmPen and G4EmPen+IonGas. Circles represent experimental data [22] corresponding to the estimated average ^{4}He energy of 17 MeV/u at the entrance to TEPC.

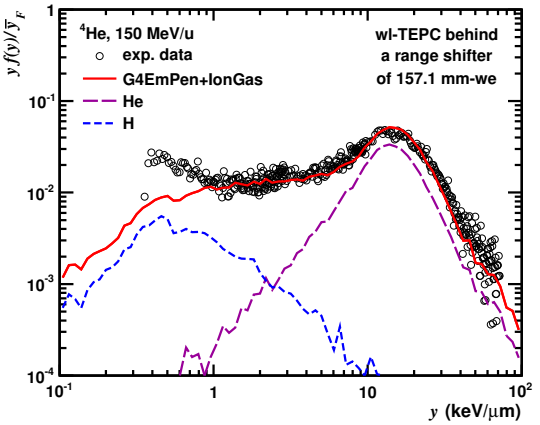

Figure 5.5: Same as in Fig. 5.4, but with microdosimetry spectrum calculated only with G4EmPen+IonGas. Specific contributions from hydrogen and helium nuclei are shown separately as explained in the legend of the figure.

crodosimetry spectra for helium beams differs from the one for proton beams. Two distinct peaks are observed in the spectra for ^{4}He nuclei. As can be seen from the decomposition of the calculated spectra into contributions of hydrogen and helium nuclei shown in Fig. 5.5, these two prominent peaks are due to hydrogen fragments for events with low y and due to helium nuclei for events with high y. A certain evolution of the position of the helium peak can be observed in Figs. 5.5 to 5.7 as the energy per nucleon of ^{4}He increases. While the projectile energy increases, the helium peak shifts to lower y. At the same time there are no noticeable changes in the peak position of hydrogen fragments. This can be explained by the fact that produced hydrogen fragments have an energy spectrum which depends weakly on the beam energy. One can see that the yields of events with $y < 1$ keV/µm in the spectra for the ^{4}He beam are underestimated by the MCHIT model, but the reason for this effect may be different as compared to the case of ^{1}H beam. The events with $y < 1$ keV/µm in the spectra calculated for the ^{4}He beam are mainly due to secondary hydrogen fragments, see Figs. 5.5 to 5.7, and secondary electrons (not shown). This means that the observed effect could also be related to an inaccuracy of the Light Ion Binary Cascade model (G4BIC) used to simulate the nucleus-nucleus collision of ^{4}He ions.

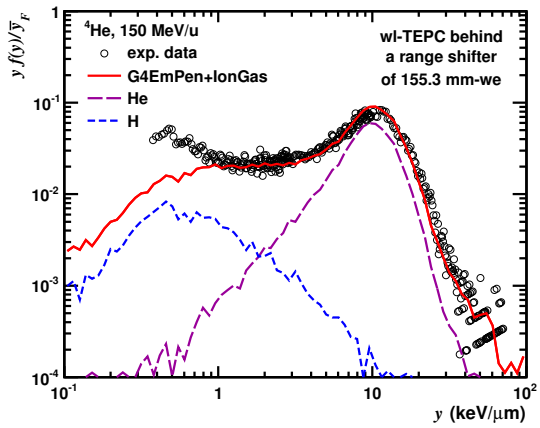

Figure 5.6: Microdosimetry spectrum behind a range shifter (155.3 mm-we) for a 150 MeV/u helium beam. Specific contributions from hydrogen and helium nuclei are shown separately as explained in the legend of the figure. Circles represent experimental data [22] corresponding to the estimated average ^{4}He energy of 22 MeV/u at the entrance to TEPC.

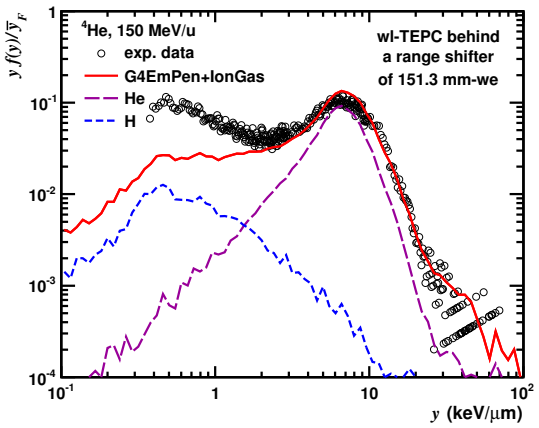

Figure 5.7: The same as Fig. 5.6 but for a 151.3 mm-we range shifter. Circles represent experimental data [22] corresponding to the estimated average ^{4}He energy of 32 MeV/u at the entrance to TEPC.

5.2.4 Beam of ^{7}Li in water

Calculated and measured [23] microdosimetry spectra for lithium beams at nine positions inside a water phantom are shown in Fig. 5.8. The centre of the TEPC was placed at three positions at the depth of 58.8, 185.8 and 283.8 mm (centres of the gas chamber) corresponding to the plateau, Bragg peak and tail of the depth-dose distribution on the beam axis and also at 2 and 10 cm radial distance from the axis. The microdosimetry spectra on the beam axis typically characterize the radiation field in the centre or in front of the target tumour volume during radiation therapy.

In addition to the total spectra the contributions from specific nuclei, H, He or Li, are also shown in Fig. 5.8. Prominent peaks of primary ^{7}Li nuclei at $y = 5$ keV/μm and $y = 50$ keV/μm are seen in the $yd(y)$ distributions calculated on the beam axis at the plateau and Bragg peak, respectively. These peaks are expected to provide the major therapeutic effect. They are superimposed on broader contributions from hydrogen and helium fragments located before and after the main ^{7}Li peak. All events registered at the Bragg peak position due to secondary nuclei are characterized by lower y compared to the events due to ^{7}Li nuclei. This relation between y of beam nuclei and their fragments also holds at the "0 cm, plateau" position. However, in the latter case there exists also a contribution of He nuclei produced in the fragmentation of target nuclei. Since such fragments are slower compared to ^{7}Li projectiles and their fragments, such target fragments are responsible for events with high y values, which are seen right to the main peak in the first panel of Fig. 5.8.

The shapes and positions of the calculated and measured ^{7}Li peaks essentially differ at "0 cm, plateau". The calculated peak is sharper as compared to the data

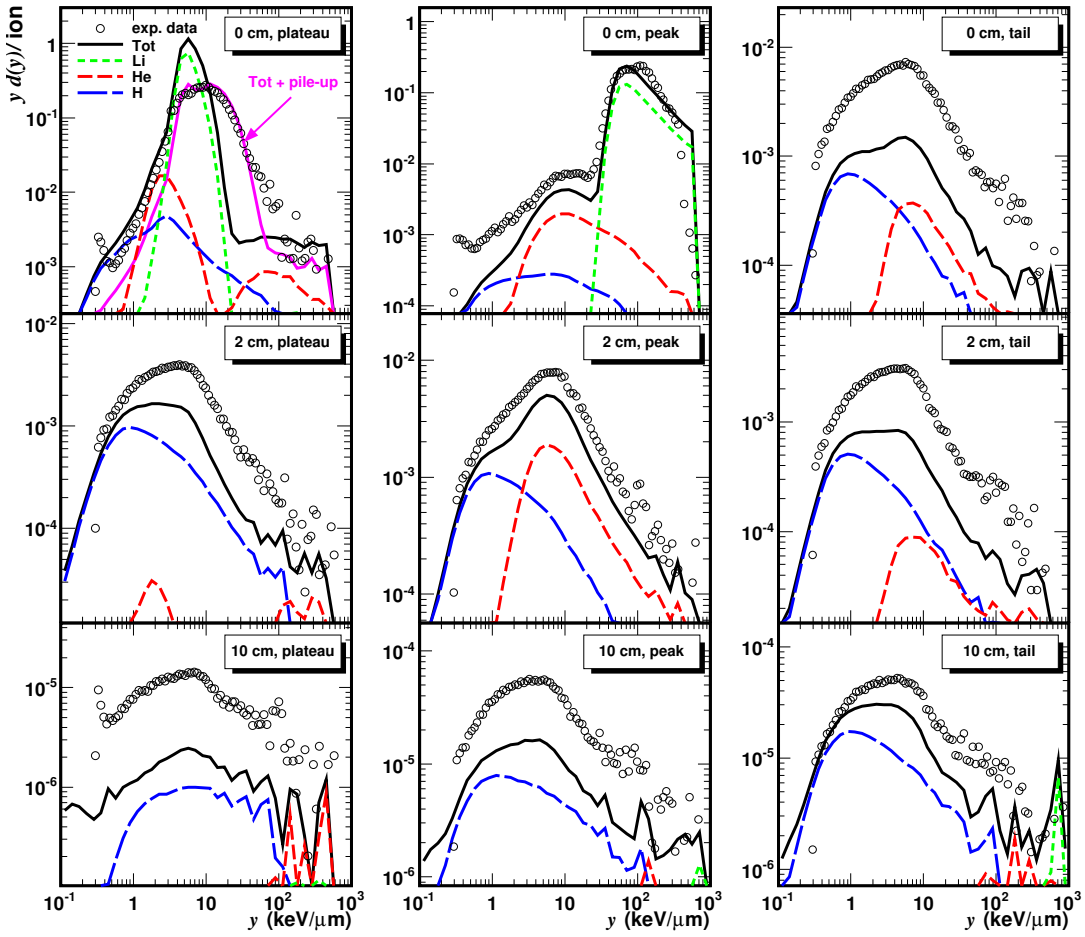

Figure 5.8: Microdosimetry spectra in water phantom irradiated by 185 MeV/u ^{7}Li nuclei calculated with MCHIT using G4BIC and G4EmPen+IonGas. Contributions from nuclear fragments of a given charge are shown by various lines as explained in the legend. The distribution at "0 cm, plateau" labelled as "Tot + pile-up" was obtained with accounting for pile-up events. Circles represent experimental data [23].

and centred at smaller y. The $\bar{y}_D$ calculated with MCHIT equals to 7.32 keV/μm, which is smaller than the value 13.6 keV/μm estimated from the measured spectrum. In addition, the average number of events per beam particle in the TEPC placed at "0 cm, plateau" is calculated by MCHIT as $\bar{N}_c = 0.94$ due to a slight attenuation of the beam after its entrance to the water phantom. According to the normalization of the measured spectra the average number of TEPC events per beam particle in the experiment is only $\bar{N}_e = 0.48$. All these observations led us to the conclusion that some of the high-y events detected at "0 cm, plateau" were due to two or more ^{7}Li nuclei traversing the TEPC within a short time interval and thus appeared as a single event. Such pile-up events are characterized by an elevated energy deposition to the detector. Since all beam particle histories are modelled by MCHIT independently of each other, pile-up events are impossible in the present simulation. Therefore, providing that the difference between $\bar{N}_c$ and $\bar{N}_e$ is only due to the pile-up effect, the probability of an event induced by multiple ^{7}Li at "0 cm, plateau" can be estimated

as

$$P_{mult} = \frac{\bar{N}_c - \bar{N}_e}{\bar{N}_c} = 0.49 \ . \tag{5.1}$$

One can define the pile-up probability P_{pu} as a probability of a single TEPC event induced by a pair of ^{7}Li nuclei. Since multiple events are represented by double, triple etc. coincidence events,

$$P_{mult} = P_{pu} + P_{pu}^2 + P_{pu}^3 + \cdots = \frac{1}{1 - P_{pu}} - 1 = \frac{P_{pu}}{1 - P_{pu}} \ , \tag{5.2}$$

resulting in

$$P_{pu} = \frac{P_{mult}}{1 + P_{mult}} = 0.33 \ . \tag{5.3}$$

In order to estimate the contribution of pile-up events to microdosimetry spectra a Monte Carlo method was implemented. The $f(y)$ distribution calculated by MCHIT at "0 cm, plateau" was used to sample independent y events. For each event, the sampled y value is piled-up with the y value of the previous event with a probability P_{pu}. The resulting $yd(y)$ distribution is shown in Fig. 5.8 labelled as "Tot + pile-up". As seen, the accounting for pile-up events restores the agreement between calculated and experimental $yd(y)$ distributions.

Beam nuclei do not reach the TEPC at "0 cm, tail" and other six positions, where the spectra are built mainly by secondary H and He fragments and δ-electrons. Also target fragments may eventually contribute with large y events as can be seen at "10 cm, tail" but one should keep in mind the poor statistic for such events for TEPC positions at 10 cm away from beam axis. The general shapes of calculated microdosimetry spectra are found to be similar to the shapes of measured spectra. However, the spectra at the tail, 2 and 10 cm away from the beam axis are underestimated by MCHIT. Since at all these positions (excluding "2 cm, peak") the spectra are mostly formed by hydrogen-like fragments, this indicates that the yields of proton, deuterons and tritons may be underestimated by the Light Ion Binary Cascade model (G4BIC) used to simulate fragmentation of ^{7}Li projectiles. For the TEPC position "2 cm, peak" this deficiency may also be connected to some underestimation of the yield of helium fragments, as the cascade model neglects the cluster structure of ^{7}Li and treats all intra-nuclear nucleons as uncorrelated. It is expected that accounting for the cluster structure of light nuclei would enhance the emission of alpha particles.

5.2.5 Beam of ^{12}C in water

Calculated and measured [23] microdosimetry spectra for carbon beams at nine positions inside a water phantom are shown in Fig. 5.9. The exact TEPC positions used in simulations are given in Section 4.1. A shoulder in the spectrum at low y at "0 cm, plateau" position is due to the contribution of several projectile fragments. Similar to ^{7}Li beam, the events with $y > 100$ keV/µm are due to protons and alphas emitted by target nuclei. Since these target fragments are much slower than the projectile fragments, they provide higher y values at this TEPC position with respect to a sharp peak due to primary ^{12}C nuclei. Apart from the underestimation of

events with $40 < y < 100\,\mathrm{keV}/\mu\mathrm{m}$, the spectrum measured at the entry to the water phantom on the beam axis is well reproduced by MCHIT. The peak of primary ^{12}C nuclei also dominates at the TEPC position "0 cm, peak" on the beam axis close to the Bragg peak. The agreement with the measured spectrum is good there in general with the exception of a slight underestimation of the contribution of projectile fragments seen at lower y before the main peak.

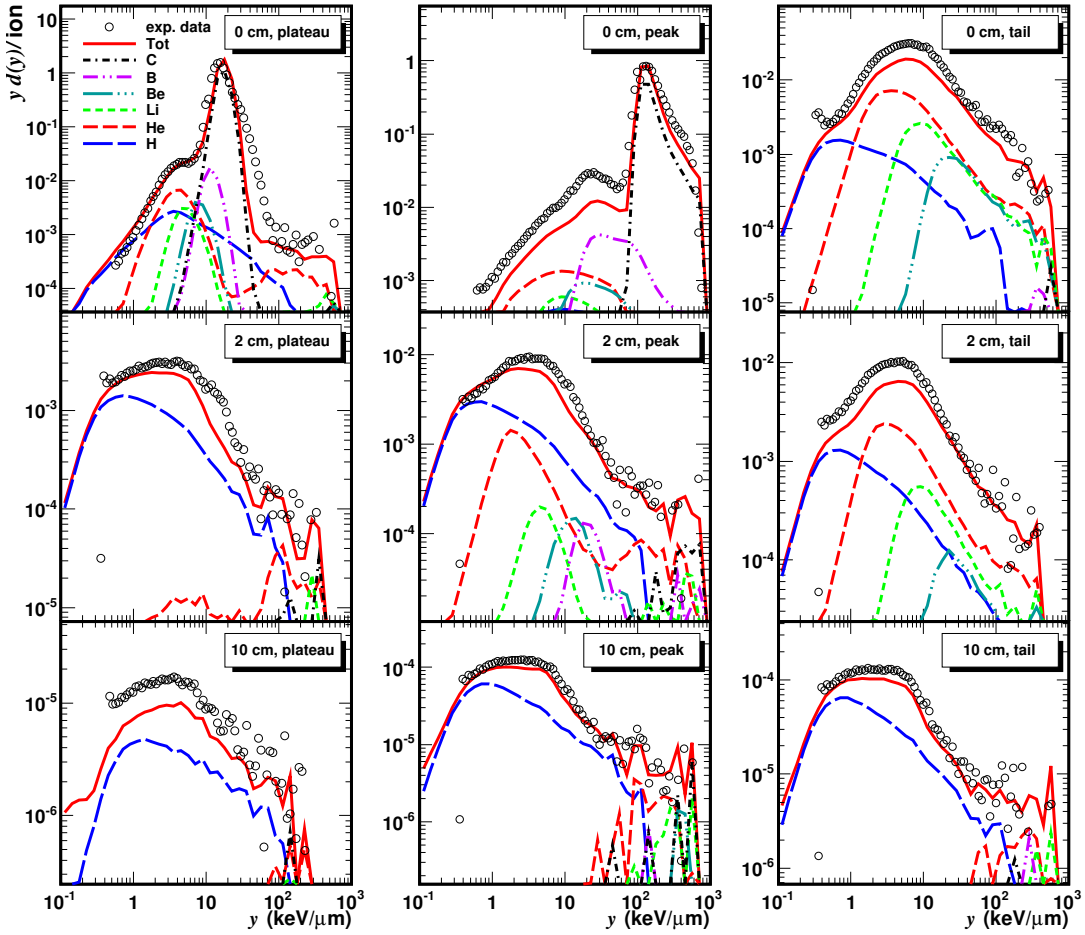

Figure 5.9: Microdosimetry spectra in water phantom irradiated by 300 MeV/u ^{12}C nuclei calculated with MCHIT using G4QMD and G4EmPen+IonGas. Contributions from nuclear fragments of a given charge are shown by various lines as explained in the legend. Circles represent experimental data [23].

The spectra at "0 cm, tail", "2 cm, peak" and "2 cm, tail" are built from overlapping contributions from various projectile fragments: H, He, Li and Be. Among these three positions a noticeable contribution from boron nuclei is predicted only at "2 cm, peak". As follows from the calculations, the maxima of the contributions from H, He, Li, Be and B are ordered according to Z^2 of the corresponding nuclei: more heavy fragments contribute with larger y. The contributions from He nuclei are remarkable. The spectra at these three positions are also underestimated, as in the case of ^{7}Li beam. The quantitative agreement between calculations and measurements for ^{12}C beam is much better compared to ^{7}Li beam, but still the deviations of the calculated spectra from measured ones can be attributed to the un-

derestimation of He fragments. The other four spectra, namely, at "2 cm, plateau", "10 cm, plateau", "10 cm, peak" and "10 cm, tail" are mostly composed from the contributions of hydrogen nuclei produced in fragmentation of ^{12}C. They are also slightly underestimated by MCHIT. Some traces of the contributions from fragments of the target nuclei are also seen at these four positions far from the ^{12}C beam. Such target fragments are scarcely produced in nuclear reactions induced by energetic secondary protons and neutrons.

5.3 Estimation of RBE and dose profiles

The modified Microdosimetric-Kinetic model (MKM) (see Section 1.3.2) is used in the present study to estimate the RBE of proton, ^{4}He, ^{7}Li and ^{12}C beams for human salivary gland (HSG) cells. Firstly, microdosimetric spectra were calculated by means of the MCHIT model placing the walled TEPC behind a range shifter made of water. The thickness of the range shifter was varied in order to calculate the microdosimetry spectra at different water-equivalent depths. The pressure of the TE gas was set to simulate a tissue sphere of 1 μm in diameter and the detector was irradiated by a broad beam. This set-up mimics the experimental conditions used by Kase *et al.* [3] in measurements of the saturation-corrected dose-mean lineal energy y^* with same TEPC and survival fraction of HSG cells for a 290 MeV/u ^{12}C beam. The value of the saturation parameter $y_0 = 150$ keV/μm assumed in the experiment is also used in this study. In addition, the following parameters for HSG cells were taken from Ref. [3]: $D_{x,10} = 5$ Gy as the 10 % survival dose of the reference radiation (200 kVp x-rays), $\alpha_0 = 0.13$ Gy^{-1}, $\beta = 0.05$ Gy^{-2}, $\rho = 1$ g/cm^3 and $r_d = 0.42$ μm. RBE$_{10}$ values for HSG cells irradiated by carbon beams were estimated according to Eq. (1.17) with the experimental and simulated values of y^* and used for the MCHIT validation. RBE$_{10}$ for proton, helium and lithium were also calculated for the sake of comparison. In order to evaluate the biological effectiveness away from the beam axis, a second set-up was devised. In this case the TEPC was placed inside a water phantom at depths close to the Bragg peak and 2 cm away from the axis of a pencil-like beam. A large number ($\sim 10^7$) of beam particle histories were simulated to ensure that statistical fluctuations of the calculated y^* are negligible in all set-up configurations.

5.3.1 RBE and biological dose profiles for ^{1}H, ^{4}He, ^{7}Li and ^{12}C beams

Using calculated microdosimetry spectra we estimate now the biological effectiveness of ^{1}H, ^{4}He, ^{7}Li and ^{12}C nuclei. For the sake of comparison we have chosen their beam energies such that they lead to similar ranges in water. The microdosimetry spectra were calculated at several positions along the beams axes. The corresponding energy deposition profiles (bin size of 0.1 mm) are shown in logarithmic and linear scales in the top panels of Figs. 5.1 and 5.10, respectively.

As demonstrated in the previous sections, the microdosimetric spectra depend strongly on depth and radial distance from the beam axis. Such variation in the energy deposition pattern leads to very different biological effects. The values of

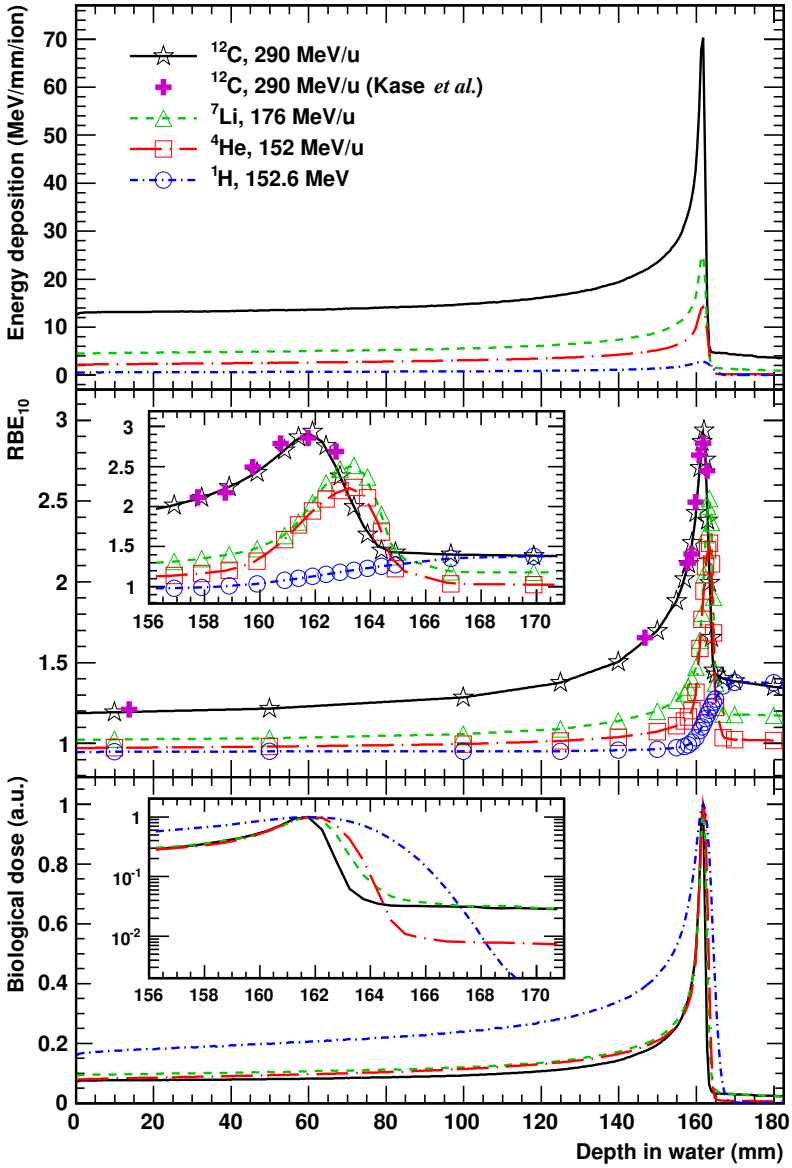

Figure 5.10: Calculated energy deposition profile per ion beam in water for ^{1}H, ^{4}He, ^{7}Li and ^{12}C beams with Bragg peak at 161.6 mm (top panel), estimated RBE$_{10}$ for HSG cells (middle panel) and biological dose (bottom panel). The cross symbols (✚) show the RBE$_{10}$ calculated from experimental values of y^* [3] while other symbols present results obtained with MCHIT and modified MKM. The biological doses for all ions were rescaled by respective values at the Bragg peak.

RBE$_{10}$ estimated by means of MCHIT coupled with the modified MKM model on the beam axis as a function of depth are presented in the middle panel of Fig. 5.10 for the four ion beams. RBE$_{10}$ values for carbon beam estimated from experimental y^* data [3] are plotted in the same figure for comparison. The well-known increase of the RBE for carbon ions on their way from the plateau region to the Bragg peak seen in the experimental data is well reproduced by MCHIT+MKM. Helium and lithium ions also show favourable RBE profiles characterized by even lower values at the plateau region, with much steeper increase close to the Bragg peak and lower

RBE values in the tail. The maximum RBE_{10} values for helium, lithium and carbon ions found around the Bragg peak are 2.2, 2.5 and 2.9, respectively. At the plateau region the values are 1.0, 1.0 and 1.2, respectively. For protons, the model predicts the RBE_{10} value slightly below 1 at the entrance to the phantom and a smooth increase to 1.2 at the Bragg peak. A further increase of RBE_{10} after the peak may be related to slow secondary neutrons produced in nuclear reactions. Similar calculations were performed with the TEPC placed 2 cm away from the beam axis at the depth of the Bragg peak. At this point RBE_{10} of 1.1±0.1 was estimated from calculated microdosimetry spectra for all four ions.

The biological dose at the considered TEPC positions can now be estimated as the product of RBE and the physical dose. The results for the biological dose for different ions are shown in the bottom panel of Fig. 5.10. The curves were rescaled in order to yield the same dose at the Bragg peak. The biological dose profiles for the helium, lithium and carbon beams were found to be similar to each other. All three ions demonstrate a high ratio of the dose at the Bragg peak relative to the dose at the plateau which helps to spare healthy tissues traversed by the beam before reaching a tumour. The biological dose values at the tail of the lithium and carbon beams are found to be very similar, while the helium beam delivers a smaller dose to the tail region due to a reduced fragmentation rate. These results show that helium and lithium beams are also promising options in addition to a well-established carbon-ion cancer therapy.

Despite the fact that the depth-dose and RBE_{10} profiles shown in Fig. 5.10 look similar in shape, the relation between $\bar{y}_F$ representing LET and RBE_{10} is not trivial. The correlated pairs of values $\bar{y}_F$ and RBE_{10} are shown in Fig. 5.11 for all four considered beams. The curves demonstrate a monotonic increase of RBE_{10} with the

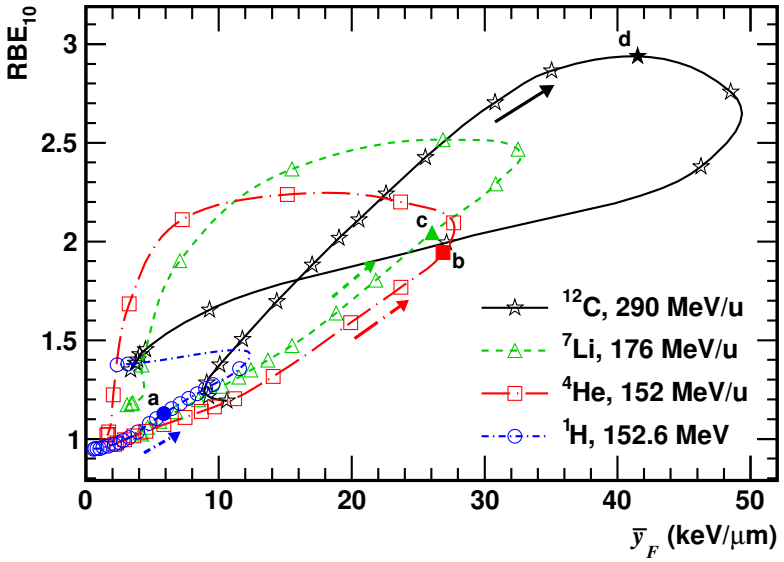

Figure 5.11: Calculated correlation between RBE_{10} and $\bar{y}_F$ for ^{1}H, ^{4}He, ^{7}Li and ^{12}C beams in water. The lines connect the values obtained for TEPCs sequentially placed along the beam axes while arrows indicate the direction for increasing depth. Full symbols indicated by letters 'a', 'b', 'c' and 'd' correspond to the values at the Bragg peak for protons, helium, lithium and carbon ions, respectively.

rise of $\bar{y}_F$ before the Bragg peak. The correlations for ^{4}He and ^{7}Li are similar to each other, but they differ from the case of ^{12}C. In the case of the carbon beam, the increase is more pronounced but RBE_{10} reaches a maximum at the Bragg peak and then slightly drops for large $\bar{y}_F$ values. This behaviour shows a kind of saturation effect. Such effect is not observed for ^{4}He and ^{7}Li. Particularly, one can see that for these two ions RBE_{10} continues to rise even when $\bar{y}_F$ values start decreasing in the tail region. Another feature of the relation between $\bar{y}_F$ and RBE_{10} is that for a given beam similar $\bar{y}_F$ values correspond to quite different RBE_{10} at the plateau and tail of the depth-dose distribution. Primary beam particles and secondary fragments which dominate, respectively, in these two regions provide rather similar $\bar{y}_F$, but their RBE_{10} differ significantly. These results confirm that $\bar{y}_F$ (LET) solely is not sufficient to characterize the biological effects of various beams.

5.3.2 Impact of beam fragmentation on RBE

Nuclear fragmentation reactions should be properly taken into account in simulations for ion-beam cancer therapy in order to reproduce the effect of lost of beam particles and build-up of secondary fragments in the energy-loss rate and resulting depth-dose profile. Besides, nuclear fragmentation leads to energy deposition to healthy tissues located behind the distal end of the Bragg peak, *i.e.*, in the tail region. Furthermore, the presence of fragments in the irradiation field change the biological effectiveness of the beam. Therefore, it is important to evaluate the impact of nuclear fragmentation reactions on the RBE of ion radiation field.

In order to estimate a limit for the impact of nuclear fragmentation on RBE a theoretical extreme case was considered. Microdosimetry spectra were calculated

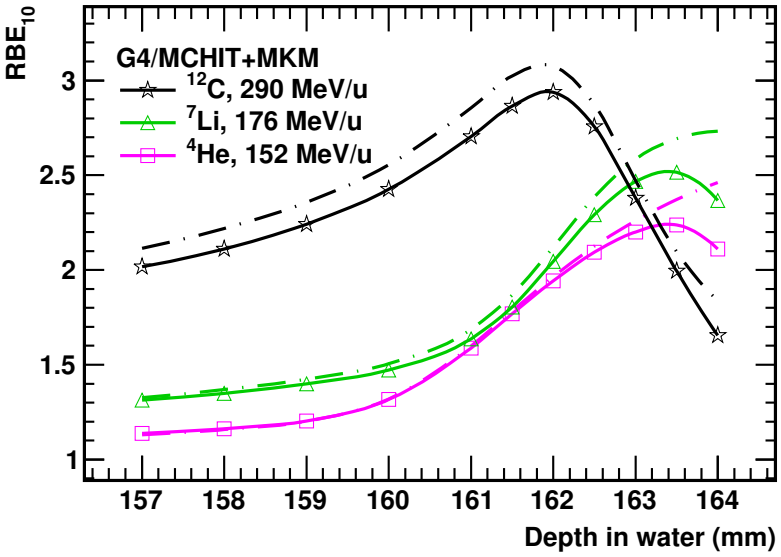

Figure 5.12: Impact of nuclear fragmentation reactions on the RBE_{10} for HSG cells after irradiation by light nuclei. Solid line present expected results calculated by MCHIT+MKM models when all interaction processes are taken into account in simulations. Dashed lines present hypothetical RBE_{10} in the absence of nuclear fragmentation of the considered beams.

by MCHIT for 152 MeV/u ^{4}He, 176 MeV/u ^{7}Li and 290 MeV/u ^{12}C ions at several depths in water neglecting any hadronic processes. RBE_{10} values for HSG cells are calculated from these spectra and compared to the values calculated above in the presence of nuclear fragmentation. The obtained RBE_{10} profiles in the vicinity of the pristine Bragg peaks are shown in Fig. 5.12. One can see that nuclear reactions reduce the RBE_{10} expected when the radiation field is composed only by primary ions. The RBE_{10} for helium and lithium is only significantly decreased at the far end of the ion range while for carbon ions the RBE_{10} values around the Bragg peak are decreased by not more than 10 %. This result shows that the loss of a primary carbon ion and yield of secondary fragments cause less biological effect for this particular end-point. Therefore, a treatment planning system for ion-beam cancer therapy that neglects the presence of fragments in the radiation field overestimates the RBE_{10}. Then, the delivered biological dose is smaller than the one prescribed undermining the treatment.

Conclusions

Our analysis of the microdosimetry spectra for light nuclei lead us to the following conclusions:

- The microdosimetry spectra of protons calculated for the macroscopic-size TEPC filled with dilute gas agree well with the microdosimetry spectra calculated for the equivalent microscopic volume of water with G4DNA physics list. In this way the basic assumption of the microdosimetry technique is fully validated by Monte Carlo simulations with MCHIT.

- Contributions of primary beam nuclei and secondary fragments to the microdosimetry spectra can be realistically evaluated by Monte Carlo simulations with MCHIT.

- A proper modelling of nuclear fragmentation reactions is crucial for describing microdosimetry spectra both on the beam axis and far from the beam. Further improvements of nuclear fragmentation models, *e.g.* with respect to production of ^{4}He nuclei, could improve the description of the microdosimetry data and, therefore, provide a better understanding of the radiation effects induced by the considered therapeutic beams.

- The MCHIT model is able to describe reasonably well the microdosimetry spectra for hydrogen and helium beams in water. Microdosimetry spectra for lithium beams are well described on the beam axis from the entrance to the Bragg peak while the spectra are underestimated far from the primary beam. It was demonstrated that in the case of TEPC directly irradiated by a ^{7}Li beam, the agreement with the experimental data can be significantly improved by taking into account the pile-up effect. This is specific to the experimental data of Ref. [23]. It is expected that similar measurements, but with lower beam current, will be not distorted by overlapping events. The spectra for carbon beam are generally well described, despite of some underestimations at positions far from the beam axis and also in the tail region.

- MCHIT coupled with the modified MKM model allowed us to estimate the RBE_{10} for proton, helium, lithium and carbon ions at several positions in a water phantom. The models predict favourable biological dose-depth profiles for helium and lithium beams similar to the one for carbon beam. This result suggests that helium and lithium beams could also be used for radiation therapy.

- The correlations between RBE_{10} and $\bar{y}_F$ for proton, helium, lithium and carbon ions were studied along the beam axis. Such a correlation for carbon beam reveals the saturation effect. It is found that $\bar{y}_F$ (representing LET) may be similar at the plateau and tail regions, but still lead to very different biological effects.

- The impact of nuclear fragmentation reactions on RBE_{10} was estimated with MCHIT. The build-up of fragments reduces the biological effectiveness of ion beams. In the case of carbon-ion, the RBE_{10} is reduced by 10 % in the vicinity of the Bragg peak. Therefore, the effect of nuclear reactions should not be neglected in treatment planning systems for ion-beam cancer therapy.

- Finally we want to emphasize that the main conclusion of this study is that helium and lithium beams should be considered as rather favourable options for ion-beam cancer therapy. They have reduced fragmentation cross sections compared to the ^{12}C beam that makes them preferable for treatment of deeply-seated tumours. On the other hand, they have a reduced lateral scattering compared to the proton beam. At the same time the biological effectiveness of these beams is only slightly lower than that of ^{12}C beam.

Chapter 6

RBE and Cell Survival Fraction for SOBP Ion Beams

The advantage of charged particles, in particular, protons and carbon nuclei, used for radiation therapy of cancer consists in elevated dose delivered at the end of projectile range in tissues. The plateau of the depth-dose distribution at the entrance of a monoenergetic beam terminates with a sharp Bragg peak which can be targeted at the tumour. Such a dose profile helps to spare healthy tissues located in front of the tumour as well as beyond the projectile range. Since a set of beam energies is typically used in treatments to cover the whole tumour volume, the resulting dose distribution is characterized by a spread-out Bragg peak (SOBP) [7, 117, 118] with a wide domain of elevated dose.

The damage of healthy tissues during therapy can be essentially reduced if the ratio between the relative biological effectiveness (RBE) values at the SOBP region and plateau is favourable. As recognized almost 40 years ago in radiobiological experiments with SOBP beams of light nuclei performed at Berkeley [119], this RBE ratio is greater than 1 and increases with ion charge up to carbon. It was also found that this ratio decreases for Ne and becomes less than 1. In 1994 first patient treatments with beams of carbon nuclei started in Japan at National Institute of Radiological Sciences (NIRS) [120] and in 1997 in Germany at Gesellschaft für Schwerionenforschung (GSI) [7]. Later the advantages of ^{12}C with respect to ^{3}He and ^{20}Ne were confirmed in experiments at NIRS with these nuclear beams [28]. As explained [121], the RBE of 135 MeV/u ^{12}C beam with the LET of 65 keV/µm was found similar to the RBE of neutrons which have been used for treatment at NIRS during last 20 years. This similarity also motivated the choice of carbon nuclei for treatments at NIRS. In the last decades localized tumours have been successfully treated with beams of carbon nuclei at several facilities constructed in Japan and Germany [2, 111, 112, 122–124].

Despite of the broad clinical experience collected worldwide with proton and carbon-ion beams, other light nuclei can be also considered as future therapy options. The radiobiological properties of proton and ^{12}C beams were compared in several studies, see e.g. Refs.[125, 126]. However, less attention has been paid so far to ^{4}He or ^{16}O and to their comparison with protons and ^{12}C. There exist several clinical rationale behind the use of ^{4}He and ^{16}O for therapy:

i) ^{4}He and ^{16}O beams have a reduced lateral spread of the dose distribution

compared to protons;

ii) their RBE in the target volume is higher compared to protons;

iii) lower dose in the tail region and lower RBE in the plateau is expected for ^{4}He compared to ^{12}C due to reduced nuclear fragmentation of ^{4}He;

iv) ^{16}O is a promising option for hypoxic tumours as it provides a higher dose-averaged LET in the target volume compared to ^{12}C.

The choice of ion species and their energies at each new particle therapy facility [127–129] essentially depends on LET and RBE of the projectiles under consideration. The distributions of dose, LET and dose-averaged LET of ^{1}H, ^{4}He, ^{6,7}Li, ^{8}Be, ^{10}B, ^{12}C, ^{14}N and ^{16}O nuclei of therapeutic energies were studied [113, 114] by means of Monte Carlo simulations with SHIELD-HIT and FLUKA codes, respectively. Similar distributions for ^{1}H, ^{3}He, ^{12}C, ^{20}Ne and ^{58}Ni were calculated [54] with the GEANT4 toolkit to study their dependence on the ions charge and energy. It was assumed [113] that ions with LET above 20 keV/μm should be used for efficient cancer therapy as such species induce on average two or more double strand breaks in DNA close to each other. However, as pointed out in the same work, this limit is not sharp and ought to vary with ion mass and charge. This indicates that the RBE of respective ions has to be additionally considered for an accurate comparison of their biological action. Indeed, as shown in our recent work [60], there is no direct correspondence between RBE and the frequency-mean lineal energy $\bar{y}_F$, which represents LET, for monoenergetic beams of therapeutic energies. Similar RBE values were estimated [60] at the peak and plateau regions which are characterized, however, by very different $\bar{y}_F$.

As demonstrated [60], microdosimetry spectra for monoenergetic ^{1}H, ^{4}He, ^{7}Li and ^{12}C nuclei propagating in a water phantom can be accurately described with our Monte Carlo model for Heavy-Ion Therapy (MCHIT) [56], and this model coupled with the Microdosimetric Kinetic model (MKM) [3, 35] can be used to calculate the respective RBE profiles. In the present chapter we evaluate ^{4}He and ^{16}O for cancer therapy as complementary options to ^{1}H and ^{12}C by considering the biological dose distribution with a 6 cm SOBP delivered by these four projectiles. This is an important prerequisite for planning radiobiological experiments with ^{4}He and ^{16}O SOBP beams and extending existing treatment planning systems to operation with ^{4}He and ^{16}O.

The experimental data [3] collected at HIMAC for the 6 cm SOBP obtained by the moderation of a 290 MeV/u ^{12}C beam are used as a reference. The results of microdosimetry simulations are validated by comparison with microdosimetry data collected for ^{1}H, ^{4}He and ^{12}C beams [3]. This makes possible to predict the RBE and cell survival profiles for ^{16}O beams and compare all four ion species in a common framework.

Results of the comparative study of RBE and cell survival fractions for ^{1}H, ^{4}He, ^{12}C and ^{16}O beams presented in this chapter were published in Ref. [62].

6.1 Materials and methods

6.1.1 Modelling of physical and biological properties of ion beams

Following the validation of MCHIT for microdosimetry of monoenergetic ^{7}Li and ^{12}C beams [58, 60], this model is applied to microdosimetry of SOBP dose distributions considered in the present study. In the measurements performed at NIRS with a 6 cm SOBP for 160 MeV ^{1}H, 150 MeV/u ^{4}He and 290 MeV/u ^{12}C [3] the data for frequency-mean lineal energy, $\bar{y}_F$, dose-mean lineal energy, $\bar{y}_D$, and saturation-corrected dose-mean lineal energy, y^* [8] were collected. The microdosimetry spectra were measured with a walled TEPC corresponding to a tissue-equivalent sphere of 1 μm in diameter.

The GEANT4 version 9.5 with patch 02 is used to build the present version of MCHIT. Electromagnetic interactions are described using G4EmPen+IonGas. Nuclear collisions are modelled with G4BIC for proton, helium and lithium beams, while G4QMD is involved in simulations with carbon and oxygen beams. More details on the TEPC modelling, physics processes and respective GEANT4 models in MCHIT are given in Section 2.3.

The modified MKM model [3] is applied for modelling RBE and survival fraction of cells. Model parameters calculated by Kase *et al.* [3] for human salivary gland (HSG) tumour cells ($\alpha_0 = 0.13\,\mathrm{Gy}^{-1}$, $\beta = 0.05\,\mathrm{Gy}^{-2}$, $\rho = 1\,\mathrm{g/cm}^3$, $r_d = 0.42$ μm, $y_0 = 150$ μm) are assumed in this study (see Section 1.3.2 for details on MKM). As demonstrated [3], the same value of parameter $\beta = 0.05$ Gy^{-2} can be used to fit the survival fraction of cells for X-rays and ions. This justifies the assumption of the MKM model that β is independent of LET while the impact of different radiation qualities can be described by different values of y^*.

6.1.2 Composing SOBP profiles from a library of pristine Bragg peaks

The computing time required for treatment planing in carbon-ion therapy can be reduced by using pre-computed libraries of dose and RBE distributions for monoenergetic beams [130–132]. The aim of the treatment planning is to find an optimum superposition of many beams with their individual energy, position and intensity in order to obtain the prescribed biological SOBP dose profile. It is expected that a similar approach will be also suitable for other therapeutic beams, like ^{4}He and ^{16}O. Therefore, we implemented a common algorithm to calculate the relative weights of pre-defined monoenergetic beams of ^{1}H, ^{4}He, ^{12}C and ^{16}O to obtain flat biological SOBP distributions for each projectile as a product of the physical dose and RBE calculated for mixed radiation field.

A library of depth-dose profiles and the corresponding microdosimetry spectra for different beam energies and nuclei were calculated by Monte Carlo simulations with MCHIT. They are used as input data for a procedure similar to one implemented at NIRS [121]. According to this procedure based on the theory of dual radiation action [133] the survival fraction of cells exposed to mixed radiation is calculated

as:

$$S_{mix}(D) = \exp\left(-\alpha_{mix}D - \beta_{mix}D^2\right); \tag{6.1}$$

$$\alpha_{mix} = \sum f_i\alpha_i; \tag{6.2}$$

$$\sqrt{\beta_{mix}} = \sum f_i\sqrt{\beta_i}. \tag{6.3}$$

Here f_i is the weight coefficient (fraction) of the local physical dose of the ith monoenergetic beam which contribute to the total physical dose D, while α_i and β_i are the parameters of the LQ model specific to ith monoenergetic beam. The parameters α_i and β_i are calculated along the beam axis using MCHIT coupled with the modified MKM model as described in Section 6.1.1. The resulting $\mathrm{RBE}_{10,mix}$ for the mixed radiation is calculated from the survival fraction of cells $S_{mix}(D)$ and it also depends on the depth. RBE_{10} and $\mathrm{RBE}_{10,mix}$ for the monoenergetic and SOBP (mixed) beams, respectively, are considered in the following. They account for the relative biological effectiveness corresponding to 10% survival of cells.

A dedicated algorithm to obtain f_i for a given biological SOBP was developed. It starts with the determination of the weight at the distal edge of the SOBP distribution and then calculates weights for less energetic beams by adjusting their contribution to provide a flat SOBP plateau.

6.2 Results and discussion

6.2.1 Pristine Bragg peaks

Simulation results for monoenergetic 152.7 MeV ^{1}H, 152.1 MeV/u ^{4}He, 290 MeV/u ^{12}C and 345.4 MeV/u ^{16}O beams are shown in Fig. 6.1. The beam energies were chosen to place the Bragg peaks of all four beams at the depth of $\sim$161.8 mm.

As expected, the ^{12}C and ^{16}O beams deposit much higher energy at the Bragg peak compared to ^{1}H and ^{4}He. However, higher energy deposition by ^{12}C and ^{16}O is also observed at the entrance and tail region. Therefore, no clear advantages of therapeutic ^{12}C and ^{16}O beams with respect to ^{1}H and ^{4}He beams regarding healthy tissues can be inferred exclusively from the analysis of the considered depth-dose distributions.

The RBE_{10} profiles for the considered ^{1}H, ^{4}He, ^{12}C and ^{16}O beams are shown in the middle panel of Fig. 6.1 and they differ from each other. The RBE_{10} for ^{12}C beam estimated from the parameters of a LQ fitting on survival curves of HSG cells with β fixed to 0.05 Gy^{-2} [3] is presented for comparison. The RBE_{10} profile for ^{12}C beam calculated with MCHIT coupled with the MKM model agrees well with the profile which is also calculated with MKM, but using the measured microdosimetry data on y^* [3]. A prominent difference between RBE_{10} profiles for ^{12}C and ^{16}O and the profile for ^{4}He is seen in the insert of Fig. 6.1. The backward shift of the maximum of RBE_{10} of ^{12}C and ^{16}O with respect to the position of the ^{4}He maximum is due to the saturation effect. It is also found that ^{12}C and ^{16}O nuclei are characterized by higher RBE values for 10 % survival of HSG cells along the whole irradiated medium. Their maximum values reach 2.9 and 3.1, respectively, close to the Bragg peak. At the same time the RBE_{10} values for helium are relatively low at the entrance and

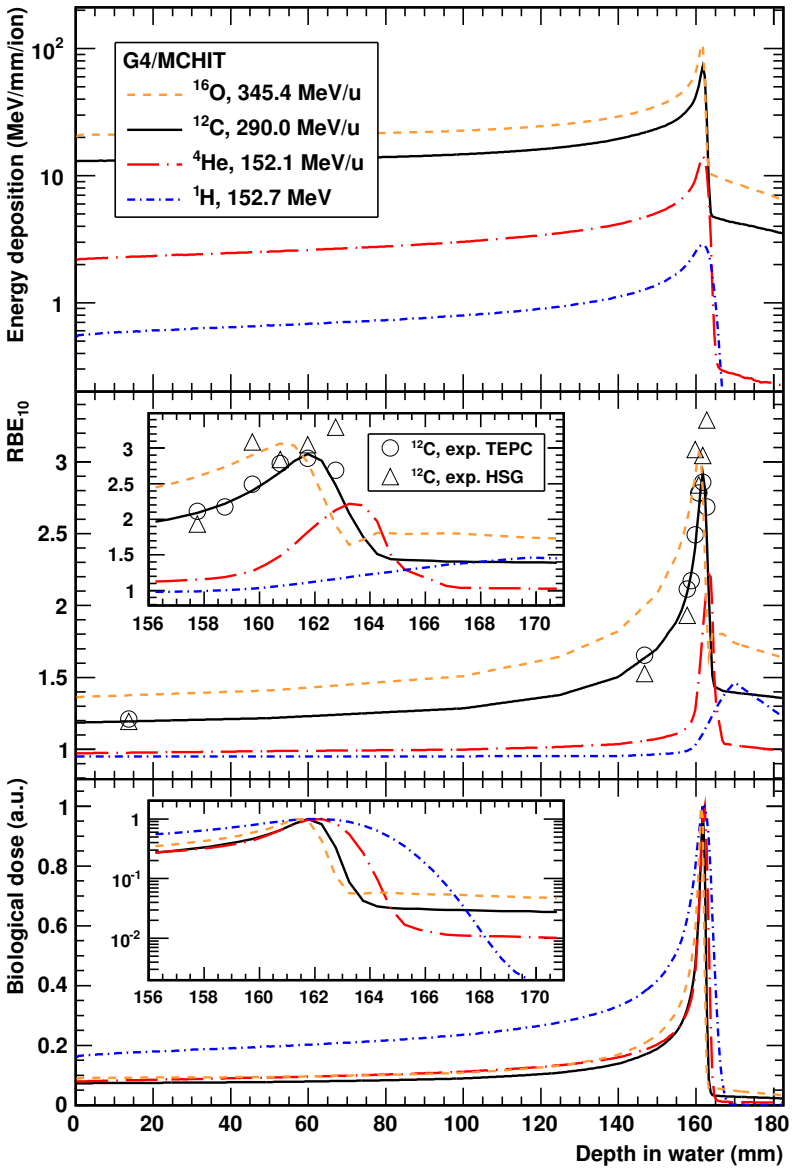

Figure 6.1: Calculated energy deposition per beam particle (top panel), RBE_{10} for HSG cells (middle panel) and biological dose (bottom panel) for ^{1}H, ^{4}He, ^{12}C and ^{16}O beams in water. The RBE_{10} calculated from measured values of y^* [3] are shown by circles. The RBE_{10} estimated from LQ fitting on survival curves of HSG cells [3] are presented by triangles. The biological dose distributions for all ions were rescaled to get the same value at the maximum.

tail regions and demonstrate a steep rise to 2.2 at the Bragg peak position. Before the Bragg peak the RBE_{10} values for proton beam are slightly below 1. and increase to 1.5 well after the distal edge of the proton Bragg peak. This rise of RBE_{10} for proton beam is explained by the presence of secondary nucleons produced by beam protons in water and propagating beyond the Bragg peak.

Finally, the biological dose profiles for ^{1}H, ^{4}He, ^{12}C and ^{16}O (a.u.) are presented in the bottom panel of Fig. 6.1. They were rescaled to get the same value at the maximum. The profiles for ^{4}He, ^{12}C and ^{16}O are very similar to each other. They

are characterized by more sharp rise and fall of the biological dose in the Bragg peak region compared to protons. After renormalization lower biological dose for ^{4}He, ^{12}C and ^{16}O is predicted at the entrance with respect to protons. SOBP profiles of biological dose for all these projectiles are considered below.

6.2.2 RBE distributions for ^{1}H, ^{4}He,^{12}C and ^{16}O

As explained in Section 6.1.2, a given biological SOBP dose distribution is composed from a set of depth-dose and depth-y^* profiles calculated with MCHIT for monoenergetic beams. Such a library created in the present work contains pristine Bragg curves with a 1 mm increment of the Bragg peak positions which are within 90–175 mm depth in water. Seven pristine Bragg peaks for ^{12}C covering a 60 mm domain in depth are shown in Fig. 6.2 to illustrate the content of this library. The

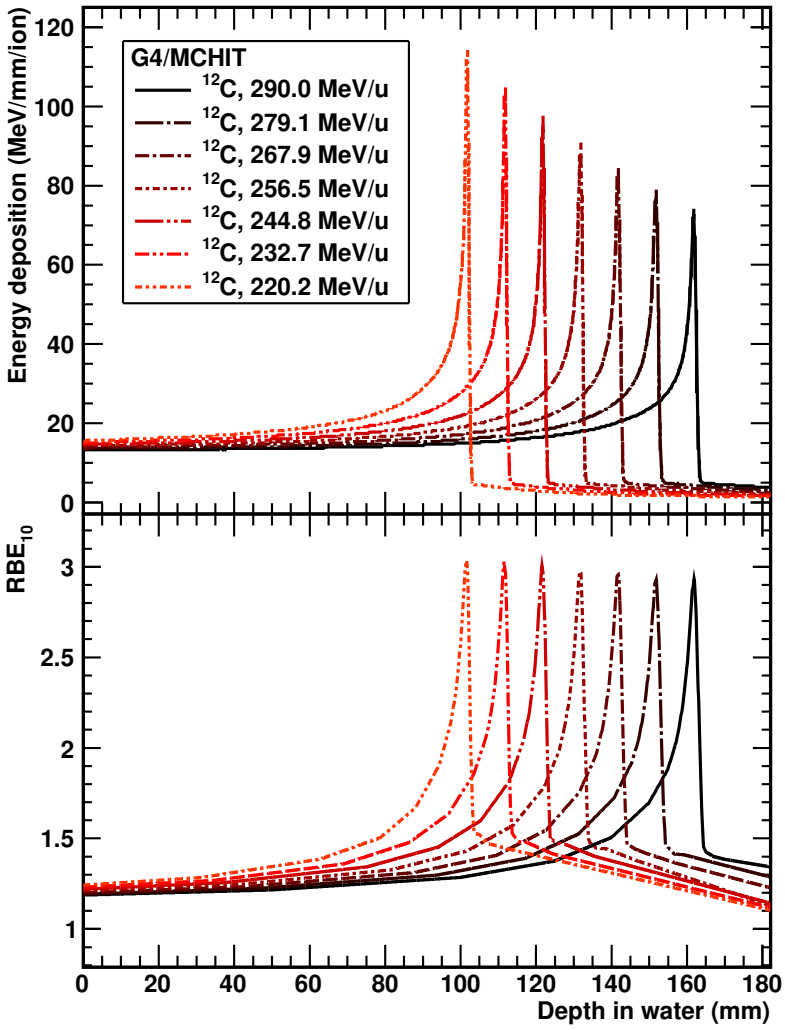

Figure 6.2: Energy deposition profiles for ^{12}C in water in 10 mm steps (top panel) and the corresponding RBE_{10} profiles for HSG cells calculated with MCHIT and the MKM model (bottom panel).

microdosimetry variables which are also stored in the library as functions of depth are used to estimate RBE_{10} profiles according to the MKM model. The respective

RBE_{10} distributions are shown in Fig. 6.2 for the same beams. As seen in Fig. 6.2, the height of the Bragg peak noticeably diminishes with depth, while the maximum RBE_{10} remains almost constant (~ 3) over the considered depth range.

A 6 cm-wide SOBP profile of biological dose for 290 MeV/u ^{12}C beam, which was built according to the above-described procedure is shown in the top panel of Fig. 6.3. Here and in the following such profiles are normalized to 1 at the plateau in

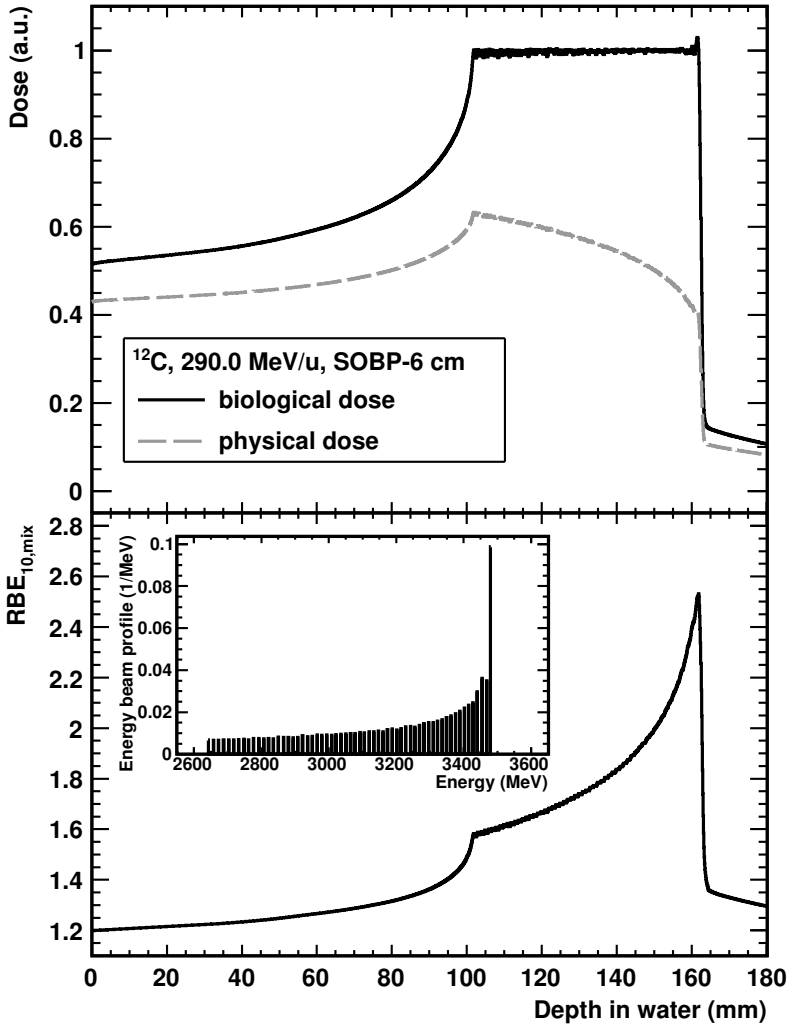

Figure 6.3: A 6 cm-wide SOBP biological dose distribution in water for 290 MeV/u ^{12}C ion beam and the respective physical dose (top panel). $RBE_{10,mix}$ profile for HSG cells (bottom panel) and the distribution of beam energy used to build the SOBP profiles (insert).

order to facilitate the comparison of various ion species. The resulting distribution has a flat SOBP plateau with negligible fluctuations due to the presence of individual Bragg peaks. In contrast, the corresponding SOBP distribution of the physical dose, which is also shown in Fig. 6.3 is not flat, but rather decreases with depth. The respective RBE_{10} amounts to ~ 1.6 at the proximal edge of the SOBP, while it is slightly above 2.5 at the distal edge, see the bottom panel of Fig. 6.3. The insert in the bottom panel of Fig. 6.3 demonstrates the calculated relative weights for monoenergetic beams used to build the SOBP distribution of biological dose shown

in Fig. 6.3.

The 6 cm-wide $RBE_{10,mix}$ profiles calculated for HSG cells for 152.7 MeV ^{1}H, 152.1 MeV/u ^{4}He, 290 MeV/u ^{12}C and 345.4 MeV/u ^{16}O beams are presented in Fig. 6.4. They were calculated with the MKM model basing on microdosimetry data generated by Monte Carlo simulations with MCHIT. The reliability of these profiles can be proved by comparing them with $RBE_{10,mix}$ calculated by two different approaches. In the first case, $RBE_{10,mix}$ is also calculated with the MKM model, but on the basis of measured y^* values [3]. In the second approach, $RBE_{10,mix}$ is calculated using the parameters of LQ fitting of survival curves of HSG cells with β fixed to 0.05 Gy^{-2} [3]. The profiles based on MCHIT simulations agree very well with the $RBE_{10,mix}$ estimated on the basis of the two set of experimental data, see Fig. 6.4. In order to make such comparison, experimental values [3] corresponding to ^{1}H and ^{4}He were shifted in depth due to the difference of beam energies used in measurements and simulations.

A good agreement with data for ^{1}H, ^{4}He and ^{12}C suggests that this method can be also applied to ^{16}O beam. The distribution of $RBE_{10,mix}$ for ^{16}O obtained on the basis of microdosimetry simulations with MCHIT is shown in Fig. 6.4 for comparison. The shapes of $RBE_{10,mix}$ profiles for ^{4}He, ^{12}C and ^{16}O are found to be similar with a rise of RBE for ^{12}C and ^{16}O at the proximal edge of the SOBP distribution. A characteristic rise of RBE for ^{1}H beyond 165 mm depth at the distal region of the SOBP is found, similarly to the case of monoenergetic proton beam, see Section 6.2.1. It is found that $RBE_{10,mix} \sim 1$ at the entrance region of ^{1}H and ^{4}He beams. The ratio between $RBE_{10,mix}$ values at the proximal (depth of $\sim$105 mm) and distal (depth of $\sim$165 mm) regions is larger for ^{16}O compared to ^{12}C. The $RBE_{10,mix}$ profile for ^{16}O demonstrates the most pronounced tail with respect to other projectiles.

6.2.3 SOBP distributions of biological dose

The SOBP distributions of biological dose D_{bio} for ^{1}H, ^{4}He, ^{12}C and ^{16}O are shown in Fig. 6.5. They are calculated for HSG cell as a product of physical dose calculated with MCHIT and $RBE_{10,mix}$ obtained with the MKM model on the basis of microdosimetric modelling with MCHIT. All four SOBP distributions presented in Fig. 6.5 are 6 cm wide, and they are normalized to 1 at the plateau to facilitate the comparison of their shapes and ratios between the plateau and entry channel. Therefore, in the following the distributions of D_{bio} are discussed in terms of dose relative to the plateau values.

The distribution of D_{bio} for ^{12}C is characterized by the lowest values at the entrance channel. This helps to spare healthy tissues located in front of the target volume in treatments with ^{12}C. In contrast, the highest entrance dose is predicted for protons. However, the tail of the proton distribution beyond the distal edge of the plateau is negligible, while it is essential both for ^{12}C and ^{16}O. This indicates that the proton beam is the best option if very sensitive organs are located behind the tumour volume. The choice of ion species for each specific treatment can, in principle, provide an optimal ratio between the doses in the entrance and tail regions.

The distribution of D_{bio} for ^{4}He demonstrates a favorably small dose at the tail

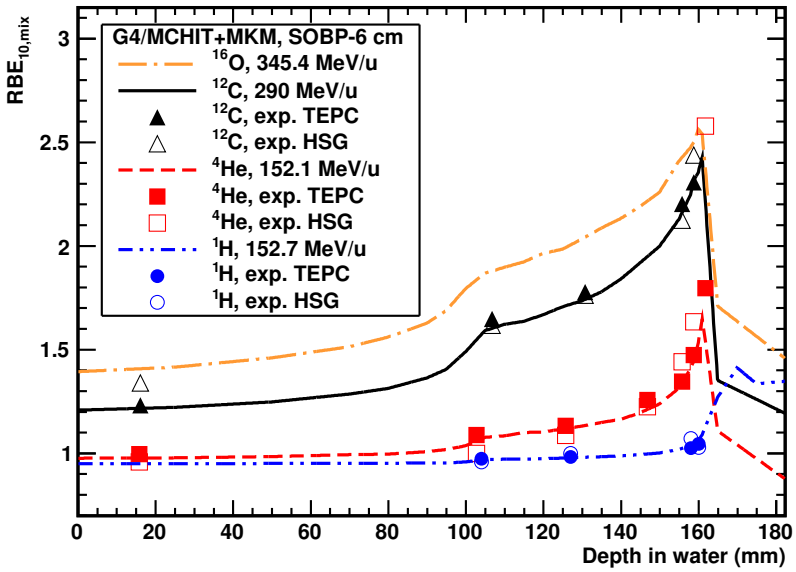

Figure 6.4: $RBE_{10,mix}$ distributions calculated with MCHIT and MKM for 6 cm SOBP beams of ^{1}H, ^{4}He, ^{12}C and ^{16}O. The beam energy profiles for ^{1}H, ^{4}He and ^{16}O were defined in such a way that they yield a 6 cm SOBP at the same depth as for 290 MeV/u ^{12}C ion. The $RBE_{10,mix}$ values estimated with the MKM model from measured y^* [3] are presented by full symbols as explained in the legend. The $RBE_{10,mix}$ values estimated from LQ fitting of survival curves of HSG cells are presented by open symbols.

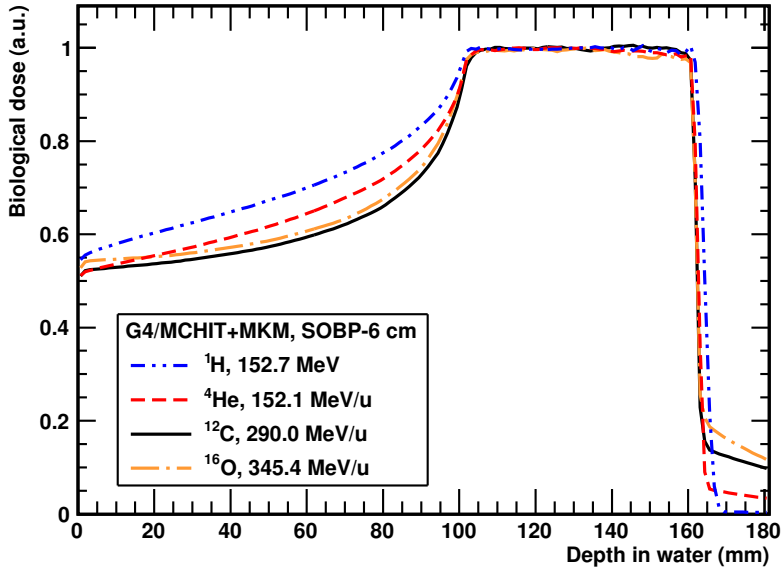

Figure 6.5: SOBP biological dose profiles for ^{1}H, ^{4}He, ^{12}C and ^{16}O nuclei obtained as a product of physical dose calculated with MCHIT and $RBE_{10,mix}$ shown in Fig. 6.4. The distributions for all projectiles were rescaled to get the same value at the plateau.

region, while its entrance value is higher compared to ^{12}C. The biological dose delivered by ^{16}O to normal tissue is slightly increased both in front of the target volume

and behind it compared to ^{12}C. From the analysis of D_{bio} distributions one can conclude that ^{12}C is the best treatment option compared to ^{1}H, ^{4}He and ^{16}O, unless only a very low D_{bio} is acceptable in the tail region. In the latter case protons become the best treatment option.

6.2.4 Distributions of cell survival fractions

The central part of our study is devoted to the comparison of survival fractions of cells S_{mix} calculated as a function of depth in the water phantom, which are estimated for tissues of different radiosensitivity. This makes possible to evaluate the respective therapeutic outcome for such tissues.

The distributions of S_{mix} calculated for cells (tissues) with $(\alpha/\beta)_{X-rays} = 3.8\,\mathrm{Gy}$, 2 Gy and 10 Gy after exposing them to ^{1}H, ^{4}He, ^{12}C and ^{16}O SOBP beams are shown in Fig. 6.6. Throughout this text the parameters for HSG cells were taken as $\alpha_0 = 0.13\,\mathrm{Gy}^{-1}$ and $(\alpha/\beta)_{X-rays} = 3.8\,\mathrm{Gy}$ [3]. Hereafter the radiosensitivity of such tissues is considered as normal. This serves as a natural reference point for comparison with two other tissues with their parameters taken following Kase *et al.* [134]. The latter two cases correspond to early responding tissue (with model parameters $\alpha_0 = 0.44\,\mathrm{Gy}^{-1}$, $(\alpha/\beta)_{X-rays} = 10\,\mathrm{Gy}$) very sensitive to radiation and late responding tissue ($\alpha_0 = 0.04\,\mathrm{Gy}^{-1}$, $(\alpha/\beta)_{X-rays} = 2\,\mathrm{Gy}$) which is radioresistant.

The dose applied to HSG cells (normal radiosensitivity) leads to their 10% survival at the target volume for all four beams. The beams of ^{4}He and ^{12}C equally well spare tissue in the entrance channel, while the impact of ^{1}H and ^{16}O is stronger there. As one can expect, the main difference between light ^{1}H, ^{4}He and heavier ^{12}C, ^{16}O is revealed beyond the distal edge of SOBP profile due to the tail of secondary fragments from ^{12}C and ^{16}O. One can also note that ^{16}O is the worst option for HSG cells, while ^{4}He is the best one.

In the case of early and late responding tissues, see Fig. 6.6, middle and bottom panels, the relations between the survival fractions estimated for ^{1}H, ^{4}He, ^{12}C and ^{16}O beyond the distal edge of the SOBP plateau are quite similar to the case of HSG cells. This is because of the fact that the dose in the tail region is defined by the presence of secondary fragments, which is essential for ^{12}C and ^{16}O beams. In the case of early responding tissues less than 5 % of cells survive in the tumour volume, but their survival outside is also unacceptably low (10–20 %). This means that in this case there are no advantages of charged particle therapy with respect to the intensity modulated radiation therapy (IMRT) with photons.

In the case of late responding tissues more cells ($\sim 15\,\%$) survive in the tumour volume after the impact of ^{1}H, ^{4}He, ^{12}C and ^{16}O SOBP beams, see Fig. 6.6, bottom panel. The ^{12}C and ^{16}O SOBP beams are very effective in killing tumour cells, but the cell survival is also lower in the entrance channel ($\sim 40\,\%$) compared to $\sim 50\,\%$ for ^{1}H and ^{4}He. By considering all three sensitivity cases one can conclude that the ^{4}He beam is equally suitable for irradiation of tissues with normal and low radiosensitivity as the ^{12}C beam. Moreover, due to the reduced fragmentation of ^{4}He, this option can be even better than ^{12}C when sparing tissues after the tumour volume is crucial. At the same time the ^{16}O beam has no clear advantages compared to ^{12}C. Due to higher ionization in the entrance channel and enhanced fragmentation more cells are killed by ^{16}O beam outside the tumour volume compared to ^{12}C beam.

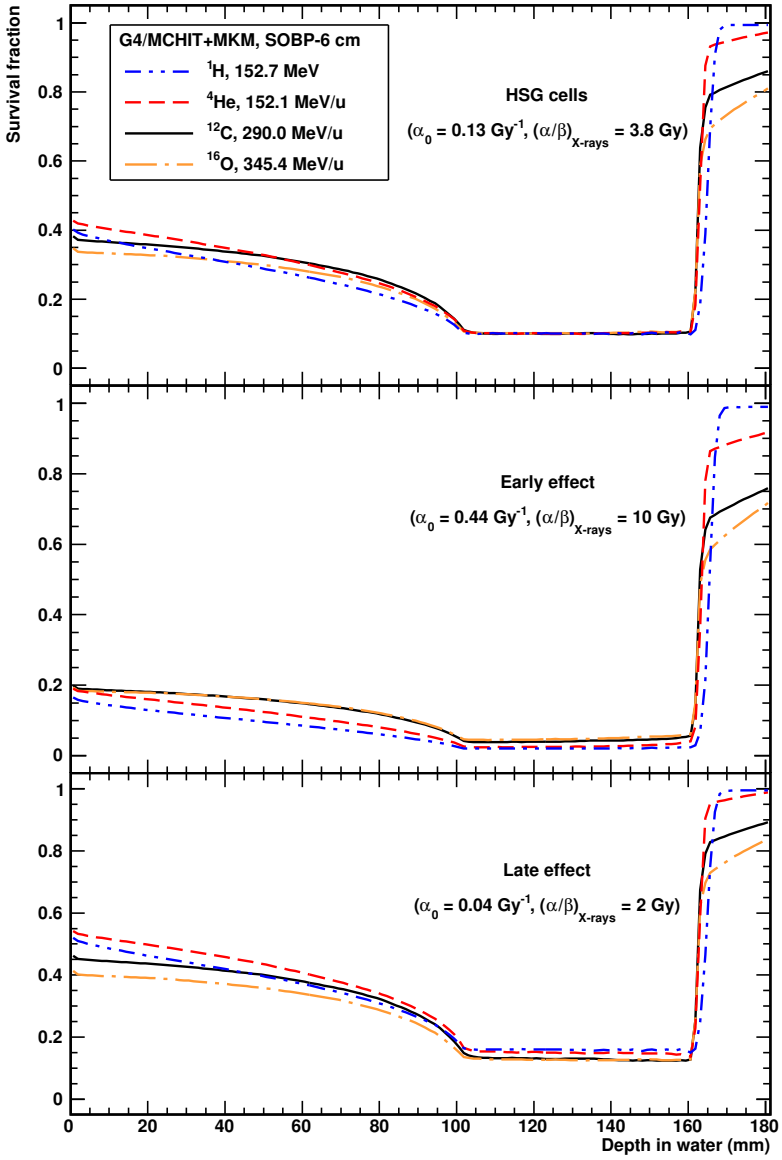

Figure 6.6: Distributions of cell survival rates S_{mix} after irradiation with ^{1}H, ^{4}He, ^{12}C and ^{16}O SOBP beams calculated for tissues with $(\alpha/\beta)_{X-rays} = 3.8$ Gy (HSG cells, top panel), 2 Gy (early responding tissue, middle panel) and 10 Gy (late responding tissue, bottom panel). The values of α_0 parameter of the MKM model are taken as 0.13 Gy^{-1}, 0.44 Gy^{-1} and 0.04 Gy^{-1}, respectively.

However, one can consider ^{16}O is a good option for highly resistant tumours, as it effectively kills cells in the tumour volume.

Conclusions

In this chapter we presented our approach based on Monte Carlo simulations of microdosimetric spectra of monoenergetic beams of ^{1}H, ^{4}He, ^{12}C and ^{16}O in water. It provides y^* values as input to the modified MKM model [4] for calculating $\mathrm{RBE}_{10,mix}$ for HSG cells for SOBP distributions composed from monoenergetic beams of these

projectiles. This method gives $RBE_{10,mix}$ for ^{1}H, ^{4}He, ^{12}C which are in full agreement with $RBE_{10,mix}$ also calculated with the MKM model, but from measured y^* [3] and $RBE_{10,mix}$ calculated from the parameters of LQ fitting of survival curves of HSG cells [3]. This makes us confident in extending our approach to ^{16}O beams for which the respective data are not available. Our approach provides well-adjusted biological dose distributions for ^{1}H, ^{4}He, ^{12}C and ^{16}O with a very flat SOBP plateau. Thus basic properties of mixed radiation fields in treatments with these projectiles are emulated.

It is found that the shapes of $RBE_{10,mix}$ profiles for ^{4}He, ^{12}C and ^{16}O are similar to each other, while the $RBE_{10,mix}$ for protons is almost constant ($\sim 1.$) over the whole depth in water, excluding enhanced $RBE_{10,mix}$ (~ 1.2) after the distal edge of the SOBP plateau. Considerably lower $RBE_{10,mix}$ values are estimated in the entrance and tail region for ^{4}He compared to ^{12}C and ^{16}O. In the target volume the highest $RBE_{10,mix}$ values of 1.5–2.5 are calculated for ^{12}C and ^{16}O.

In order to reduce side effects of ion therapy such as radionecrosis [134] the damage to surrounding healthy tissues should be reduced as much as possible. With the help of our MCHIT model connected with the modified MKM model the severity of this damage is evaluated by calculating the cell survival fractions in healthy tissues for several kinds of therapeutic beams (^{1}H, ^{4}He, ^{12}C, ^{16}O). We considered the cases of normal (HSG cells), high and low radiosensitivity of tissues in the tumour volume and around it. The consideration of the impact of ^{1}H, ^{4}He, ^{12}C and ^{16}O SOBP beams in these three cases led us to the following conclusions:

- In the case of early responding tissues all four charged particle beams induce severe damage not only to the target volume, but also around it. Since in this case the region of high damage is not conformal to the target volume, the treatment with charged particles loses its advantages with respect to treatment with photons.

- In the case of tissues with normal radiosensitivity (HSG cells) ^{4}He and ^{12}C beams spare tissue in the entrance channel better than ^{1}H and ^{16}O ones.

- ^{4}He and ^{12}C nuclei are equally suitable for irradiation of tissues with normal and low radiosensitivity. The cell survival fractions calculated, respectively, for the entrance channel and target volume are similar for ^{4}He and ^{12}C.

- However, as soon as it is important to spare healthy tissues after the distal edge of the SOBP plateau, ^{4}He can be recommended due to the reduced nuclear fragmentation of these projectiles.

- No definitive advantages of ^{16}O with respect to ^{12}C were found, with the except of an enhanced impact of these heavier projectiles on radioresistant tumours.

In a recent work [25] the authors studied the possibility to spare healthy tissues by properly selecting ion species for therapy. In addition to ^{1}H, ^{4}He, ^{12}C they considered lithium, beryllium, boron and neon ions and calculated the dose to normal tissue delivered by these beams. However, the option of ^{16}O was not considered, while the Heidelberger Ionenstrahl-Therapiezentrum (HIT) in Heildeberg, Germany, provides ^{16}O beams of therapeutic energies [124, 135] in addition to ^{1}H, ^{4}He, ^{12}C. Treatments

at this facility are performed presently only with protons and carbon ions, but ^{16}O can be also used following respective pre-clinical studies. In this sense our study complements the results of Remmes *et al.* [25] by considering ^{16}O beams, and also by comparing cell survival profiles in ^{1}H, ^{4}He, ^{12}C and ^{16}O treatments in addition to biological dose profiles.

As suggested [136], multi modal irradiations with various nuclei can be used for LET-painting. In this method high-LET radiation is used to boost the LET in a hypoxic sub-volume of the target (hypoxic compartments of the tumour). At the same time low-LET radiation is applied to the complementary target volume. Such combination may increase tumour control and reduce side effects. This means that a thorough evaluation of the physical properties and biological effectiveness of different beams is necessary before they can be applied in real treatments. Our approach can be also used for estimating RBE and cell survival fractions for ^{7}Li, ^{8}Be, ^{10}B and ^{14}N nuclei prior to planning radiobiological experiments with these beams.

Summary

In the present thesis the interaction of ions with tissue-like media was investigated using the Monte Carlo model for Heavy-Ion Therapy (MCHIT) developed at the Frankfurt Institute for Advanced Studies. MCHIT is a GEANT4-based application intended to benchmark the physical models of GEANT4 and study the physical processes induced by therapeutic ion beams. It has been previously demonstrated that MCHIT can reproduce well the depth-dose profiles for light nuclei and the yields of secondary neutrons and charged fragments in nuclear collisions between the primary ion and nuclei of the medium. Besides, distributions of positron-emitting nuclei relevant for PET monitoring in ion-beam cancer therapy were also successfully calculated.

We have implemented several new features in MCHIT in order to extend the benchmarking of GEANT4 models and increase the resolution of energy deposition from millimetre to micrometre scale. This is a necessary step towards a more comprehensive understanding of the interactions of ion beams with tissue-like medium and modelling respective biological effects. Such developments allowed us to calculate microdosimetric quantities characterizing the radiation fields of accelerated nucleons and nuclei. In particular, the TEPC geometries were thoroughly implemented in MCHIT using rich possibilities offered by GEANT4. The results of our Monte Carlo simulations were compared with recent experimental microdosimetry data measured with various TEPCs. We have shown that MCHIT model is able to describe the spatial distribution of the total dose in tissue-like media which varies by many orders of magnitude with increasing radial distance from the beam axis. These and other results presented in this thesis were published in Refs. [57–62].

Our studies demonstrate that MCHIT is able to describe well the TEPC response function as well as the microdosimetry parameters for a broad selection of ions and beam energies relevant to space research and ion-beam cancer therapy. In particular, we have shown that microdosimetry spectra for protons calculated for a macroscopic-size TEPC filled with dilute gas agree well with microdosimetry spectrum calculated for the equivalent microscopic volume of water. In this way the basic assumption of the microdosimetry technique was validated by our Monte Carlo simulations with MCHIT.

The measurements of microdosimetry spectra behind thick targets open another possibility to validate Monte Carlo transport codes. Nuclear fragmentation reactions which happen, for instance, in a shielding material of a spacecraft or in beam-line elements in front of a patient, lead to a significant modification of the radiation fields in the regions of interest, *i.e.*, cell nuclei or sensitive volumes of TEPCs. While a TEPC placed on the beam axis is irradiated by primary ions and secondary

particles, only secondary particles contribute to the energy deposition far away from the beam axis. Therefore, a proper modelling of nuclear fragmentation reactions is crucial to the description of microdosimetry spectra both on the beam axis and far from the beam. Contributions of primary beam nuclei and secondary fragments were thoroughly evaluated with MCHIT and compared with existing experimental data.

Two hadronic models of GEANT4 for the fast stage of nuclear collisions, namely the Light Ion Binary Cascade and the Quantum Molecular Dynamics, turned out to be equally suitable for describing general features of the microdosimetric spectra. However, both models underestimate the fluxes of protons and neutrons far from the beam and the yield of alpha particles. This indicates the necessity of improving nucleus-nucleus collision models in calculating the angular and energy distributions of secondary nucleons and light fragments. Further refining of nuclear fragmentation models could improve the description of the microdosimetry data and, therefore, provide a better understanding of the radiation effects from therapeutic beams of light nuclei.

The contributions of δ-electrons to the energy deposited in the TEPC was also investigated. Obviously, it varies at different detector locations in the radiation field. The propagation of energetic beam nuclei through a TEPC is accompanied by production of energetic δ-electrons, which may escape the sensitive volume, thus transporting and releasing the energy outside. This effect is less important at the Bragg peak and also far from the beam axis for the detectors impacted only by secondary nucleons, as they produce low-energy electrons with short ranges.

The in-field and out-of-field microdosimetry spectra for therapeutic ion beams were calculated with MCHIT in a consistent approach. Our computational method is useful to assess the biological effects of complex radiation fields from therapeutic ion beams, including effects of secondary neutrons produced in nuclear reactions. The contribution of secondary neutrons to out-of-field dose was estimated with MCHIT for pencil-like carbon beams typical in radiation therapy. It was shown that the relative contribution of neutrons increases rapidly as a detector moves away from the beam axis and backward. Since experimental identification of neutrons would require bulky detectors placed only outside the phantom, such microdosimetry measurements provide the only possibility to estimate the upper limits for the dose from neutrons and their radiation quality close to the target volume inside the phantom.

In addition to microdosimetry calculations with MCHIT performed for physical characterization of the radiation fields by ions, we also investigated the biological properties of ion beams, *e.g.* their relative biological effectiveness (RBE), by means of a radiobiological model, namely the modified Microdosimetric-Kinetic model (MKM). The MKM uses the stochastic patterns of energy deposition at micrometre scale in describing cell response to radiation. MCHIT+MKM allowed us to estimate RBE and biological dose for therapeutic ion beams at several positions in a tissue-like phantom which is relevant to ion-beam cancer therapy.

We applied MCHIT+MKM to evaluate the impact of nuclear fragmentation reactions on the biological effectiveness of ion beams. The build-up of fragments reduces the RBE due to the loss of beam particles, which are characterized by higher stopping power than all the fragments together. In particular, the RBE_{10} (RBE at a level of 10 % survival fraction of cells) for HSG cells irradiated by therapeutic

carbon-ions is decreased by $\sim 10\,\%$ due to nuclear fragmentation in the vicinity of the Bragg peak. It is clear that the effect of nuclear reactions is not negligible and should be considered in treatment planning systems for ion-beam cancer therapy. The variation of biological effectiveness of ions as a result of their propagation in extended media has also implications to the choice of materials and shielding thickness in constructing spacecrafts.

Physical and biological dose distributions of monoenergetic ion beams in tissue-like media were investigated with MCHIT+MKM. The models predict favourable biological dose-depth profiles for helium and lithium beams similar to the one for carbon beam. These nuclei should be considered as favourable options for ion-beam cancer therapy. They have reduced fragmentation cross sections compared to the carbon nuclei that makes them preferable for deeply-seated tumours. Besides, they also have a reduced lateral scattering compared to the proton beam. At the same time the biological effectiveness of these beams is only slightly lower than that of carbon beam. These results suggest that helium and lithium beams could also be successfully used for radiation therapy.

Detailed simulations were also performed for spread-out Bragg peaks (SOBP) required to treat extensive tumours in ion-beam cancer therapy. An algorithm was developed to simulate SOBP for light nuclei from monoenergetic beams of various projectiles. We have demonstrated well-adjusted biological dose distributions for ^{1}H, ^{4}He, ^{12}C and ^{16}O with a very flat SOBP plateau calculated with MCHIT+MKM. This allowed us to study RBE and survival fraction of cells in conditions which are highly relevant to radiation therapy.

From SOBP simulations with MCHIT+MKM we calculated $\mathrm{RBE}_{10,mix}$ profiles for protons, ^{4}He, ^{12}C and ^{16}O, where $\mathrm{RBE}_{10,mix}$ stands for the RBE_{10} for a SOBP beam. We found that the shapes of $\mathrm{RBE}_{10,mix}$ profiles for ^{4}He, ^{12}C and ^{16}O are similar to each other, while the $\mathrm{RBE}_{10,mix}$ for protons is almost constant (~ 1) over the whole depth in water, excluding enhanced $\mathrm{RBE}_{10,mix}$ (~ 1.2) after the distal edge of the SOBP plateau. Considerably lower $\mathrm{RBE}_{10,mix}$ values are estimated in the entrance and tail region for ^{4}He compared to ^{12}C and ^{16}O. In the target volume the highest $\mathrm{RBE}_{10,mix}$ values of 1.5–2.5 are obtained for ^{12}C and ^{16}O.

In order to reduce side effects of ion therapy such as radionecrosis the damage to surrounding healthy tissues should be reduced as much as possible. With the help of our MCHIT model connected with the modified MKM model the severity of this damage was evaluated by calculating the cell survival fractions in healthy tissues for several therapeutic beams, namely ^{1}H, ^{4}He, ^{12}C and ^{16}O. We considered the cases of normal, high and low radiosensitivity of tissues in the tumour volume and around it. In the case of early responding tissues all four charged particle beams induce severe damage not only to the target volume, but also around it. Since in this case the region of high damage is not conformal to the target volume, the treatment with charged particles loses its advantages with respect to treatment with photons. In the case of tissues with normal radiosensitivity ^{4}He and ^{12}C beams spare tissue in the entrance channel better than ^{1}H and ^{16}O ones. For all cases the cell survival fractions calculated for the entrance channel and target volume are similar for ^{4}He and ^{12}C. However, as soon as it is important to spare healthy tissues behind the distal edge of the SOBP plateau, ^{4}He can be recommended due to the reduced nuclear fragmentation of these projectiles. As for oxygen beam, no

definitive advantages with respect to carbon were found, with the exception of an enhanced impact of these heavier projectiles on radioresistant tumours.

In summary, the methods developed in this thesis were applied to characterize the interactions of ions with tissue-like materials. MCHIT+MKM allowed us to study the physical and biological properties of ion beams. The main results of the thesis are as follows:

- MCHIT is able to describe the spatial distribution of the physical dose in tissue-like media and microdosimetry spectra for ions with energies relevant to space research and ion-beam cancer therapy.
- MCHIT+MKM predicts a reduction of the biological effectiveness of ions propagating in extended medium due to nuclear fragmentation reactions.
- We predicted favourable biological dose-depth profiles for monoenergetic helium and lithium beams similar to the one for carbon beam. Well-adjusted biological dose distributions for ^{1}H, ^{4}He, ^{12}C and ^{16}O with a very flat SOBP plateau were calculated with MCHIT+MKM.
- The shapes of RBE profiles for SOBP ^{4}He, ^{12}C and ^{16}O beams are similar to each other. However, considerably lower RBE values are estimated in the entrance and tail region for ^{4}He beam.
- MCHIT+MKM predicts less damage to healthy tissues in the entrance channel for SOBP ^{4}He and ^{12}C beams compared to ^{1}H and ^{16}O ones. No definitive advantages for oxygen ions with respect to carbon were found.

Outlook

Further developments of MCHIT shall extend the modelling of energy deposition to the nanometre scale. The code will use electromagnetic models for low-energy processes from the GEANT4-DNA project which apply the detailed history approach. This extension of the code will allow to study the spatial patterns of energy deposition at few nanometres around the ion track in addition to the present capabilities to simulate the energy deposition at the micrometre scale. Therefore, we will be able to investigate the structure of ion tracks and simulate nanodosimetry measurements. This is important for description of DNA damage formation. The spatial and temporal distribution of the initial DNA insults are crucial for the biological modelling of the cell response.

Bibliography

[1] Elsaesser T, Weyrather WK, Friedrich T, Durante M, Iancu G, *et al.* 'Quantification of the relative biological effectiveness for ion beam radiotherapy: direct experimental comparison of proton and carbon ion beams and a novel approach for treatment planning.' *Int. J. Radiat. Oncol.* (2010) **78**(4): 1177–1183. doi:10.1016/j.ijrobp.2010.05.014.

[2] Durante M, Loeffler JS. 'Charged particles in radiation oncology.' *Nat. Rev. Clin. Oncol.* (2010) **7**(1): 37–43. doi:10.1038/nrclinonc.2009.183.

[3] Kase Y, Kanai T, Matsumoto Y, Furusawa Y, Okamoto H, *et al.* 'Microdosimetric measurements and estimation of human cell survival for heavy-ion beams.' *Radiat. Res.* (2006) **166**(4): 629–638. doi:10.1667/RR0536.1.

[4] Kase Y, Kanai T, Sakama M, Tameshige Y, Himukai T, *et al.* 'Microdosimetric Approach to NIRS-defined Biological Dose Measurement for Carbon-ion Treatment Beam.' *J. Radiat. Res.* (2011) **52**(1): 59–68. doi:10.1269/jrr.10062.

[5] Krämer M, Durante M. 'Ion beam transport calculations and treatment plans in particle therapy.' *Eur. Phys. J. D* (2010) **60**(1): 195–202. doi:10.1140/epjd/e2010-00077-8.

[6] Tobias F, Durante M, Taucher-Scholz G, Jakob B. 'Spatiotemporal analysis of DNA repair using charged particle radiation.' *Mutat. Res.-Rev. Mutat.* (2010) **704**(1-3): 54–60. doi:10.1016/j.mrrev.2009.11.004.

[7] Schardt D, Elsaesser T, Schulz-Ertner D. 'Heavy-ion tumor therapy: Physical and radiobiological benefits.' *Rev. Mod. Phys.* (2010) **82**(1): 383–425. doi:10.1103/RevModPhys.82.383.

[8] International Commission of Radiation Units and Measurements (ICRU). *Report 36, Microdosimetry* (ICRU, Bethesda, MD 1983).

[9] Waker AJ. 'Principles of experimental microdosimetry.' *Radiat. Prot. Dosim.* (1995) **61**(4): 297–308. `http://rpd.oxfordjournals.org/content/61/4/297.abstract?sid=4df572f6-4dcb-47d9-a202-2a8fb4652bc3`.

[10] Waker AJ. 'Techniques for radiation measurements: microdosimetry and dosimetry.' *Radiat. Prot. Dosim.* (2006) **122**(1-4): 369–373. doi:10.1093/rpd/ncl497.

[11] Rossi HH. 'The role of microdosimetry in the understanding of radiation quality.' *Radiat. Prot. Dosim.* (1990) **31**(1-4): 361–365. `http://rpd.oxfordjournals.org/content/31/1-4/361.abstract`.

[12] Lindborg L, Nikjoo H. 'Microdosimetry and radiation quality determinations in radiation protection and radiation therapy.' *Radiat. Prot. Dosim.* (2011) **143**(2-4): 402–408. doi:10.1093/rpd/ncq390.

[13] Gersey BB, Borak TB, Guetersloh SB, Zeitlin C, Miller J, *et al.* 'The response of a spherical tissue-equivalent proportional counter to iron particles from 200-1000 MeV/nucleon.' *Radiat. Res.* (2002) **157**(3): 350–360. doi:10.1667/0033-7587(2002)157[0350:TROAST]2.0.CO;2.

[14] Guetersloh S, Borak T, Taddei P, Zeitlin C, Heilbronn L, *et al.* 'The response of a spherical tissue-equivalent proportional counter to different ions having similar linear energy transfer.' *Radiat. Res.* (2004) **161**(1): 64–71. doi:10.1667/RR3101.

[15] Taddei PJ, Borak TB, Guetersloh SB, Gersey BB, Zeitlin C, *et al.* 'The response of a spherical tissue-equivalent proportional counter to different heavy ions having similar velocities.' *Radiat. Meas.* (2006) **41**(9-10): 1227–1234. doi:10.1016/j.radmeas.2006.01.003.

[16] Nikjoo H, Khvostunov IK, Cucinotta FA. 'The Response of Tissue-Equivalent Proportional Counters to Heavy Ions.' *Radiat. Res.* (2002) **157**(4): 435–445. doi:10.1667/0033-7587(2002)157[0435:TROTEP]2.0.CO;2.

[17] Taddei PJ, Zhao Z, Borak TB. 'A comparison of the measured responses of a tissue-equivalent proportional counter to high energy heavy (HZE) particles and those simulated using the Geant4 Monte Carlo code.' *Radiat. Meas.* (2008) **43**(9-10): 1498–1505. doi:10.1016/j.radmeas.2008.09.003.

[18] Endo S, Tanaka K, Ishikawa M, Hoshi M, Onizuka Y, *et al.* 'Microdosimetric evaluation of the 400 MeV/nucleon carbon beam at HIMAC.' *Med. Phys.* (2005) **32**(12): 3843–3848. doi:10.1118/1.2133719.

[19] Haettner E, Iwase H, Schardt D. 'Experimental fragmentation studies with ^{12}C therapy beams.' *Radiat. Prot. Dosim.* (2006) **122**(1-4): 485–487. doi:10.1093/rpd/ncl402.

[20] Endo S, Takada M, Onizuka Y, Tanaka K, Maeda N, *et al.* 'Microdosimetric evaluation of secondary particles in a phantom produced by carbon 290 MeV/nucleon ions at HIMAC.' *J. Radiat. Res.* (2007) **48**(5): 397–406. doi:10.1269/jrr.07016.

[21] Tsuda S, Sato T, Takahashi F, Satoh D, Endo A, *et al.* 'Measurement of microdosimetric spectra with a wall-less tissue-equivalent proportional counter for a 290 MeV/u ^{12}C beam.' *Phys. Med. Biol.* (2010) **55**(17): 5089–5101. doi:10.1088/0031-9155/55/17/013.

[22] Tsuda S, Sato T, Takahashi F, Satoh D, Sasaki S, *et al.* 'Systematic Measurement of Lineal Energy Distributions for Proton, He and Si Ion Beams Over a Wide Energy Range Using a Wall-less Tissue Equivalent Proportional Counter.' *J. Radiat. Res.* (2012) **53**(2): 264–271. doi:10.1269/jrr.11135.

[23] Martino G, Durante M, Schardt D. 'Microdosimetry measurements characterizing the radiation fields of 300 MeV/u ^{12}C and 185 MeV/u ^{7}Li pencil beams stopping in water.' *Phys. Med. Biol.* (2010) **55**(12): 3441–3449. doi:10.1088/0031-9155/55/12/011.

[24] Yonai S, Kase Y, Matsufuji N, Kanai T, Nishio T, *et al.* 'Measurement of absorbed dose, quality factor, and dose equivalent in water phantom outside of the irradiation field in passive carbon-ion and proton radiotherapies.' *Med. Phys.* (2010) **37**(8): 4046–4055. doi:10.1118/1.3458721.

[25] Remmes NB, Herman MG, Kruse JJ. 'Optimizing normal tissue sparing in ion therapy using calculated isoeffective dose for ion selection.' *Int. J. Radiat. Oncol.* (2012) **83**(2): 756–762. doi:10.1016/j.ijrobp.2011.08.006.

[26] Blakely EA, Tobias CA, Smith KC, Lyman JT. 'Inactivation of Human Kidney Cells by High-Energy Monoenergetic Heavy-Ion Beams.' *Radiat. Res.* (1979) **80**(1): 122–160. doi:10.2307/3575121.

[27] Weyrather WK, Ritter S, Scholz M, Kraft G. 'RBE for carbon track-segment irradiation in cell lines of differing repair capacity.' *Int. J. Radiat. Biol.* (1999) **75**(11): 1357–1364. doi:10.1080/095530099139232.

[28] Furusawa Y, Fukutsu K, Aoki M, Itsukaichi H, Eguchi-Kasai K, *et al.* 'Inactivation of aerobic and hypoxic cells from three different cell lines by accelerated He-3-,C-12- and Ne-20-ion beams.' *Radiat. Res.* (2000) **154**(5): 485–496. doi:10.1667/0033-7587(2000)154[0485:IOAAHC]2.0.CO;2.

[29] Kraft G. 'Tumor therapy with heavy charged particles.' *Prog. Part. Nucl. Phys.* (2000) **45**(Suppl. 2): S473–S544. doi:10.1016/S0146-6410(00)00112-5.

[30] Scholz M, Elsässer T. 'Biophysical models in ion beam radiotherapy.' *Adv. Space Res.* (2007) **40**(9): 1381–1391. doi:10.1016/j.asr.2007.02.066.

[31] Ottolenghi A, Merzagora M, Paretzke HG. 'DNA complex lesions induced by protons and α-particles: track structure characteristics determining linear energy transfer and particle type dependence.' *Radiat. Environ. Bioph.* (1997) **36**(2): 97–103. doi:10.1007/s004110050060.

[32] Friedland W, Dingfelder M, Kundrát P, Jacob P. 'Track structures, DNA targets and radiation effects in the biophysical Monte Carlo simulation code PARTRAC.' *Mutat. Res.-Fund. Mol. M.* (2011) **711**(1-2): 28–40. doi:10.1016/j.mrfmmm.2011.01.003.

[33] Hawkins RB. 'A Statistical Theory of Cell Killing by Radiation of Varying Linear Energy Transfer.' *Radiat. Res.* (1994) **140**(3): 366–374. doi:10.2307/3579114.

[34] Hawkins RB. 'A microdosimetric-kinetic model of cell death from exposure to ionizing radiation of any LET, with experimental and clinical applications.' *Int. J. Radiat. Biol.* (1996) **69**(6): 739–755. doi:10.1080/095530096145481.

[35] Hawkins RB. 'A Microdosimetric-Kinetic Model for the Effect of Non-Poisson Distribution of Lethal Lesions on the Variation of RBE with LET.' *Radiat. Res.* (2003) **160**(1): 61–69. doi:10.1667/RR3010.

[36] Kase Y, Kanai T, Matsufuji N, Furusawa Y, Elsässer T, *et al.* 'Biophysical calculation of cell survival probabilities using amorphous track structure models for heavy-ion irradiation.' *Phys. Med. Biol.* (2008) **53**(1): 37–59. doi:10.1088/0031-9155/53/1/003.

[37] Sato T, Watanabe R, Kase Y, Tsuruoka C, Suzuki M, *et al.* 'Analysis of cell-survival fractions for heavy-ion irradiations based on microdosimetric kinetic model implemented in the particle and heavy ion transport code system.' *Radiat. Prot. Dosim.* (2011) **143**(2-4): 491–496. doi:10.1093/rpd/ncq484.

[38] Metropolis N. *The Beginning of the Monte Carlo Method*, volume 15 (Special Issue, Stanislaw Ulam 1909-1984) of *Los Alamos Science* (1987). LA-UR-88-9067.

[39] Ferrari A, Sala PR, Fassò A, Ranft J. *FLUKA: A multi-particle transport code (program version 2005)* (CERN, Geneva 2005). doi:10.5170/CERN-2005-010.

[40] Battistoni G, Cerutti F, Fassò A, Ferrari A, Muraro S, *et al.* 'The FLUKA code: description and benchmarking.' *AIP Conf. Proc.* (2007) **896**(1): 31–49. doi:10.1063/1.2720455.

[41] Agostinelli S, Allison J, Amako K, Apostolakis J, Araujo H, *et al.* 'GEANT4-a simulation toolkit.' *Nucl. Instrum. Meth. A* (2003) **506**(3): 250–303. doi:10.1016/S0168-9002(03)01368-8.

[42] Allison J, Amako K, Apostolakis J, Araujo H, Dubois P, *et al.* 'Geant4 developments and applications.' *IEEE T. Nucl. Sci.* (2006) **53**(1, Part 2): 270–278. doi:10.1109/TNS.2006.869826.

[43] Mashnik SG, Bull JS, Hughes HG, Prael RE, Sierk AJ. 'Current status of MCNP6 as a simulation tool useful for space and accelerator applications.' *AIP Conf. Proc.* (2013) **1560**(1): 706–708. doi:10.1063/1.4826878.

[44] Iwase H, Niita K, Nakamura T. 'Development of General-Purpose Particle and Heavy Ion Transport Monte Carlo Code.' *J. Nucl. Sci. Technol.* (2002) **39**(11): 1142–1151. doi:10.1080/18811248.2002.9715305.

[45] Niita K, Sato T, Iwase H, Nose H, Nakashima H, *et al.* 'PHITS - a particle and heavy ion transport code system.' *Radiat. Meas.* (2006) **41**(9-10): 1080–1090. doi:10.1016/j.radmeas.2006.07.013.

[46] Sato T, Niita K, Matsuda N, Hashimoto S, Iwamoto Y, *et al.* 'Particle and Heavy Ion Transport code System, PHITS, version 2.52.' *J. Nucl. Sci. Technol.* (2013) **50**(9): 913–923. doi:10.1080/00223131.2013.814553.

[47] Gudowska I, Sobolevsky N, Andreo P, Belkic D, Brahme A. 'Ion beam transport in tissue-like media using the Monte Carlo code SHIELD-HIT.' *Phys. Med. Biol.* (2004) **49**(10): 1933–1958. doi:10.1088/0031-9155/49/10/008.

[48] Hansen DC, Lühr A, Herrmann R, Sobolevsky N, Bassler N. 'Recent improvements in the SHIELD-HIT code.' *Int. J. Radiat. Biol.* (2012) **88**(1-2): 195–199. doi:10.3109/09553002.2011.610863.

[49] Perl J, Shin J, Schümann J, Faddegon B, Paganetti H. 'TOPAS: An innovative proton Monte Carlo platform for research and clinical applications.' *Med. Phys.* (2012) **39**(11): 6818–6837. doi:10.1118/1.4758060.

[50] Geant4 Collaboration. 'Physics Reference Manual.' (2012). URL `http://geant4.web.cern.ch/geant4/support/userdocuments.shtml`.

[51] Pshenichnov I, Mishustin I, Greiner W. 'Neutrons from fragmentation of light nuclei in tissue-like media: a study with the GEANT4 toolkit.' *Phys. Med. Biol.* (2005) **50**(23): 5493–5507. doi:10.1088/0031-9155/50/23/005.

[52] Pshenichnov I, Mishustin I, Greiner W. 'Distributions of positron-emitting nuclei in proton and carbon-ion therapy studied with GEANT4.' *Phys. Med. Biol.* (2006) **51**(23): 6099–6112. doi:10.1088/0031-9155/51/23/011.

[53] Pshenichnov I, Larionov A, Mishustin I, Greiner W. 'PET monitoring of cancer therapy with He-3 and C-12 beams: a study with the GEANT4 toolkit.' *Phys. Med. Biol.* (2007) **52**(24): 7295–7312. doi:10.1088/0031-9155/52/24/007.

[54] Pshenichnov I, Mishustin I, Greiner W. 'Comparative study of depth-dose distributions for beams of light and heavy nuclei in tissue-like media.' *Nucl. Instrum. Meth. B* (2008) **266**(7): 1094–1098. doi:10.1016/j.nimb.2008.02.025.

[55] Mishustin I, Pshenichnov I, Greiner W. 'Modelling heavy-ion energy deposition in extended media.' *Eur. Phys. J. D* (2010) **60**(1): 109–114. doi:10.1140/epjd/e2010-00187-3.

[56] Pshenichnov I, Botvina A, Mishustin I, Greiner W. 'Nuclear fragmentation reactions in extended media studied with Geant4 toolkit.' *Nucl. Instrum. Meth. B* (2010) **268**(6): 604–615. doi:10.1016/j.nimb.2009.12.023.

[57] Bleicher M, Burigo L, Durante M, Herrlitz M, Krämer M, *et al.* 'Nanolesions induced by heavy ions in human tissues: Experimental and theoretical studies.' *Beilstein J. Nanotechnol.* (2012) **3**: 556–563. doi:10.3762/bjnano.3.64.

[58] Burigo L, Pshenichnov I, Mishustin I, Bleicher M. 'Microdosimetry of radiation field from a therapeutic ^{12}C beam in water: A study with Geant4 toolkit.' *Nucl. Instrum. Meth. B* (2013) **310**: 37–53. doi:10.1016/j.nimb.2013.05.021.

[59] Burigo L, Pshenichnov I, Mishustin I, Bleicher M. 'Monte Carlo simulations of Microdosimetry for Space Research at FAIR.' *J. Phys. Conf. Ser.* (2013) **426**(1): 012006. doi:10.1088/1742-6596/426/1/012006.

[60] Burigo L, Pshenichnov I, Mishustin I, Bleicher M. 'Microdosimetry spectra and RBE of ^{1}H, ^{4}He, ^{7}Li and ^{12}C nuclei in water studied with Geant4.' *Nucl. Instrum. Meth. B* (2014) **320**: 89–99. doi:10.1016/j.nimb.2013.10.018.

[61] Burigo LN, Pshenichnov IA, Mishustin IN, Bleicher M. 'Radiation quality of cosmic ray nuclei studied with Geant4-based simulations.' *J. Phys. Conf. Ser.* (2014) **503**(1): 012021. doi:10.1088/1742-6596/503/1/012021.

[62] Burigo L, Pshenichnov I, Mishustin I, Bleicher M. 'Comparative study of RBE and cell survival fractions for ^{1}H, ^{4}He, ^{12}C and ^{16}O beams using Geant4 and Microdosimetric Kinetic model.' (2014). arXiv:1403.7929 [physics.med-ph].

[63] Tsuda S, Sato T, Takahashi F, Satoh D, Endo A, *et al.* 'Analysis of the effect of structural materials in a wall-less tissue-equivalent proportional counter irradiated by 290 MeV u^{-1} carbon beam.' *Radiat. Prot. Dosim.* (2011) **143**(2-4): 450–454. doi:10.1093/rpd/ncq536.

[64] Lechner A, Ivanchenko VN, Knobloch J. 'Validation of recent Geant4 physics models for application in carbon ion therapy.' *Nucl. Instrum. Meth. B* (2010) **268**(14): 2343–2354. doi:10.1016/j.nimb.2010.04.008.

[65] Incerti S, Ivanchenko A, Karamitros M, Mantero A, Moretto P, *et al.* 'Comparison of GEANT4 very low energy cross section models with experimental data in water.' *Med. Phys.* (2010) **37**(9): 4692–4708. doi:10.1118/1.3476457.

[66] International Commission of Radiation Units and Measurements (ICRU). *Report 49, Stopping Powers and Ranges for Protons and Alpha Particles* (ICRU, Bethesda, MD 1993).

[67] International Commission of Radiation Units and Measurements (ICRU). *Report 73, Stopping of Ions Heavier than Helium* (ICRU, Bethesda, MD 2005).

[68] Ivanchenko V, Apostolakis J, Bagulya A, Abdelouahed HB, Black R, *et al.* 'Recent Improvements in Geant4 Electromagnetic Physics Models and Interfaces.' *Prog. Nucl. Sci. Tech.* (2011) **2**: 898–903.

[69] Wellisch HP, Axen D. 'Total reaction cross section calculations in proton-nucleus scattering.' *Phys. Rev. C* (1996) **54**: 1329–1332. doi:10.1103/PhysRevC.54.1329.

[70] Shen W, Wang B, Feng J, long Zhan W, tai Zhu Y, *et al.* 'Total reaction cross section for heavy-ion collisions and its relation to the neutron excess degree of freedom .' *Nucl. Phys. A* (1989) **491**(1): 130–146. doi:10.1016/0375-9474(89)90209-1.

[71] Tripathi R, Cucinotta FA, Wilson JW. 'Accurate universal parameterization of absorption cross sections.' *Nucl. Instrum. Meth. B* (1996) **117**(4): 347–349. doi:10.1016/0168-583X(96)00331-X.

[72] Tripathi R, Cucinotta F, Wilson J. 'Accurate universal parameterization of absorption cross sections III - light systems.' *Nucl. Instrum. Meth. B* (1999) **155**(4): 349–356. doi:10.1016/S0168-583X(99)00479-6.

[73] Folger G, Ivanchenko V, Wellisch J. 'The Binary Cascade.' *Eur. Phys. J A* (2004) **21**(3): 407–417. doi:10.1140/epja/i2003-10219-7.

[74] Koi T. 'New native QMD code in Geant4.' *Proceedings of the MC2010 Monte Carlo Conference* (2010) .

[75] Böhlen TT, Cerutti F, Dosanjh M, Ferrari A, Gudowska I, *et al.* 'Benchmarking nuclear models of FLUKA and GEANT4 for carbon ion therapy.' *Phys. Med. Biol.* (2010) **55**(19): 5833–5847. doi:10.1088/0031-9155/55/19/014.

[76] Bondorf J, Botvina A, Iljinov A, Mishustin I, Sneppen K. 'Statistical Multifragmentation of Nuclei.' *Phys. Rep.* (1995) **257**(3): 133–221. doi:10.1016/0370-1573(94)00097-M.

[77] Weisskopf V, Ewing D. 'On the Yield of Nuclear Reactions with Heavy Elements.' *Phys. Rev.* (1940) **57**(6): 472–485. doi:10.1103/PhysRev.57.472.

[78] National Aeronautics and Space Administration (NASA). 'Exploration: Beyond Earth.' URL `http://www.nasa.gov/exploration/home/index.html`.

[79] European Space Agency (ESA). 'The European Space Exploration Programme Aurora.' URL `http://www.esa.int/Our_Activities/Human_Spaceflight/Exploration/The_European_Space_Exploration_Programme_Aurora`.

[80] Durante M, Cucinotta FA. 'Physical basis of radiation protection in space travel.' *Rev. Mod. Phys.* (2011) **83**: 1245–1281. doi:10.1103/RevModPhys.83.1245.

[81] Schimmerling W, Cucinotta F, Wilson J. 'Radiation risk and human space exploration.' *Adv. Space Res.* (2003) **31**(1): 27–34. doi:10.1016/S0273-1177(02)00653-1.

[82] Durante M, Kraft G, O'Neill P, Reitz G, Sabatier L, *et al.* 'Preparatory study of a ground-based space radiobiology program in Europe.' *Adv. Space Res.* (2007) **39**(6): 1082–1086. doi:10.1016/j.asr.2006.10.007.

[83] National Aeronautics and Space Administration (NASA). 'Space Radiation Analysis Group, Johnson Space Center.' URL `http://srag.jsc.nasa.gov/Index.cfm`.

[84] Cucinotta FA, Durante M. 'Cancer risk from exposure to galactic cosmic rays: implications for space exploration by human beings.' *Lancet Oncol.* (2006) **7**(5): 431–435. doi:10.1016/S1470-2045(06)70695-7.

[85] Durante M, Cucinotta FA. 'Heavy ion carcinogenesis and human space exploration.' *Nat. Rev. Cancer* (2008) **8**(6): 465–472. doi:10.1038/nrc2391.

[86] Badhwar GD, Cucinotta FA, Braby LA, Konradi A. 'Measurements on the Shuttle of the LET Spectra of Galactic Cosmic Radiation and Comparison with the Radiation Transport Model.' *Radiat. Res.* (1994) **139**(3): 344–351. doi:10.2307/3578832.

[87] Badhwar G, Atwell W, Benton E, Frank A, Keegan R, *et al.* 'A study of the radiation environment on board the Space Shuttle flight STS-57.' *Radiat. Meas.* (1995) **24**(3): 283–289. doi:10.1016/1350-4487(95)00007-2.

[88] Badhwar GD, Keith JE, Cleghorn TF. 'Neutron measurements onboard the space shuttle.' *Radiat. Meas.* (2001) **33**(3): 235–241. doi:10.1016/S1350-4487(00)00159-1.

[89] Reitz G, Beaujean R, Benton E, Burmeister S, Dachev T, *et al.* 'Space radiation measurements on-board ISS - the DOSMAP experiment.' *Radiat. Prot. Dosim.* (2005) **116**(1-4): 374–379. doi:10.1093/rpd/nci262.

[90] National Council on Radiation Protection and Measurements (NCRP). *Report No. 153, Information Needed to Make Radiation Protection Recommendations for Space Missions Beyond Low-Earth Orbit* (NCRP, Bethesda, MD 2006).

[91] Durante M. 'BIOMAT. Biophysics collaboration: applications of relativistic heavy ions in radiobiology and space radiation protection.' *FAIR Newsletter* (2006) **3**: 11–13.

[92] Rademacher SE, Borak TB, Zeitlin C, Heilbronn L, Miller J. 'Wall Effects Observed in Tissue-Equivalent Proportional Counters from 1.05 GeV/nucleon Iron-56 Particles.' *Radiat. Res.* (1998) **149**(4): 387–395. doi:10.2307/3579702.

[93] Böhlen TT, Dosanjh M, Ferrari A, Gudowska I, Mairani A. 'FLUKA simulations of the response of tissue-equivalent proportional counters to ion beams for applications in hadron therapy and space.' *Phys. Med. Biol.* (2011) **56**: 6545–6561. doi:10.1088/0031-9155/56/20/002.

[94] Haettner E, Iwase H, Krämer M, Kraft G, Schardt D. 'Experimental study of nuclear fragmentation of 200 and 400 MeV/ u ^{12}C ions in water for applications in particle therapy.' *Phys. Med. Biol.* (2013) **58**(23): 8265–8279. doi:10.1088/0031-9155/58/23/8265.

[95] Hultqvist M, Lillhok JE, Lindborg L, Gudowska I, Nikjoo H. 'Nanodosimetry in a ^{12}C ion beam using Monte Carlo simulations.' *Radiat. Meas.* (2010) **45**(10): 1238–1241. doi:10.1016/j.radmeas.2010.05.033.

[96] Taleei R, Hultqvist M, Gudowska I, Nikjoo H. 'A Monte Carlo evaluation of carbon and lithium ions dose distributions in water.' *Int. J. Radiat. Biol.* (2012) **88**(1-2): 189–194. doi:10.3109/09553002.2011.624572.

[97] Böhlen TT, Dosanjh M, Ferrari A, Gudowska I. 'Simulations of microdosimetric quantities with the Monte Carlo code FLUKA for carbon ions at therapeutic energies.' *Int. J. Radiat. Biol.* (2012) **88**(1-2): 176–182. doi:10.3109/09553002.2011.620062.

[98] Nakane Y, Sakamoto Y. 'Measurement of absorbed dose distributions in a plastic phantom irradiated by 40-and 65-MeV quasi-monoenergetic neutrons.' *Nucl. Instrum. Meth. A* (2001) **459**(3): 552–564. doi:10.1016/S0168-9002(00)01022-6.

[99] Tsuda S, Nakane Y, Yamaguchi Y. 'Calculation of energy distributions of charged particles produced by neutrons from 0.14 to 65 MeV in tissue substitutes.' *Radiat. Prot. Dosim.* (2007) **126**(1-4): 174–177. doi:10.1093/rpd/ncm037.

[100] Toftegaard J, Bassler N. 'Stopping Power of Ions.' (2012). URL `http://dedx.au.dk/`.

[101] Luhr A, Toftegaard J, Kantemiris I, Hansen DC, Bassler N. 'Stopping power for particle therapy: The generic library libdEdx and clinically relevant stopping-power ratios for light ions.' *Int. J. Radiat. Biol.* (2012) **88**(1-2): 209–212. doi:10.3109/09553002.2011.595877.

[102] Jiang H, Wang B, Xu X, Suit H, Paganetti H. 'Simulation of organ-specific patient effective dose due to secondary neutrons in proton radiation treatment.' *Phys. Med. Biol.* (2005) **50**(18): 4337–4353. doi:10.1088/0031-9155/50/18/007.

[103] Jarlskog CZ, Paganetti H. 'Risk of developing second cancer from neutron dose in proton therapy as function of field characteristics, organ, and patient age.' *Int. J. Radiat. Oncol.* (2008) **72**(1): 228–235. doi:10.1016/j.ijrobp.2008.04.069.

[104] Xu XG, Bednarz B, Paganetti H. 'A review of dosimetry studies on external-beam radiation treatment with respect to second cancer induction.' *Phys. Med. Biol.* (2008) **53**(13): R193–R241. doi:10.1088/0031-9155/53/13/R01.

[105] Newhauser WD, Durante M. 'Assessing the risk of second malignancies after modern radiotherapy.' *Nat. Rev. Cancer* (2011) **11**(6): 438–448. doi:10.1038/nrc3069.

[106] Kellerer A. 'Risk estimates for radiation-induced cancer - the epidemiological evidence.' *Radiat. Environ. Bioph.* (2000) **39**(1): 17–24. doi:10.1007/PL00007679.

[107] Grahn D, Lombard LS, Carnes BA. 'The Comparative Tumorigenic Effects of Fission Neutrons and Co-60 γ Rays in the B6CF$_1$ mouse.' *Radiat. Res.* (1992) **129**(1): 19–36. doi:10.2307/3577899.

[108] Dennis J. 'Relative biological effectiveness of neutron radiation and its implications for quality factor and dose limitation.' *Prog. Nucl. Energ.* (1987) **20**(2): 133–149. doi:10.1016/0149-1970(87)90018-7.

[109] Endo S, Tanaka K, Takada M, Onizuka Y, Miyahara N, *et al.* 'Microdosimetric study for secondary neutrons in phantom produced by a 290 MeV/nucleon carbon beam.' *Med. Phys.* (2007) **34**(9): 3571–3578. doi:10.1118/1.2767933.

[110] Wissmann F, Giesen U, Klages T, Schardt D, Martino G, *et al.* 'Microdosimetric measurements in the secondary radiation field produced in ^{12}C-therapy irradiations.' *Radiat. Environ. Bioph.* (2010) **49**(3): 331–336. doi:10.1007/s00411-010-0279-z.

[111] Jensen AD, Muenter MW, Debus J. 'Review of clinical experience with ion beam radiotherapy.' *Brit. J. Radiol.* (2011) **84**(1): S35–S47. doi:10.1259/bjr/71511359.

[112] Kamada T. 'Clinical evidence of particle beam therapy (carbon).' *Int. J. Clin. Oncol.* (2012) **17**(2): 85–88. doi:10.1007/s10147-012-0388-6.

[113] Kempe J, Gudowska I, Brahme A. 'Depth absorbed dose and LET distributions of therapeutic ^{1}H, ^{4}He, ^{7}Li, and ^{12}C beams.' *Med. Phys.* (2007) **34**(1): 183–192. doi:10.1118/1.2400621.

[114] Kantemiris I, Karaiskos P, Papagiannis P, Angelopoulos A. 'Dose and dose averaged LET comparison of ^{1}H, ^{4}He, ^{6}Li, ^{8}Be, ^{10}B, ^{12}C, ^{14}N, and ^{16}O ion beams forming a spread-out Bragg peak.' *Med. Phys.* (2011) **38**(12): 6585–6591. doi:10.1118/1.3662911.

[115] Moteabbed M, Geyer A, Drenkhahn R, Bolch WE, Paganetti H. 'Comparison of whole-body phantom designs to estimate organ equivalent neutron doses for secondary cancer risk assessment in proton therapy.' *Phys. Med. Biol.* (2012) **57**(2): 499–515. doi:10.1088/0031-9155/57/2/499.

[116] Seravalli E, Robert C, Bauer J, Stichelbaut F, Kurz C, *et al.* 'Monte Carlo calculations of positron emitter yields in proton radiotherapy.' *Phys. Med. Biol.* (2012) **57**(6): 1659–1673. doi:10.1088/0031-9155/57/6/1659.

[117] Kase Y, Kanematsu N, Kanai T, Matsufuji N. 'Biological dose calculation with Monte Carlo physics simulation for heavy-ion radiotherapy.' *Phys. Med. Biol.* (2006) **51**(24): N467–N475. doi:10.1088/0031-9155/51/24/N03.

[118] Gueulette J, Wambersie A. 'Comparison of the methods of specifying carbon ion doses at NIRS and GSI.' *J. Radiat. Res.* (2007) **48**(Suppl. A): A97–A102. doi:10.1269/jrr.48.A97.

[119] Chapman J, Blakely E, Smith K, Urtasun R. 'Radiobiological characterization of the inactivating events produced in mammalian cells by helium and heavy ions.' *Int. J. Radiat. Oncol.* (1977) **3**: 97–102. doi:10.1016/0360-3016(77)90234-6.

[120] Kanai T, Endo M, Minohara S, Miyahara N, Koyama-ito H, *et al.* 'Biophysical characteristics of HIMAC clinical irradiation system for heavy-ion radiation therapy.' *Int. J. Radiat. Oncol.* (1999) **44**(1): 201–210. doi:10.1016/S0360-3016(98)00544-6.

[121] Matsufuji N, Kanai T, Kanematsu N, Miyamoto T, Baba M, *et al.* 'Specification of carbon ion dose at the National Institute of Radiological Sciences (NIRS).' *J. Radiat. Res.* (2007) **48**(Suppl. A): A81–A86. doi:10.1269/jrr.48.A81.

[122] Tsujii H, etsu Mizoe J, Kamada T, Baba M, Kato S, *et al.* 'Overview of clinical experiences on carbon ion radiotherapy at NIRS.' *Radiother. Oncol.* (2004) **73**(Suppl. 2): S41–S49. doi:10.1016/S0167-8140(04)80012-4.

[123] Schulz-Ertner D, Tsujii H. 'Particle Radiation Therapy Using Proton and Heavier Ion Beams.' *J. Clin. Oncol.* (2007) **25**(8): 953–964. doi:10.1200/JCO.2006.09.7816.

[124] Combs SE, Jäkel O, Haberer T, Debus J. 'Particle therapy at the Heidelberg Ion Therapy Center (HIT) - Integrated research-driven university-hospital-based radiation oncology service in Heidelberg, Germany .' *Radiother. Oncol.* (2010) **95**(1): 41–44. doi:10.1016/j.radonc.2010.02.016.

[125] Wilkens JJ, Oelfke U. 'Direct Comparison of Biologically Optimized Spread-out Bragg Peaks for Protons and Carbon Ions .' *Int. J. Radiat. Oncol.* (2008) **70**(1): 262–266. doi:10.1016/j.ijrobp.2007.08.029.

[126] Suit H, DeLaney T, Goldberg S, Paganetti H, Clasie B, *et al.* 'Proton vs carbon ion beams in the definitive radiation treatment of cancer patients.' *Radiother. Oncol.* (2010) **95**(1): 3–22. doi:10.1016/j.radonc.2010.01.015.

[127] Brahme A, Lewensohn R, Ringborg U, Amaldi U, Gerardi F, *et al.* 'Design of a centre for biologically optimised light ion therapy in Stockholm.' *Nucl. Instrum. Meth. B* (2001) **184**(4): 569–588. doi:10.1016/S0168-583X(01)00781-9.

[128] Svensson H, Ringborg U, Naeslund I, Brahme A. 'Development of light ion therapy at the Karolinska Hospital and Institute.' *Radiother. Oncol.* (2004) **73**(Suppl. 2): S206–S210. doi:10.1016/S0167-8140(04)80049-5.

[129] Lundkvist J, Ekman M, Ericsson S, Jonsson B, Glimelius B. 'Proton therapy of cancer: Potential clinical advantages and cost-effectiveness.' *Acta. Oncol.* (2005) **44**(8): 850–861. doi:10.1080/02841860500341157.

[130] Krämer M, Jäkel O, Haberer T, Kraft G, Schardt D, *et al.* 'Treatment planning for heavy-ion radiotherapy: physical beam model and dose optimization.' *Phys. Med. Biol.* (2000) **45**(11): 3299–3317. doi:10.1088/0031-9155/45/11/313.

[131] Krämer M, Scholz M. 'Treatment planning for heavy-ion radiotherapy: calculation and optimization of biologically effective dose.' *Phys. Med. Biol.* (2000) **45**(11): 3319–3330. doi:10.1088/0031-9155/45/11/314.

[132] Jäkel O, Krämer M, Karger C, Debus J. 'Treatment planning for heavy ion radiotherapy: clinical implementation and application.' *Phys. Med. Biol.* (2001) **46**(4): 1101–1116. doi:10.1088/0031-9155/46/4/314.

[133] Zaider M, Rossi HH. 'The Synergistic Effects of Different Radiations.' *Radiat. Res.* (1980) **83**(3): 732–739. doi:10.2307/3575352.

[134] Kase Y, Himukai T, Nagano A, Tameshige Y, Minohara S, *et al.* 'Preliminary Calculation of RBE-weighted Dose Distribution for Cerebral Radionecrosis in Carbon-ion Treatment Planning.' *J. Radiat. Res.* (2011) **52**(6): 789–796. doi:10.1269/jrr.11044.

[135] Haberer T, Debus J, Eickhoff H, Jäkel O, Schulz-Ertner D, *et al.* 'The Heidelberg Ion Therapy Center .' *Radiother. Oncol.* (2004) **73**(Suppl. 2): S186–S190. doi:10.1016/S0167-8140(04)80046-X.

[136] Bassler N, Jäkel O, Søndergaard CS, Petersen JB. 'Dose- and LET-painting with particle therapy.' *Acta. Oncol.* (2010) **49**(7): 1170–1176. doi:10.3109/0284186X.2010.510640.